Adaptation of a W-Band EPR Spectrometer to UHV Conditions

Dissertation zur Erlangung des akademischen Grades des
Doktors der Naturwissenschaften (Dr. rer. nat.)

eingereicht im Fachbereich Biologie, Chemie, Pharmazie
der Freien Universität Berlin

vorgelegt von

Esther Kieseritzky geb. Fischbach
aus Berlin

2010

Die vorliegende Arbeit wurde im Zeitraum Juli 2005 bis August 2010 am Fritz-Haber-Institut der Max-Planck-Gesellschaft, Abteilung Chemische Physik, unter der Leitung von Prof. Dr. H.-J. Freund angefertigt.

1. Gutachter: Prof. Dr. H.-J. Freund
2. Gutachter: Prof. Dr. K. Christmann

Disputation am: 13.10.2010

Acknowledgements/Danksagung

Der Aufbau und die Inbetriebnahme der Apparatur waren und sind ein großes Projekt, dass ohne die Hilfe zahlreicher Personen nicht zustande gekommen wäre. Bei all diesen möchte ich mich herzlich bedanken. Mein besonderer Danke gilt:

- Herrn Prof. Hans-Joachim Freund dafür, mir dieses Hochrisikoprojekt der Max-Planck-Gesellschaft anzuvertrauen,
- Herrn Prof. Klaus Christmann für die Übernahme des Zweitgutachtens,
- Dr. Thomas Risse für die ungezählten Stunden, die wir gemeinsam an diesem Projekt verbracht haben sowohl voller Enthusiasmus als auch am Boden zerstört, für das (Mit-)Teilen seines Wissens über surface science, Korrektur der Doktorarbeit, Fahrradrepatur am Freitag Abend, ...
- Werner Hänsel-Ziegler für die technische Unterstützung insbesonderem auch die technischen Zeichnungen in dieser Arbeit
- Dr. Alex Bondarchuk for sharing the machine with me and teaching me a lot about UHV business, special thanks for your unique menus in the afternoon,
- Jan Rocker und Anja Seiler für die Übernahme und Fortführung des Projekts, Jan außerdem für die zahlreichen Belehrungen zu Musik und Kino,
- all current and former members of the EPR group for the support we gave one another,
- der Elektronikwerkstatt, der Feinwerktechnik, der Schlosserei und Klaus-Peter Vogelgesang für die Anfertigung hunderter Kleinteile und größerer Gerätschaften,
- the members of the CP department for answering 1001 questions about science as well as engineering and lending equipment when necessary and possible,
- Dr. Aditya Ashi Savara, Dr. John Uhlrich, Rhys Dowler, and Dr. Nicola Scott for comments regarding the use of the English language in the written thesis,

- the people of the EPR community (especially Prof. Dr. Dinse, Prof. Dr. Bittl and his group, Dr. Alexander Schnegg, Dr. Paul Cruickshanks) for helpful comments on the realization of the EPR UHV setup,

- der Studienstiftung des deutschen Volkes für die finanzielle und idelle Förderung, im Besonderen meinem Vertrauensdozenten Prof. Onno Oncken für höchste interessante Gesprächsrunden und Ausflüge,

- meinem Eltern, die mich auf diesen Weg geführt haben, auch wenn mein Vater diese Zwischenstation meines Lebensweges nicht mehr erleben kann,

- Gernot für das gegenseitige bei der Stange halten während der Promotion,

- Ann-Sophie, die mich auch nach einem frustrierenden Arbeitstag zum Lachen bringen konnte (so sie noch wach war).

Contents

Chapter 1

Introduction

In the last few decades the interest in a detailed description of microscopic processes on metal oxide surfaces has increased continuously [69]. This is motivated by the broad areas of application for these materials. Representative sensor technology, superconductivity, and catalysis shall be mentioned here. In the field of heterogeneous catalysis, metal oxides are either used as the support for a catalytically active species – oftentimes a metallic species –, or they serve as catalysts themselves. An understanding of the catalytic activity requires a microscopic understanding of the various sites, with respect to their geometric and electronic structure as well as their catalytic properties. In the case of complex powder catalysts, this ambitious goal is often beyond todays experimental capabilities. Thus, the quest for solutions to this problem is still actively pursued in various directions.

Reducing the inherent complexity of the catalysts is an obvious possibility which has been one of the main driving forces to develop modern surface science. Metal single crystals with well-defined geometric and electronic properties have been investigated under ultra high vacuum (UHV) conditions, and have been employed in experiments to elucidate reaction mechanisms of heterogeneously catalyzed reactions. The success of this approach was recently recognized by the 2007 Nobel Price in chemistry awarded to Gerhard Ertl [46]. Within this approach, the support, which is often an oxide, is simply ignored. This shortcoming was addressed in the last two decades by developing heterogeneous model catalysts using single crystalline oxide surfaces as supports. The implementation of this strategy was hampered by the fact that most of the oxides used as supports are insulators, which renders them unsuitable towards characterization by methods which involve charged particles such as electrons as probes. Thin, single-crystalline oxide films grown on metal single crystal surfaces were shown to be a valuable solution, because they retain much of the complexity of real catalysts while being suitable towards characterization using modern surface science techniques [36, 53, 127].

The development of proper model systems is an important ingredient to advance our understanding of catalytic systems. However, the availability of appro-

priate experimental techniques to address the various questions at hand is of at least equal importance. In fact, major advancements of our understanding are associated with the development of experimental techniques. Scanning tunneling microscopy (STM) is perhaps one of the best examples where a single technique has advanced our perception of surfaces tremendously [21,105]. In comparison to metals, oxides have considerably different electronic properties which also require different methodologies to probe them. Defects, and in particular point defects, may serve as an instructive example. The latter are thought to play an important role for the properties of oxide surfaces, however, an atomistic characterization of point defects is still challenging. This is the typical scenario where method development sets in. With respect to point defects in oxides, electron paramagnetic resonance (EPR) spectroscopy was used for decades to characterize these species in the bulk, due to the paramagnetic nature of some of these sites. The application of EPR spectroscopy to single crystal surfaces is more demanding, but was shown possible using an X-Band (9.5 GHz) spectrometer [117]. These experiments allow characterization of paramagnetic surface species in terms of their geometric as well as electronic environment [131,137,164]. With respect to the above-mentioned problem of point defects, the spectral resolution of X-Band spectroscopy, which is governed by the g-anisotropy of the species, is inapplicable towards discriminating the various sites. To this end, increasing the spectral resolution would provide additional atomistic insight into these systems. Increased spectral resolution can be achieved by increasing the operation frequency of the spectrometer along the lines pursued in nuclear magnetic resonance (NMR) spectroscopy. In practice, the extension to higher frequencies proved useful not only in terms of spectral resolution but also in terms of sensitivity [18,51,80]. Since the first high field EPR spectrometer installation in 1983 [107], the use of frequencies ≥ 94 GHz has steadily increased and in 1996 the first commercial W-band spectrometer (94 GHz) made this frequency regime accessible to a larger scientific group [118]. Adapting such a commercially available W-Band EPR spectrometer (E600, Bruker) to a UHV apparatus was the central objective of the current thesis project. This increases the operating frequency and thus the spectral resolution by an order of magnitude as compared to the existing X-Band implementations at UHV. The corresponding reduction of the operating wavelength by a factor of 10 has severe implications for the implementation as a simple transfer of the X-band design was impossible. Therefore, the measuring setup had to be redesigned which will be discussed in detail.

EPR spectroscopy alone is insufficient to reach a comprehensive picture of the surface at hand, because the method is exclusively sensitive to paramagnetic species which are usually minority sites on the surface. Thus, it is important to combine this spectroscopy with other techniques that allow characterization of the surface with respect to the geometry, adsorption properties, chemical composition etcetera. For this purpose, the current setup contains capabilities to deploy low energy electron diffraction (LEED), Auger electron spectroscopy (AES) and scanning tunneling microscopy for elucidation of the geometric structure as well

as the chemical composition of the surface. In addition, infrared spectroscopy as well as a quadrupole mass spectrometer (QMS) is implemented to obtain chemical information of the adsorbates.

The thesis is structured as follows: Chapter 2 reviews the main techniques of the experimental setup with emphasis on EPR spectroscopy. Chapter 3 gives a detailed description of the experimental setup starting with design considerations imposed by the W-band spectrometer. Subsequently, all parts of the UHV system are depicted in detail. The resonator used in the UHV implementation of the W-band spectrometer is introduced in chapter 4. Besides a general overview of the theory involved, the special considerations to perform EPR measurements of the indicated frequency in UHV are discussed. This includes a description of the evolutional development of the resonator and the implications involved. As many X-band experiments in the past were performed on MgO thin films [131, 137, 164] this system is chosen for initial experiments using the different techniques. Chapter 5 is therefore dedicated to MgO thin films using silver or molybdenum as substrates. First, the effect of substrate temperature onto MgO film growth is compared for the two metal single crystals using Auger electron spectroscopy. Then a short characterization of MgO on silver by STM is given in order to test the performance of the microscope. Afterwards, the adsorption behavior of N_2O on the MgO surface is described as inferred from Fourier transfer infrared (FT IR) spectra. Finally, W-band EPR measurements under UHV conditions are presented. The performance of the resonator is analyzed by adsorption of an organic radical onto MgO films. An initial measurement of defects in the MgO film completes the thesis.

Chapter 2

Experimental Techniques

2.1 Electron Paramagnetic Resonance

In electron paramagnetic resonance (EPR) spectroscopy species with one or more unpaired electron spins are investigated. This chapter will first give an introduction into the theoretical basis of EPR. After addressing a quantum mechanical description of the processes involved, they will be brought in contact with the context of the measurable quantities of the EPR experiment. The second goal of this chapter is to point out the necessity and beauty of performing experiments at different microwave frequencies, in relation to this thesis especially high field experiments. Finally, the chapter concludes with a description of the EPR spectrometer and how a spectrum is obtained.

2.1.1 The Free Electron

The magnetic moment of a free electron $\vec{\mu}_s$ is directly proportional to the intrinsic angular momentum $\vec{S}$ of the electron which is commonly called spin:

$$\vec{\mu}_s = -\frac{g_e \mu_B}{\hbar} \vec{S} \tag{2.1}$$

g_e is the so-called free electron g-factor. In general, a g-factor is a dimensionless, system-specific quantity that relates magnetic moment and angular momentum. In the special case of the free electron g_e equals 2.002319 [145]. $\mu_B = \frac{e\hbar}{2m_e}$ is the Bohr magneton which expresses the magnetic moment one expects for one unit of quantum mechanical angular momentum in the case of electrons. $\hbar$ is the reduced Planck constant ($\hbar = h/2\pi$) and m_e the electron mass. The interaction of a free electron exposed to an external magnetic field is described by the following Hamiltonian:

$$\mathfrak{H} = \frac{g_e \mu_B}{\hbar} \vec{S} \vec{B} \tag{2.2}$$

The term magnetic field for the quantity $\vec{B}$ will be used throughout this thesis as is commonly done in EPR. However, one has to keep in mind that $\vec{B}$ represents the

magnetic flux density alias magnetic induction with the unit of tesla ($T = kg/s{\cdot}C$) and differs from the magnetic 'field' $\vec{H}$. The two are related by:

$$\vec{B} \;=\; \widehat{\mu}\vec{H} \tag{2.3}$$

$\widehat{\mu}$ is the permeability of the medium and in general is a second rank tensor which reduces to a scalar in an isotropic medium and μ_0 in vacuum. In this case $\vec{B}$ and $\vec{H}$ have the same orientation and eq. 2.3 is often expressed in terms of scalar measures as:

$$B \;=\; \mu_0(H + M) \tag{2.4}$$

with M being the magnetization. In vacuum eq. 2.4 reduces to:

$$B \;=\; \mu_0 H \tag{2.5}$$

A particle with spin $\vec{S}$ has $2S{+}1$ possible orientations with respect to the magnetic field. A single electron is a fermion and therefore a spin 1/2 particle. Thus, two states exist. They are separated by the following energy:

$$\Delta E \;=\; g_e \mu_B B_0 \;\text{ with }\; \vec{B} \;=\; (0, 0, B_0) \tag{2.6}$$

The splitting of intrinsic angular momenta in a magnetic field was first observed by P. Zeeman and is named after him as the Zeeman effect [166]. An EPR spectrum, as it is expected for a free electron, is shown in the top part of Fig. 2.1. Due to the lock-in technique used (see also section 2.1.8) the first derivative of the absorption signal is observed. The physical interactions leading to the spectra below will be topic of the next section.

2.1.2 The Electron in an Atomic Framework

In contrast to the previously idealized cases, the unpaired electrons investigated in EPR are associated with atoms in various environments. This implies that other angular momenta present in the system may have to be taken into account, as they will also interact with the external magnetic field. For an electron caught in a potential the orbital angular momentum $\vec{L}$ also reacts to an applied field. In the presence of atoms with nuclear angular momenta $\vec{I} \neq 0$, e.g., ^{14}N with $I = 1$, these also couple with the magnetic field. This leads to the following Hamiltonian for the possible Zeeman interactions [5, 57]:

$$\mathfrak{H}_{Zeeman} \;=\; \frac{g_e \mu_B}{\hbar}\vec{S}\vec{B} + \frac{\mu_B}{\hbar}\vec{L}\vec{B} + \frac{g_n \mu_n}{\hbar}\vec{I}\vec{B} \tag{2.7}$$

g_n is the nuclear g-factor and μ_n the nuclear magneton with $\mu_n = \frac{e\hbar}{2m_P}$, m_P being the proton mass. As μ_B and μ_n are reciprocally related to the specific particle mass the third term in eq. 2.7 is about three orders of magnitude smaller than the first one. Additionally, selection rules as derived by first order perturbation theory do not allow simultaneous excitation of the nuclear and the electron spin

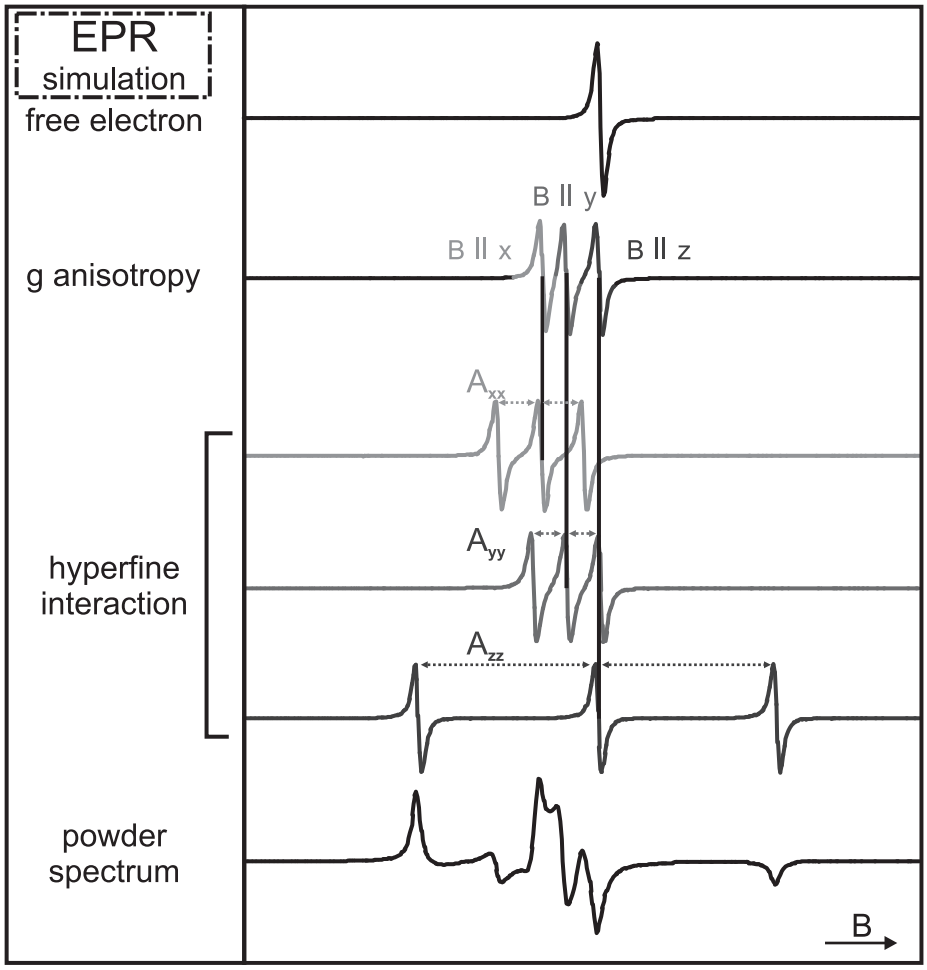

Figure 2.1: Effects of molecular anisotropy on the final shape of the EPR spectrum, $\widehat{A}$ is taken congruent with $\widehat{g}$.

(see also section 2.1.3). Furthermore the nuclear Zeeman interaction does not change the energy difference for the electron excitations. For these reasons the nuclear Zeeman interaction is often neglected as will be done here [57].

Much more important for EPR spectroscopy is the interaction of the nuclear spin with the electron spin known as hyperfine interaction. This coupling consists of two parts. One is the classically expected dipole-dipole interaction of two magnetic moments as described by [5]:

$$\mathfrak{H}_{HF,\,dipolar} = \frac{\mu_0}{4\pi}\frac{g_e\mu_B}{\hbar}\frac{g_n\mu_n}{\hbar}\left(\frac{3(\vec{S}\vec{r})(\vec{I}\vec{r})}{r^5} - \frac{\vec{S}\vec{I}}{r^3}\right) \tag{2.8}$$

If the electron has finite probability to be found at the nucleus, which is the case for *s*-orbitals, the system is not properly described by eq. 2.8 but an additional term has to be added. Derived by Fermi it is called the Fermi contact interaction [48]:

$$\mathfrak{H}_{HF,\,contact} = \frac{2\mu_0}{3}\frac{g_e\mu_B}{\hbar}\frac{g_n\mu_n}{\hbar}\left|\psi(0)\right|^2\vec{S}\vec{I} \tag{2.9}$$

$|\psi(0)|^2$ is the probability to find the electron at the nucleus. Although the contact interaction depends on the dot product $\vec{S}\cdot\vec{I}$, it is isotropic in space.

The electron spin $\vec{S}$ not only interacts with surrounding nuclei, but also with the electron's own orbital angular momentum $\vec{L}$. This spin-orbit coupling is known to be responsible for the fine structure of atomic spectral lines [91]. It is expressed by:

$$\mathfrak{H}_{\vec{L}\vec{S}} = \xi(r)\vec{L}\vec{S} \tag{2.10}$$

The interactions discussed so far consisting of the Zeeman interaction, the spin-orbit coupling, and the hyperfine interaction add up to the following Hamiltonian:

$$\begin{aligned}\mathfrak{H}_{extended} &= \mathfrak{H}_{Zeeman} + \mathfrak{H}_{\vec{L}\vec{S}} + \mathfrak{H}_{HF,\,dipolar} + \mathfrak{H}_{HF,\,contact}\\ &= \mathfrak{H}_{Zeeman} + \mathfrak{H}_{\vec{L}\vec{S}} + \mathfrak{H}_{HF}\end{aligned} \tag{2.11}$$

Under certain assumptions this expression can be transformed into a Hamiltonian that only depends on the spin operators $\vec{S}$ and $\vec{I}$ as will be seen below.

The g-Tensor. At first only the spin-orbit coupling as well as the electron Zeeman interaction will be considered. The idea is to combine the three terms describing the interaction between electron spin, orbital angular momentum, and magnetic field such that one characteristic parameter suffices for a complete description. Therefore a quantum mechanical treatment will be done applying perturbation theory. This is justified by the fact that the energies involved are much smaller than those of the remaining electronic Hamiltonian (kinetic energy, Coulomb energy, etcetera). The eigenstates of the unperturbed Hamiltonian will be denoted by $|n\rangle$ and the corresponding energy eigenvalues by $E_n^{(0)}$.

Essential for the following discussion is the 'quenching' of the orbital angular momentum. This effect will be demonstrated using a simple molecular orbital scheme and applying it to the radical di-tert-butyl nitroxide (DTBN). The molecular structure is shown in Fig. 2.2 along with the molecular coordinate system centered on the paramagnetic site. In the molecule, the degeneracy of the three atomic p-orbials of the nitrogen atom is lifted. The orbitals form three lower lying sp^2-orbitals for bonding to adjacent atoms and an unhybridized p-orbital which hosts the unpaired electron. As a non-degenerate single-electron wavefunction it can always be described by a real function [6]. The operator of the orbital angular momentum is purely imaginary. However, as $\vec{L}^2$ is an observable the expectation value has to be real. The only solution to obtain a real value for this observable in the case of a real wavefunction is by setting $L = 0$. As such, the molecule can be treated as an orbital singlet (^2S) in the ground state. More generally, whenever the ground state is non-degenerate the orbital angular momentum is

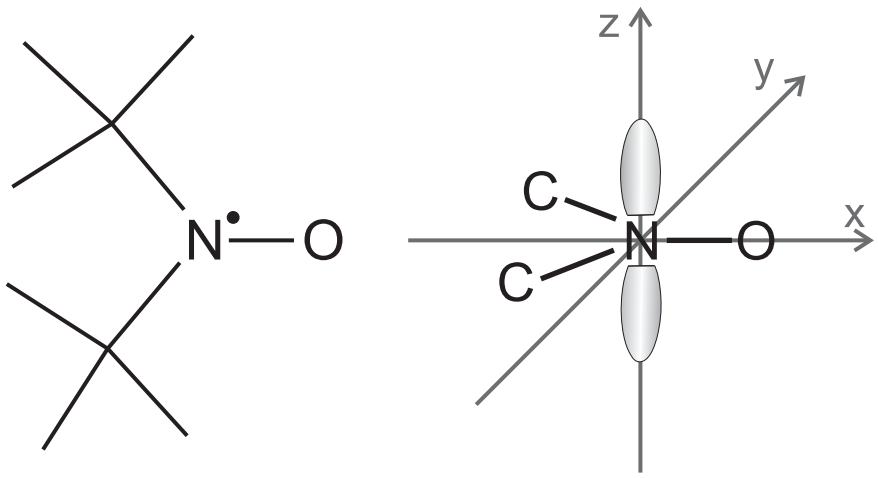

Figure 2.2: The molecular structure of DTBN (left) and the main axes of the g-tensor (right).

'quenched' with the above meaning. Applying first order perturbation theory, one obtains for every non-degenerate state the correction to the ground-state energy by determining the expectation value of the perturbing operator applied onto the ground-state wavefunction [92]:

$$\begin{aligned} E_0^{(1)} &= \langle 0|\mathfrak{H}'|0\rangle \\ &= \frac{g_i\mu_B}{\hbar}\langle 0|\vec{S}\vec{B}|0\rangle + \frac{\mu_B}{\hbar}\langle 0|\vec{L}\vec{B}|0\rangle + \langle 0|\xi(r)\vec{L}\vec{S}|0\rangle \end{aligned} \tag{2.12}$$

g_i is an isotropic g-value that usually deviates from the free electron value by a small admixture of orbital angular momenta [5, 57]. $\vec{S}$ only acts on spin space and $\vec{L}$ on real space. In case of quantization along the z-direction $E_0^{(1)}$ can than be rearranged to:

$$E_0^{(1)} = \frac{g_i\mu_B}{\hbar}B_z\langle 0|0\rangle S_z + \frac{\mu_B B_z}{\hbar}\langle 0|L_z|0\rangle + \lambda\langle 0|L_z|0\rangle S_z \tag{2.13}$$

To derive eq. 2.13, it was assumed that the ground-state wavefunction can be separated into a radial component and an angular dependent component. Then λ is understood as the expectation value of $\xi(r)$ on the radial component whereas $\vec{L}$ only acts on the angular one. As $L = 0$, the term $\langle 0|L_z|0\rangle$ also has to vanish. Thus, only the first term in eq. 2.13 remains. The according Hamiltonian is given by:

$$\mathfrak{H}'^{(1)}_{spin} = \frac{g_i\mu_B}{\hbar}\vec{S}\vec{B} \tag{2.14}$$

This describes an isotropic interaction between an electron and a magnetic field.

Conducting the perturbation theory to second order reveals that the anisotropy of the g-factor for the ground state can be attributed to the interaction with ex-

cited states $|1\rangle ... |n\rangle$ [57]. The second-order energy correction reads as follows [92]:

$$E_0^{(2)} = -\sum_{n\neq 0} \frac{\langle 0|\mathfrak{H}'|n\rangle\langle n|\mathfrak{H}'|0\rangle}{E_n^{(0)} - E_0^{(0)}} \tag{2.15}$$

It is again assumed that the wavefunctions are separable into angular and radial components. After insertion of the $\vec{L}$-dependent terms for $\mathfrak{H}'$ the following spin Hamiltonian is obtained [57]:

$$\begin{aligned} \mathfrak{H}'^{(2)}_{spin} = -2\frac{\mu_B}{\hbar}\lambda \sum_{i,j=x,y,z} \Lambda_{ij} B_i S_j - \lambda^2 \sum_{i,j=x,y,z} \Lambda_{ij} S_i S_j \\ -\frac{\mu_B^2}{\hbar^2} \sum_{i,j=x,y,z} \Lambda_{ij} B_i B_j, \end{aligned} \tag{2.16}$$

with

$$\Lambda_{ij} = \sum_{n\neq 0} \frac{\langle 0|L_i|n\rangle\langle n|L_j|0\rangle}{E_n^{(0)} - E_0^{(0)}} \tag{2.17}$$

The last term in eq. 2.16 describes the diamagnetic interaction. As it is small compared to the first term it is generally neglected. The middle term accounts for anisotropic spin-spin interactions that are mediated by spin-orbit coupling. They are intramolecular interactions that are small in nature and vanish for single unpaired electrons [57]. Therefore only the first term in eq. 2.16 remains.

The spin Hamiltonian, including first and second order perturbations without hyperfine interactions, thus reduces to:

$$\begin{aligned} \mathfrak{H}_{spin} &= \mathfrak{H}^{(1)}_{spin} + \mathfrak{H}^{(2)}_{spin} \\ &= \frac{g_i \mu_B}{\hbar} \vec{S}\vec{B} - 2\frac{\mu_B}{\hbar}\lambda \sum_{i,j=x,y,z} \Lambda_{ij} B_i S_j \\ &= \frac{\mu_B}{\hbar} \sum_{i,j=x,y,z} g_{ij} B_i S_j, \end{aligned} \tag{2.18}$$

with

$$g_{ij} = g_i \delta_{ij} - 2\lambda\Lambda_{ij} \tag{2.19}$$

$$\text{mit } \delta_{ij} = \begin{cases} 1 & i = j \\ 0 & i \neq j \end{cases} \tag{2.20}$$

As $2\lambda\Lambda_{ij}$ is a 3×3 matrix, this also holds true for g_{ij}, which is the reason why it is frequently called the g-tensor. However, in strictly mathematical terms, only the square of $\widehat{g}$ is a tensor. Eq. 2.18 can be abbreviated by:

$$\mathfrak{H}_{spin} = \frac{\mu_B}{\hbar} \vec{S}\widehat{g}\vec{B} \tag{2.21}$$

All operators contained in Λ_{ij} are hermitian and result therefore in a symmetric matrix. Thus, the matrix can always be diagonalized choosing an appropriate coordinate system. The task is to determine the three principal components of the g-matrix and their orientation with respect to the molecular framework. The latter can be greatly simplified by symmetry considerations [99]. The second spectrum in Fig. 2.1 shows the three different absorption lines for an anisotropic g-tensor where each spectrum is obtained by aligning the magnetic field along one of the principal g-axes.

The A-Tensor. To include the hyperfine interaction the nuclear-dependent term in eq. 2.11 has to be evaluated. Conducting a derivation similar to the one for the g-tensor it is found that [57]:

$$\mathfrak{H}_{HF} \;=\; \sum_{i,j} \left(A_{ij}^{anisotrop} + \delta_{ij} a_{iso} \right) S_i I_j \;=\; \vec{S}\widehat{A}\vec{I} \tag{2.22}$$

The A- and g-tensor have the same properties. Combining the two expressions the spin Hamiltonian is given by:

$$\mathfrak{H}_{spin} \;=\; \mathfrak{H}_{Zeeman} + \mathfrak{H}_{HF} \;=\; \frac{\mu_B}{\hbar} \vec{S}\widehat{g}\vec{B} + \vec{S}\widehat{A}\vec{I} \tag{2.23}$$

2.1.3 The Resonance Condition

Energy Eigen Values. If there is no hyperfine interaction, eq. 2.23 consists of only the first term. For this case, the energy eigenvalues will be derived.

In general the magnetic field $\vec{B}$ is defined in the laboratory frame whereas $\vec{S}$ is defined in the spin coordinate system. Before the energy eigenvalues can be evaluated the coordinate systems have to be aligned appropriately. In the language of quantum mechanics a common set of eigen functions for $\mathfrak{H}_{spin}$ and S_z has to be found. The magnetic field B_0 is taken to be aligned along the z-direction of the laboratory frame. By an Euler transformation it is rotated into the coordinate system in which the g-tensor is diagonal. The combined system $\widehat{g}\vec{B}_0$ is transformed such that it is aligned along the quantization axis (here the z-axis) by a second Euler transformation [10,11]. The stationary solutions of the Schrödinger equation then become:

$$E_n^{(0)} \;=\; E_{S,\,m_S}^{(0)} \;=\; \mu_B g_{eff} B_0 m_s \tag{2.24}$$

with

$$g_{eff} \;=\; \sqrt{(g_{xx}^2 \cos^2\phi + g_{yy}^2 \sin^2\phi)\sin^2\vartheta + g_{zz}^2 \cos^2\vartheta} \tag{2.25}$$

ϑ is defined as the angle between the static field and g_{zz}, and ϕ is the corresponding azimuthal angle in the xy-plane of the g-tensor. To incorporate hyperfine coupling in the analysis, the strength of the Zeeman interaction has to be evaluated in comparison with the hyperfine interaction. In the cases where the Zeeman interaction is much larger than the hyperfine interaction the latter can be treated as perturbation. As this becomes true for high magnetic fields the application

of first order perturbation theory is called the 'high field' approach [5, 152]. Extending the treatment to second order induces shifts in the expected transitions leading to asymmetry in the spectrum [5]. The expressions up to second order in the case of an anisotropic g- and an anisotropic A-tensor are found in [10, 11]. If the electron Zeeman interaction and the hyperfine coupling are of the same order of magnitude the problem can no longer be treated by perturbation theory but a full matrix diagonalization must be performed. This is in most cases done numerically and open source programs like Easyspin are available to solve such problems [140, 141].

Transition Probability and Selection Rules. In the following section, expressions for the transition probability between spin states will be found that allow determination of the transition selection rules. The static magnetic field itself cannot induce transitions between spin states. For the occurrence of a transition, an oscillating magnetic field $B(t)$ which is perpendicular to the static field has to be irradiated onto the sample [5]. Usually B_0 is aligned along the z-axis of the laboratory frame while $B(t)$ is assumed to be linearly polarized along the x-axis. If the amplitude of $B(t)$ is sufficiently small the problem can be treated by perturbation theory. The perturbing term can be described to be sinusoidal with angular velocity ω ($B(t) = B_1\vec{e}_x \sin\omega t$). The additional term arising in the Hamiltonian is:

$$\mathfrak{H}_{MW} = \mu_B \vec{S}\hat{g}\vec{B}(t) \tag{2.26}$$

Using time-dependent perturbation theory one derives the transition probability which is time independent for the periodic perturbation [91, 126]:

$$W_{fi} = \frac{2\pi}{\hbar}|\langle f|\mathfrak{H}_{MW}|i\rangle|^2\delta(E_f - E_i - h\nu) \tag{2.27}$$

with i representing the initial state and f the final state. The δ-function only differs from zero for $E_f - E_i = h\nu$ and ensures energy conservation. Substituting $\mathfrak{H}_{MW}$ in eq. 2.27 by the appropriate expression given in eq. 2.26 and explicitly writing the components of the angular momentum operator gives:

$$W_{fi} = \frac{2\pi\mu_B^2}{\hbar}|B_1|^2|\langle f|c_xS_x + c_yS_y + c_zS_z|i\rangle|^2 \tag{2.28}$$

To extract the selection rules for allowed transitions it is useful to express the x- and y-components of $\vec{S}$ in terms of raising and lowering operators. The applied static field along z prevents transitions taking place in this direction and the S_z-component can be neglected. The above equation thus transforms to:

$$W_{fi} = \frac{\pi\mu_B^2}{2\hbar}|B_1|^2|\langle f|(c_x - ic_y)S_+ + (c_x + ic_y)S_-|i\rangle|^2 \tag{2.29}$$

Whereas the raising operator S_+ describes the absorption of a photon the lowering operator S_- relates to the induced photon emission. Both events are equally probable. Therefore no conclusion about the net absorption of the system can

be drawn from the probabilities. To observe absorption during the experiment a population difference of the spin states as described by the Boltzmann distribution has to be sustained. This will be further discussed in section 2.1.5. From eq. 2.29 follows that the integral is only non-zero if m_s of the initial and the final state differ by 1; that is $\Delta m_s = \pm 1$. In the case of a single unpaired electron, photon absorption thus takes place for excitations between $m_s = -1/2$ and $m_s = +1/2$. The coefficients c_x and c_y depend on the polar angles ϑ and ϕ. Therefore also the transition probability containing these parameters depends on the orientation of the static magnetic field B_0 in the g-matrix framework [10].

As $\Delta m_I = 0$ during the electron spin transitions, the spectra in Fig. 2.1 can be understood as follows: If the B_0-field is aligned along one axis three transitions are expected, one for each state of $\vec{I}$ ($m_I = +1, 0, -1$) with m_s changing by 1. The intensity of all lines is equal as the populations of all three upper states ($m_s = +1/2$, $m_I = +1, 0, -1$) are assumed to be the same as well as of the three lower states ($m_s = -1/2$, $m_I = +1, 0, -1$). The spacing of the lines is determined by the hyperfine component of the observed orientation.

In the previous pages, the microwave frequency was treated as tunable and the magnetic field as static. Technical aspects lead to the fact that in most EPR experiments the frequency is kept constant whereas the magnetic field is swept. Therefore formally the frequency (energy) axis has to be transformed to the corresponding magnetic field axis. This leads to the following expression for the case without hyperfine interaction:

$$B(\nu_0, m_s, \vartheta, \phi) \;=\; \frac{h\nu_0}{g_{eff}\mu_B} \tag{2.30}$$

Expressions including the hyperfine interaction can be found elsewhere [10, 11]. Obviously the magnetic field value at which the transition occurs depends on the orientation between the molecular coordinate system and the field itself. In the case of disordered samples, such as most powders, the spectrum is obtained by integrating over all possible orientations between the molecular coordinate system and the magnetic field. An example of this is shown at the bottom of Fig. 2.1.

2.1.4 Magnetic Susceptibility

Up until this point in the thesis, the quantum mechanical interaction between single paramagnetic centers and the magnetic field has been described. In an EPR experiment, however, an ensemble of paramagnetic species is observed. The macroscopic quantity measured will be introduced shortly in the following.

Application of an external magnetic field to an ensemble of unpaired electrons leads to an alignment of magnetic dipole moments and thus a magnetic polarization which is commonly called magnetization ($\vec{M}$). In the case of paramagnetic materials, the magnetization is proportional to the magnetic field strength H_0 and the magnetic induction B_0 and assuming collinearity the magnetization can be expressed as:

$$M = \chi H_0 = \frac{\chi}{\mu_0} B_0 \tag{2.31}$$

Where eq. 2.5 was used on the right hand side. The proportionality factor χ defined in this equation is the volume magnetic susceptibility. If N independent particles contribute to M and the Hamiltonian for the system is described by $\mathfrak{H} = g\mu_B B_0 S_z$ the expectation value of the magnetization is related to the microscopic spin S by [5, 55, 110]:

$$\langle M \rangle = \frac{N g^2 \mu_B^2 S(S+1) B_0}{3 V_s k T} \tag{2.32}$$

with V_s being the sample volume, k the Boltzmann constant, and T the temperature. Combining eq. 2.31 and eq. 2.32, the magnetic susceptibility relates to the microscopic world by the following equation:

$$\chi = \frac{\mu_0 N g^2 \mu_B^2 S(S+1)}{3 V_s k T} \tag{2.33}$$

The inverse relationship between the susceptibility and temperature is known as Curie's law. The direct scaling of χ with the number of particles as well as the inverse temperature dependence are used in quantitative analysis of signal intensities in EPR.

As excitation in EPR is achieved by an alternating field the spectrum is not determined by the above mentioned static susceptibility but has to be related to the complex high-frequency susceptibility:

$$\chi_{compl} = \chi' + i\chi'' \tag{2.34}$$

It can be shown that the dissipation of energy is associated with the imaginary part χ'' [5] and is usually the observed quantity in EPR experiments. More precisely, due to the lock-in technique used the change of the imaginary part of the susceptibility with the magnetic field $d\chi''/dB_0$ is measured. The conclusions drawn follow from the more general linear response theory. It states that a small periodic perturbation leads to a response that can always be described by a complex response function with the imaginary part related to the power absorbed (see, e.g., [109]). The real part of the response specifies the phase lag in the response of the system to the perturbation and is called dispersion. In general χ' can be deduced from χ'' by an integral transform. It can also be determined experimentally. The proportionality to N/T shown in eq. 2.33 also holds true for χ'' [1]. The ability to decrease temperature to increase intensity has a lower limit given by the necessary dissipation of the energy absorbed. This process called relaxation will be subject of the next section.

2.1.5 Relaxation and Lineshape

A standard model to describe relaxation of a spin system in EPR is the Bloch ansatz, which was originally proposed for nuclear magnetic resonance [23]. The basic principles involved will shortly be discussed. Applying a static magnetic field along the z-axis induces – within a classical picture – a precession of the present spins about this axis. The Boltzmann statistics in this case predict a population difference between the two spin states taking part in the excitation and therefore a magnetization along the z-axis. A change in magnetization along this axis is thereby directly correlated with a change in population difference. The single spin also has a magnetization component in the xy-plane but there is no phase coherence to the other spins of the ensemble in this plane. Thus, there is no macroscopic magnetization in the xy-plane. Having this in mind, Bloch wanted to describe relaxation by two processes: one is the energy dissipation to restore the population difference, the other the loss in coherence. In his ansatz, both processes are described by an exponential decay. The characteristic time constants appearing in the exponential terms are called T_1 and T_2. T_1 characterizes the exponential recovery of the z-component whereas T_2 describes the exponential drop of phase coherence. In general the two times are not equal as they are connected to different physical processes. Loss in phase coherence is not necessarily coupled to spin flipping while transitions between two spin states also lead to phase decoherence (a more detailed description is found in, e.g., [1]). The equations of motion including the relaxation take the following form:

$$\frac{dM_z}{dt} = \gamma(\vec{B} \times \vec{M})_z + \frac{M_0 - M_z}{T_1} \tag{2.35}$$

$$\frac{dM_x}{dt} = \gamma(\vec{B} \times \vec{M})_x - \frac{M_x}{T_2} \tag{2.36}$$

$$\frac{dM_y}{dt} = \gamma(\vec{B} \times \vec{M})_y - \frac{M_x}{T_2} \tag{2.37}$$

with γ being the gyromagnetic ratio ($-g_i\mu_B/\hbar$). To perform an EPR experiment a periodic oscillating field with amplitude B_1 is applied (commonly along the x-axis) and has to be added to the equations of motion above [152]. Solving the resulting equations and expressing them in terms of the components of the complex susceptibility leads to [5]:

$$\chi' = \frac{1}{2}\left\{\frac{\gamma M_0(\omega_0 - \omega)}{\gamma^2 B_1^2(T_1/T_2) + (1/T_2)^2 + (\omega_0 - \omega)^2}\right\} \tag{2.38}$$

$$\chi'' = \frac{1}{2}\left\{\frac{\gamma M_0(1/T_2)}{\gamma^2 B_1^2(T_1/T_2) + (1/T_2)^2 + (\omega_0 - \omega)^2}\right\} \tag{2.39}$$

where ω_0 is equal to γB_0. To deduce the lineshape of the absorption signal eq. 2.39 has to be analyzed. Obviously χ'' depends on the incident microwave field B_1.

As the term B_1^2 describes saturation effects it can be neglected as long as an appropriate incident microwave power is chosen in the EPR experiment. In this case eq. 2.39 reduces to an expression of the well known Lorentzian lineshape. Therefore the EPR spectra of an ensemble of non-interacting spins with a single transition frequency are expected to show a Lorentzian line or rather its first derivative.

So far the treatment dealt with independent particles. In the next section the influence of intermolecular interactions onto the line shape and especially linewidth are discussed.

2.1.6 Intermolecular Interactions

In the case of diluted samples the effect of intermolecular interactions onto the EPR signal is small and in most cases ignored. However, for sufficiently concentrated samples intermolecular interactions can change the EPR spectrum substantially. In solids, dipolar and exchange interactions between electrons play an important role and will be discussed briefly in the following [20]. The exchange interaction results from orbital overlap and is thus usually important at short distances. If the distance between adjacent spins is larger than 8 to 10 Å the dipolar interaction has generally the greater influence.

The spin of an electron is a magnetic dipole whose field acts upon other magnetic moments in its surroundings. One of the resulting interactions is the dipolar part of the hyperfine coupling introduced in section 2.1.2. An equivalent interaction is to be expected for two unpaired electrons. In analogy to eq. 2.8 and assuming isotropic g-values g_1 and g_2 the dipolar interaction between electrons can directly be written as:

$$\mathfrak{H}_{d-d} \;=\; \frac{g_1 g_2 \mu_B^2}{\hbar^2}\left(\frac{-3(\vec{S}_1\vec{r})(\vec{S}_2\vec{r})}{r^5}+\frac{\vec{S}_1\vec{S}_2}{r^3}\right) \tag{2.40}$$

In this simple case the dipolar interaction leads to splitting of an EPR line into two lines. The size of the splitting is given by:

$$\text{dipolar splitting} = g_1 g_2 \mu_B^2 (1 - cos^2\theta)/r^3 \tag{2.41}$$

with r being the interspin distance and θ the angle between magnetic field and $\vec{r}$. At the 'magic angle' of 54.7° the splitting vanishes. For large separations of the adjacent spins, the splitting is not observed due to the r^{-3} dependence.

In the more general case, both centers can have anisotropic g-values. Assuming a coincident principal axes for the two g-matrices involved and that the interspin vector is aligned along the z-axis, the Hamiltonian can be divided into two components, an isotropic component and an anisotropic component:

$$\mathfrak{H}_{d-d} \;= -J_{d-d}\vec{S_1}\vec{S_2} + \vec{S_1}\widehat{D}\vec{S_2} \tag{2.42}$$

The interaction matrix $\widehat{D}$ in eq. 2.42 is symmetrical about the diagonal. It has to be emphasized that the isotropic contribution is only significant for systems with large g-anisotropy. Eq. 2.41 still describes the dipolar interaction well if all three g components are of similar value. A discussion of the general case allowing arbitrary g-tensors and arbitrary orientation is beyond the current scope and can be found in the literature [24].

The other interaction that comes into play if two paramagnetic centers are close to each other is the exchange interaction. At a large distance the electron orbitals do not interact. However, as the separation is decreased, two energy levels are formed with either an antiparallel bonding orientation of the spins or a parallel antibonding one. The energy separating these two levels is called exchange energy and depends strongly on the distance of the two spins. Although an overlap of electron orbitals is mandatory for spin exchange no direct overlap of the two orbitals involved is necessary. The exchange can also be mediated by intervening atoms, e.g., a delocalized π-system. Assuming that the wavefunctions are negligibly disturbed by this interaction, the exchange will not influence the Zeeman interaction which is generally describe by $\widehat{g}$. In the isotropic case the Hamiltonian describing the exchange interaction is:

$$\mathfrak{H}_{ex} = J_{12}(r)\vec{S_1}\vec{S_2} \tag{2.43}$$

Similar to the spin-orbit coupling of a single paramagnetic species that leads to anisotropy in $\widehat{g}$ the exchange interaction of the ground state of one center with the excited states of another center introduces an anisotropic exchange term. This anisotropic exchange term which can – in analogy to the dipolar coupling – be written in the form $\vec{S_1}\widehat{D}_{ex}\vec{S_2}$ is large for systems that have considerable spin-orbit coupling, e.g., Cu(II) complexes. For systems that do not have a center of inversion the spin-orbit coupling can also lead to antisymmetric exchange contributions, but the effects are difficult to distinguish from the antisymmetric dipolar terms and unambiguous experimental data are lacking.

So far, dipolar and exchange interaction were discussed separately, but as they both arise from interaction between two paramagnetic centers they are present at the same time. Whether one of the interactions dominates the spectrum depends on the details of the system. As mentioned before the distance between adjacent spins allows already a good estimation of which interaction dominates. Mathematically, the exchange and dipolar contributions can be combined in one Hamiltonian:

$$\mathfrak{H}_{ex/dd} = \vec{S_1}\widehat{I}\vec{S_2} \tag{2.44}$$

The matrix $\widehat{I}$ is an arbitrary matrix that can be subdivided into three parts: a scalar, a matrix that is symmetriacal about the diagonal, and an antisymmetric matrix having only off-diagonal elements. These can be understood physically as follows: the scalar is the symmetric coupling constant J that arises from isotropic exchange as well as isotropic dipolar contributions. The second one is the matrix $\widehat{D}$ which contains the main contribution of the dipolar interaction – namely

the part that arises from anisotropic interaction – and the possible anisotropic exchange. The third component is the interaction matrix $\vec{E}$ that describes the antisymmetric exchange and dipolar terms which will not be discussed further here. In well-resolved single crystal studies, all matrix elements of $\widehat{I}$ might be extractable by the EPR experiment. However, to separate the contribution from the dipolar and exchange interaction often requires additional information such as the geometry of the interacting molecules.

Under certain experimental conditions one or a few particular terms dominate the spin-spin interaction and thereby facilitate an interpretation of the spectra. One example is the fast tumbling of a paramagnetic species in solution provided that the concentration is high enough to observe intermolecular interaction. The molecular motion averages out the antisymmetric and anisotropic contributions and only the isotropic term J remains to be analyzed. The dipolar contribution can be estimated by evaluating the first term in eq. 2.42 which requires an assumption on the interspin distance. The g-values are generally extracted from other experiments, e.g., the diluted case. As the isotropic dipolar contribution is only large for considerable g-anisotropy it is often neglected and the isotropic part of eq. 2.44 solely attributed to the isotropic exchange interaction in eq. 2.43.

The mathematical description of the dipolar and exchange interaction given applies explicitly to just two paramagnetic centers acting with each other. The example of the fluid solution already implies that in many systems the interaction is not limited to two centers. In a powder with a random distribution of molecular orientations, with respect to the magnetic field, all possible pair interactions overlap in the spectrum, complicating the analysis. However, in many cases the spectrum is still governed by pair interactions due to the strong distance dependence of the interactions involved, and can be interpreted in this simplified way. Two effects that lead to broadening and narrowing of the observed EPR signal in disordered samples shall be mentioned here.

In the solid state, the dipolar interaction leads to a splitting of the EPR line as discussed above. If the only free parameter is the angle between interspin vector and magnetic field, the EPR signal results from the integration over the angular distribution. The resulting line shape is called a 'pake pattern' in which the line splitting is still observable (e.g., [119]). If in addition to the angle, the interspin distance varies in the disordered system, then the resulting EPR signal consists of one broadened line. The linewidth is in a first approximation proportional to r_{12}^{-3} (r being now the average distance between spins 1 and 2). Thus, the average distance between the two spin centers can be determined if the dipolar interaction governs the linewidth.

The effects of a dominant exchange interaction mostly leads to line narrowing. In the picture of a pairwise interaction leading to spin exchange the isotropic exchange interaction can be properly described by identifying an effective exchange frequency ν_{ex}. The exchange interaction then influences the EPR spectrum in disordered or only partially ordered samples in the following way: the combined response of electrons that rest at many different positions within a disordered

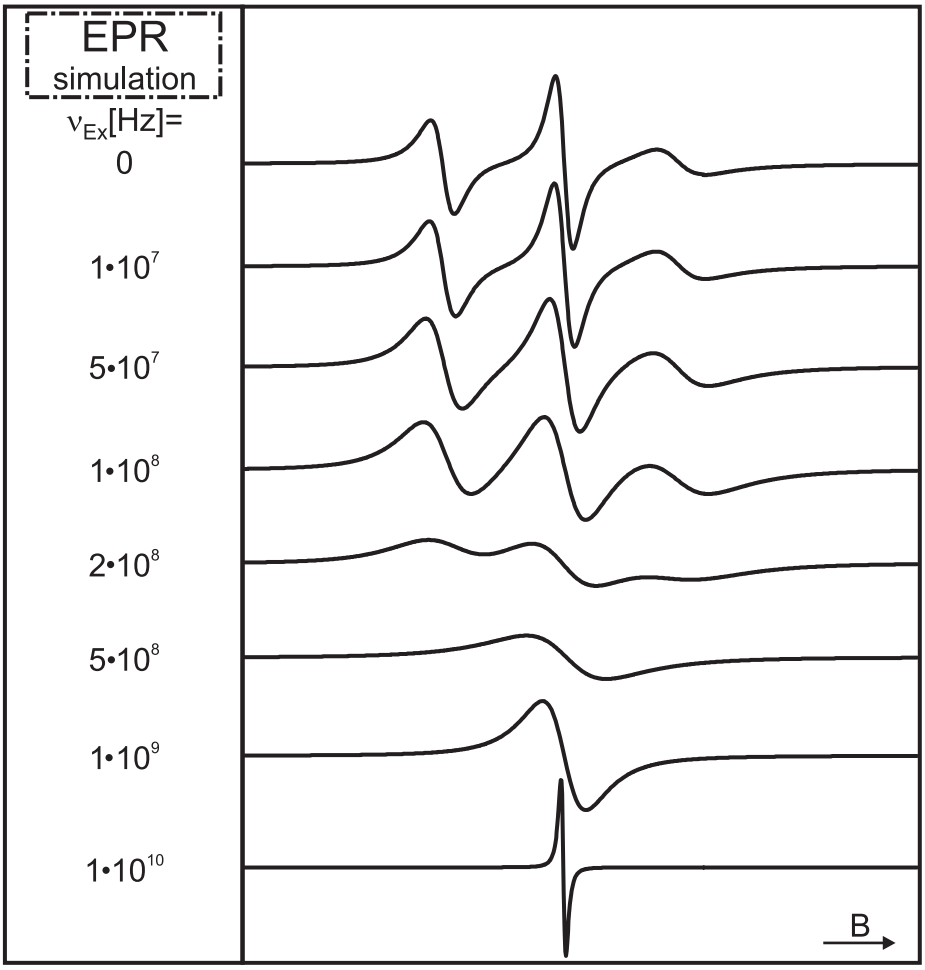

Figure 2.3: Loss of spectral information with increasing exchange interaction for a nitroxy radical ($S = 1/2$ and $I = 3/2$).

cluster in a short time interval is observed. This destroys g-anisotropy as each single electron occupies sites with different g-values during the time interval. Furthermore, an electron interacts with a statistical distribution of the possible nuclear spin states. The hyperfine coupling is averaged out and can no longer be observed. This also results in averaging of the dipolar interaction. The effect of an increased exchange interaction on the spectral features is simulated in Fig. 2.3. The difference in the linewidth depends on the distance between the spin centers and is directly proportional to the isotropic exchange frequency [102].

In conclusion, dipolar and exchange interactions can be used to study the interplay of paramagnetic centers. While the first reveals important information on distances and geometrical orientations, the latter additionally allows access to dynamics information. However, the additional terms in the Hamiltonian describing the system complicate a full analysis as they increase the number of unknown parameters and can especially in the case of disordered samples lead to a loss of spectral information.

2.1.7 Why High Field EPR

Most EPR spectra are taken at X-band (9.5 GHz) and a smaller fraction at Q band (35 GHz). Higher frequencies were for a long time difficult to implement as the necessary microwave components were not available. However, early attempts to use higher frequencies by Lebedev and coworkers in the late 70s [59] were soon followed by others [30, 31, 98, 151]. In 1996 the first commercial high frequency spectrometer (W-band, 94 GHz) made the technique also accessible to laboratories who wanted to apply higher frequencies without developing their own EPR spectrometer [118]. In this section, the different advantages of using higher fields and frequencies in EPR spectroscopy will be briefly discussed, with focus on properties relevant to the sample class used. General overviews are found in the references provided [28, 45, 64, 80].

Spectral Resolution. The fundamental reason for high frequency EPR is enhanced spectral resolution for magnetic field dependent parameters. The splitting δB_0 of two lines with g-factors g_1 and g_2 is described by:

$$\delta B_0 = \frac{h\nu}{\mu_B}\left(\frac{1}{g_1} - \frac{1}{g_2}\right) \tag{2.45}$$

As eq. 2.45 shows, δB_0 is proportional to the microwave frequency. The increase in spectral resolution from X-band to W-band is schematically shown in Fig. 2.4. This can be important in two different cases: Either the g-anisotropy of one species is too small to disentangle the principle components at X-band but is resolved at higher frequencies or different species with similar g-values overlap at X-band but can be distinguished at higher frequencies. In both cases it is not rare that the relative difference $\delta g/g$ does not exceed $10^{-4} - 10^{-3}$. Assuming a frequency of 10 GHz, and the free electron g-value, the splitting δB_0 is between 0.2-2 G. If the linewidth ΔB exceeds δB_0 the species cannot be separated. To

allow distinction between similar species with ΔB between 1 and 10 G the common X-band frequency is too small. Increasing ν by a factor of 10 permits to discriminate between those species. This is the case by going from X-band to W-band spectroscopy. Of course, it is only true if the linewidth ΔB does not increase with frequency. It has been shown experimentally that for a wide set of species the linewidth does not change significantly between 10 and 150 GHz [44].

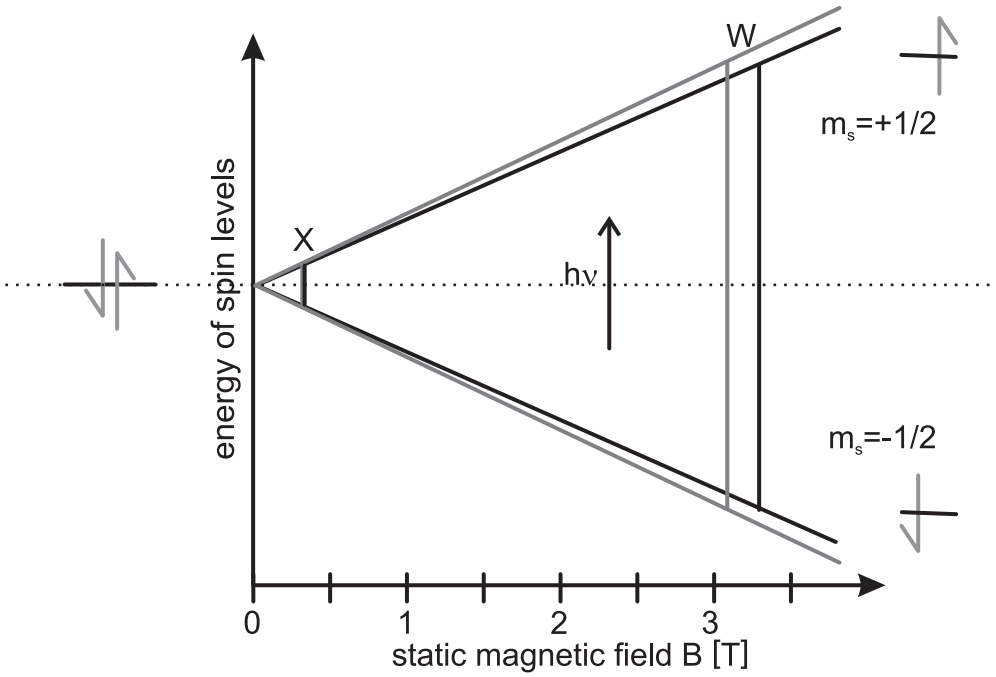

Figure 2.4: Shown is the increase in spectral resolution for higher frequencies as the resonance position of two different paramagnetic sites denoted by gray and black drift further apart with increasing field.

Weighting of Interactions. It was already mentioned in section 2.1.3 that the derivations of simple expressions for the energy eigenvalues in the case of electron Zeeman splitting and the hyperfine interaction are only valid in the 'high field' approximation. Only within this approximation does the first order perturbation theory give appropriate results, in which case the quantum numbers of the states can be described by the simple product function $|m_S, m_I\rangle$. The other extremum at zero field is defined by coupling $\vec{S}$ and $\vec{I}$ to a total angular momentum $\vec{F}$. In general, $(2K + 1)$ F-states exist. K always represents the smaller of the two angular momenta I and S. Assuming isotropic hyperfine coupling, the energy separation between different F-states is given by:

$$\Delta E_{F \to F+1} = a(F + 1) \tag{2.46}$$

In the special case of a paramagnetic species with $S = 1/2$ two F states result with $F = I \pm 1/2$. Instead of expressing the energy separation in dependence

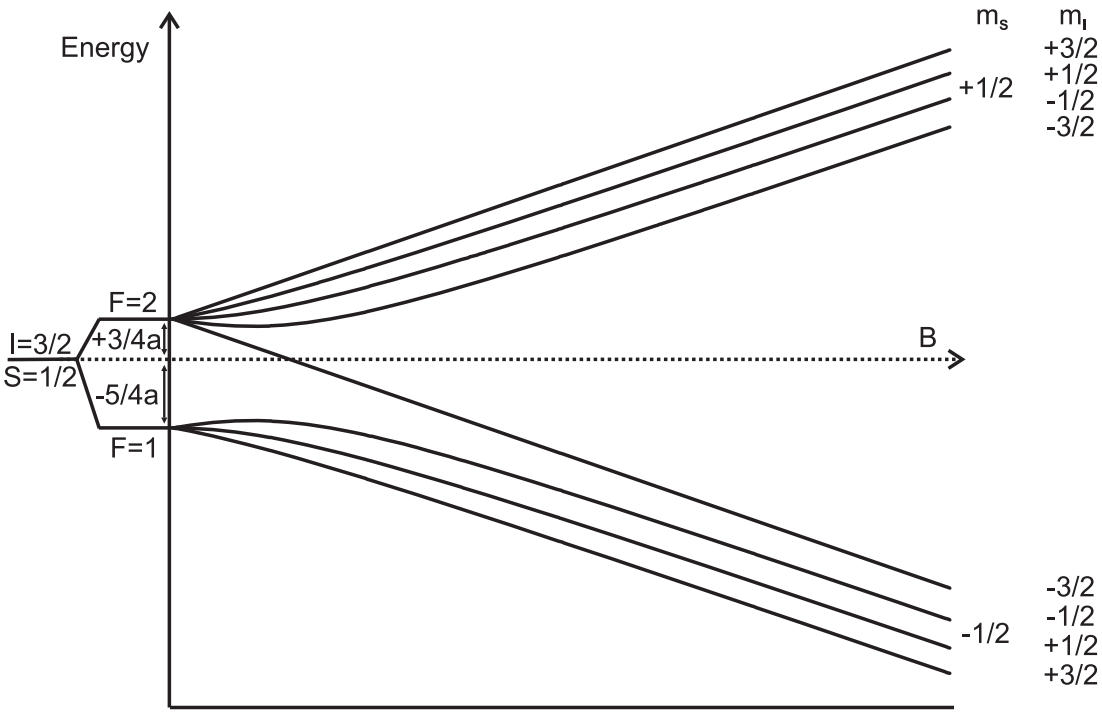

Figure 2.5: Energy splitting of gold atoms ($S = 1/2$ and $I = 3/2$) on terrace sites of MgO thin films at zero and intermediate field values, parameters were taken from [164], B aligned parallel to surface normal.

of F as in eq. 2.46, ΔE can alternatively be calculated from the nuclear angular momentum I:

$$\Delta E_{F \to F+1} = a/2(2I + 1) \tag{2.47}$$

This situation is shown for Au atoms in Fig. 2.5 on the left. A description of intermediate fields, which are the so-called Breit-Rabi cases, is more complicated [27]. As is seen in Fig. 2.5, the states denoted $m_S = \pm 1/2$ diverge with increasing field, with the high field regime reached when the sublevels m_I run parallel. It can clearly be seen that at intermediate fields the transitions induced by $h\nu$ are not equidistant. A correct description for intermediate fields incorporates an admixture of the simple products where the common picture of EPR transitions taking place with $\Delta m_S = 1$ and $\Delta m_I = 0$ loses meaning. While the general Breit-Rabi case can only be solved numerically, it is informative and for some systems sufficient to treat only the hyperfine interaction with second order perturbation theory. In this case, transitions can be classified as $\Delta m_I = 0$ transitions and the second-order correction to the position of each line as compared to first-order treatment is given by (isotropic case) [152]:

$$\Delta B(m_I) = -\frac{a^2}{2g_i\mu_B\nu}\left\{I(I+1) - m_I^2\right\} \tag{2.48}$$

This clearly shows that all transitions are shifted downward and the g-factor does not coincide with the center of the spectrum. It can be obtained by fitting the data including second-order effects. If more than one nucleus is involved, higher-order effects do not only lead to a shift of the resonance position, but also to a further splitting of levels. In Fig. 2.6 the numerically solved simulation for gold atoms at X-band frequencies clearly shows different spacings between the lines as the hyperfine coupling constant is about 1/6 of the magnetic field used [164]. However, at W-band the ratio changes by a factor 10 and the hyperfine coupling can now be directly deduced from the spectrum.

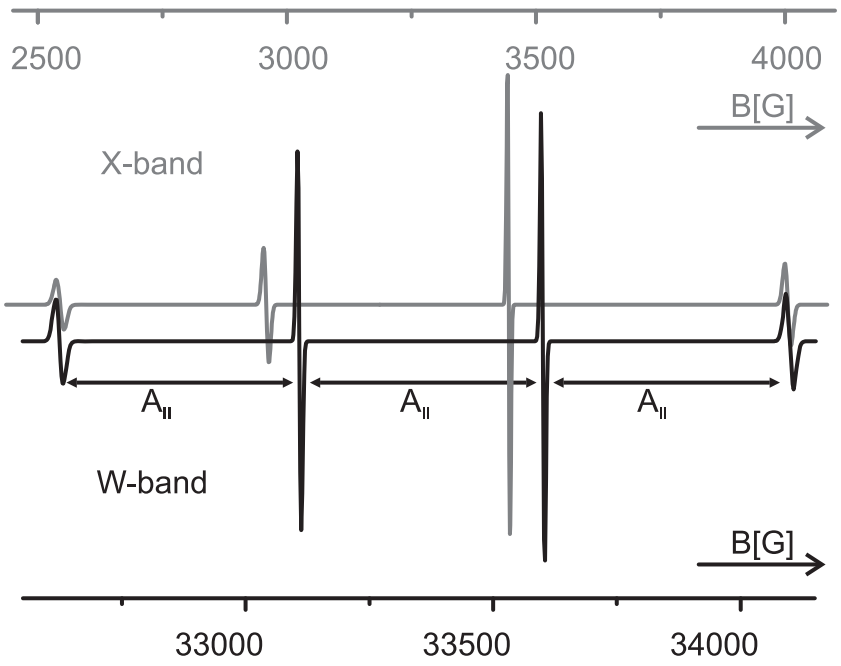

Figure 2.6: Simulation for Au atoms (defined as above) at W-band and X-band frequencies.

Sensitivity. An often praised property of EPR is its sensitivity. This is especially true if compared to NMR due to the larger magnetic moments of the former, and the quadratic dependence of intensity on the moment. The minimum number of detectable spins depends on many experimental parameters regarding the sample and the instrumentation used (see, e.g., [110,112,152] for details). For a rectangular X-band cavity (TE_{102}) the sensitivity is on the order of $10^{10}\frac{spins}{G}$ in ideal conditions [29]. The question of how the sensitivity evolves going to higher fields and frequencies is influenced by physical and technical aspects. There are two obvious physical reasons for the enhanced sensitivity. The first one is due to a shift in spin state populations by increasing the Zeeman splitting. For species close to the free electron g-value the Boltzmann distribution predicts a change of the population difference by a factor 10 if the external field is increased from 0.35 T to 3.5 T at room temperature. The second physical aspect is the frequency

dependence of absorption in a radiation field. While the Einstein coefficient B_e scales with ν^{-1}, the radiation density scales approximately with ν^3 leading to an expected dependence of ν^2 for the absorption [72]. Assuming a constant B_1 for all frequencies, detailed calculations for different sets of parameters show that the signal-to-noise (S/N) ratio increases as approximately $\nu^{7/4}$ if resonator resistance and not sample losses dominate S/N ([112] and papers therein). This value holds only for constant sample size and resonator volume as well as an identical noise figure for all amplifiers in the detection system. If resonator and sample size scale inversely with the frequency, S/N scales with $\nu^{-1/4}$ whereas for constant sample size but inversely reducing resonator size a scaling of $\nu^{11/4}$ is found. This little excerpt only contained dependence on resonator and sample size but shows already a huge spread in S/N improvement (or deterioration). The tedious task to experimentally verify the theoretical dependence has been done in the low frequency regime (250 MHz - 9 GHz) with the experiments coming close to the expected values but never reaching full enhancement [112]. In general, it can be stated that high frequency is certainly a great advantage if only small sample amounts are available, as might be the case for biological single crystal samples. Furthermore all systems implemented at W-band frequencies gained sensitivity to comparable X-band measurements but none of them come close to the predicted sensitivity (see, e.g., [29, 80, 111]).

Pulsed EPR. Another advantage of high frequencies is clearly seen in the field of pulsed EPR spectroscopy. Although such experiments are not included as part of this thesis, the setup described allows for a later extension with a pulse bridge. The main problem with pulsed experiments is that the dead-time τ of the resonator after a pulse has to be short compared with the T_2 relaxation times of the system. The gain by going to higher frequency is achieved by the fact that τ is inversely proportional to the frequency. If the system investigated allows pulsed X-band measurements at all the quality factor Q of the resonator which is directly proportional to τ has to be degraded artificially. With pulsed experiments at higher frequencies systems with shorter T_2 relaxation times are accessible.

2.1.8 The W-band Spectrometer and the Measurement Protocol

In this section the general functionality of the W-band spectrometer is outlined. Besides the resonator which was designed during this thesis and is discussed in detail in section 4.2, the EPR spectrometer consists of the Bruker ELEXSYS E600. The superconducting magnet integrated into the system was manufactured by Magnex Scientific and the corresponding control by Oxford Instruments (IPS 120.10). Control of the experimental parameters and data acquisition were conducted with the Xepr software provided by Bruker.

All microwave frequencies involved are generated by Gunn oscillators. The Gunn effect was first observed by J. B. Gunn in 1963 [62]. The effect was found in

GaAs, which is still the most commonly used material in gunn diodes. It is found in semiconductors whose conduction band allows the electrons to sit not only in the low-mass high velocity state - the global minimum of the conduction band - but also in a higher mass lower velocity state on the edge of the Brillouin zone ([32] and papers therein). In an electric field, accelerated electrons are scattered into the high-mass low velocity state by interaction with the crystal lattice. This leads to a decreasing slope in a current-voltage plot which relates to a negative differential resistivity. Due to the different mobilities of the electrons in the two states, local inhomogeneity created by partial excitation does not vanish but is amplified. This leads to the formation of dipole domains. The domains travel through the semiconductor crystal in a manner that is influenced by the electric field, and are registered at the anode as current pulses. The resulting microwave frequency depends on the drift velocity of the domains and the length of the semiconductor. To use a gunn diode as a stable microwave source it is put into a suitable resonator in which the resonator determines the output frequency, which must be higher than the gunn frequency. By proper superposition of direct and alternate voltage, the whole gunn diode is put in a state of negative differential resistivity which increases the generation of oscillations effectively. The assembly of Gunn diode and resonator is called 'Gunn oscillator'. The small variability of the microwave source just described leads to the common practice in EPR experiments of keeping the frequency stable and sweeping the magnetic field.

The used frequency of approximately 94 GHz corresponds to a wavelength of 3.2 mm and requires a magnetic field of 3.4 T to observe species with a g-tensor close to the free electron value of 2.0023. The magnetic field is mainly created by a superconducting magnet with a maximum field strength of 6 T. To avoid sweeping the superconducting magnet during measurement an additional electromagnet is used with a sweep range of 600 G. The details of the magnet setup are discussed later as the magnet design strongly influences the entire experimental setup (chapter 3). The main components of the EPR spectrometer are shown in Fig. 2.7.

The W-band frequencies are generated by heterodyne mixing. The bridge system only differs from a Bruker X-band bridge by replacing the X-band circulator with the W-band bridge. The intermediate frequencies (IF) generated by a Gunn oscillator are between 9.2-9.9 GHz. They are split in reference and signal arm. The signal arm is attenuated such that the sample is irradiated by the highest power possible that does not saturate the system yet. After a chosen attenuation - the maximum power output is 4 mW - the signal arm enters the W bridge. A second Gunn oscillator generates a frequency ν_0 of approximately 84.5 GHz. This frequency is kept constant at all times by phase locking. It is mixed with the incoming signal arm to yield a final microwave frequency of approximately 94 GHz which enters the circulator at port 1. The microwave leaves the circulator at port 2 and travels to the resonator. The light which is reflected from the resonator reenters the circulator at port 2 and reaches the downconverter via port 3. ν_0 is subtracted and the resulting intermediate frequency signal is amplified before it

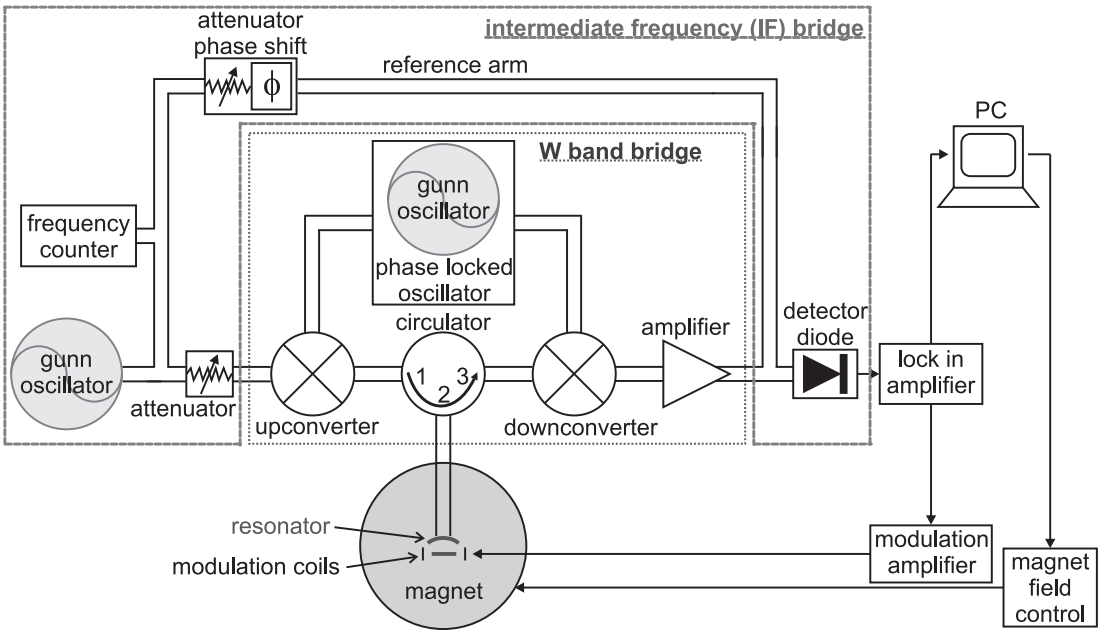

Figure 2.7: Diagram of the EPR spectrometer.

is guided back into the IF bridge onto the detector diode. In order to maximize the sensitivity, the detector diode needs to be biased. Therefore the reference arm is used with appropriate attenuation and the phase adjusted to the signal arm.

The IF bridge further houses an automatic frequency control (AFC) which measures the difference between the output frequency and the one necessary to keep the resonator properly tuned (not shown in Fig. 2.7). The AFC can then change the properties of the Gunn oscillator in a small range to keep the resonator on resonance. The control signal coming from the AFC can be read out and used for further manipulation as will be seen in section 4.2.4.

To obtain an EPR spectrum the resonator is tuned first. By changing mechanical parameters (details are found in section 4.2.2) the reflected power of the resonator is minimized. The resonator is coupled critically if the reflected power vanishes independent of the incident power. The spectrum is then measured by sweeping the magnetic field while keeping the frequency constant, and recording the response of the resonator. If the magnetic field value coincides with a transition between two spin states, additional microwaves are absorbed in the resonator. This alters the reflecting behavior of the resonator. The change in reflected power equals a change in current at the detector diode. The absolute deviations in the diode current are very small. Therefore the detector signal is not directly used as signal. Instead the static magnetic field is modulated with a fixed known frequency (here 100 kHz). The diode current is rectified phase sensitively by a lock-in amplifier. This output signal relates the change of the measured signal with the magnetic field. The recorded spectrum represents thus

the first derivative of the absorption signal. The use of the lock-in technique leads to a strong improvement of the signal-to-noise ratio.

2.2 Infrared Reflection Absorption Spectroscopy

The absorption of infrared (IR) light by molecules not only allows chemical identification of the species but also reveals information about adsorbate-substrate interactions on surfaces as well as intermolecular interactions. The technique is based on vibrational excitations of the molecules interacting with the electromagnetic field. After a short description of the theoretical foundations underlying the excitation, the specific characteristics of IR on metal surfaces is pointed out. The chapter concludes with remarks on the principles of a Fouriertransform IR (FTIR) spectrometer.

2.2.1 Theory

The excitation of molecular vibrations through interaction with the electromagnetic field can be treated with time dependent perturbation theory (for details see, e.g., [6]). The perturbing term is the inner product of the electric field vector $\vec{E}$ and the electric dipole operator $\vec{\mu}$ that is to say

$$\mathfrak{H}^{(1)} = -\vec{E} \cdot \vec{\mu}. \tag{2.49}$$

In the case of the incident wavelength being much longer than the dimensions of molecular vibrations the electric dipole approximation can be used. It assumes that the electric field component is a constant at the site of interaction. This is a valid approximation for all infrared frequencies. Inserting the perturbing term into Fermi's Golden Rule as was equivalently done for a spin transition before (eq. 2.27) leads to the following expression for the transition probability:

$$W_{i\to f} \propto \left| \vec{E_0} \cdot \langle \Psi_f | \vec{\mu} | \Psi_i \rangle \right|^2 \tag{2.50}$$

Ψ_i and Ψ_f being the initial and final state wavefunctions, respectively. The transition probability is only nonzero if the integrand in eq. 2.50 is totally symmetric. From this fact it can be deduced [6] that a vibrational excitation is only infrared active if the molecular dipole moment changes along the normal coordinate Q_k during the vibration that is

$$(\partial\vec{\mu}/\partial Q_k)_0 \neq 0. \tag{2.51}$$

Applying the harmonic approximation it further implies that only transitions between neighboring vibrational levels (v_n) can occur:

$$\Delta v = \pm 1. \tag{2.52}$$

2.2.2 IR on Metal Surfaces

In all IR measurements conducted here the adsorbate is close to a metal surface. This poses an additional selection rule – the metal surface selection rule (MSSR) – and asks for a certain geometrical orientation of sample and IR beam. As the transmittance of IR for metals is low, absorption by adsorbates on the surface is usually measured in reflection geometry. This technique is then called infrared reflection absorption spectroscopy (IRAS).

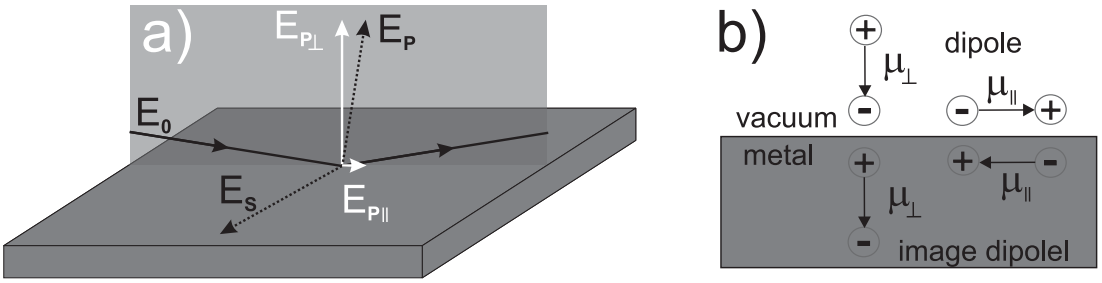

Figure 2.8: a) Decomposition of the electric field component on the surface b) Illustration of image dipoles created in the metal.

In Fig. 2.8 a) the decomposition of the electric field component E_0 of the incident beam on the metal surface into p- and s-polarized (E_P and E_S) components is shown. As can be deduced from Fresnel equations the s-component undergoes a phase shift near π for all possible incident angles on a metal surface [49]. Therefore the incident and reflected beam practically cancel on the surface. The amplitude of the p-polarized vector depends strongly on the incident angle. Interference of incident and reflected light almost doubles the normal electric field component ($E_{P\perp}$) near the grazing angle compared to the incoming wave. The parallel component ($E_{P\parallel}$) of the p-polarized wave is several orders smaller than the normal component and does not contribute to the observed absorption. As there is no significant parallel component of the electric field on the surface the dynamic dipoles can only interact with the normal electric field component. Angles near grazing incidence are used to maximize $E_{P\perp}$.

This interaction between electromangnetic wave and the metal surface can also be understood in a dipole picture. The oscillating dipole moment of the electromagnetic wave creates an according image dipole in the metal surface. The dipole component perpendicular to the surface is amplified by its image dipole whereas the parallel components are canceled as seen in Fig. 2.8 b). Thus, only the perpendicular component of the electromagnetic wave contributes to the vibrational excitation. This dipole picture is also useful for analysis of the adsorbate-metal interaction. The vibrating molecule adsorbed on a metal surface induces a corresponding image dipole in the latter. Amplification and cancellation are equivalent to the light-metal interaction as depicted in Fig. 2.8 b). Again – this time for the molecule – only the dipole component perpendicular to the

surface remains.

In conclusion, the electrodynamic properties of the metal lead to the metal surface selection rule that states that only species with a dipole moment perpendicular to the surface can be detected and that the incident light needs to have a p-component in order to do so (e.g. [58, 71, 74]). This is also valid for an oxide film on a metal surface as long as the film thickness is small compared to the IR wavelength [71].

2.2.3 IR Frequencies and Intensities of Adsorbed Molecules

The interaction between adsorbate and substrate as well as within the adsorbate layer usually leads to a frequency shift compared to the gas phase value. The main causes for such shifts are briefly summarized (more details are found in e.g., [71, 74] and papers therein):

- Frequency shifts of the molecule by interaction with the substrate are induced by:
  1. mechanical renormalization: The coupling of the molecule to the (rigid) substrate leads to a blueshift that can be understood by using a simple model of masses and springs.
  2. the interaction of the dynamic dipole with its image dipole: The dynamic dipole moment induces an image dipole which in turn changes the local electric field of the molecule. This shifts the gas phase value downward to lower frequencies.
  3. chemical and electrostatic effects: This includes changes in the electronic structure induced by chemical bonding between adsorbate and substrate as well as charge redistribution due to electrostatic interaction.
- Frequency shifts by interaction within the adsorbate layer are induced by:
  1. dipole-dipole interaction: The direct coupling of neighboring dipoles as well as through-metal coupling interactions between adsorbed molecules shifts the frequency upward.
  2. chemical and electrostatic effects: The presence of neighboring molecules can change the electronic structure of the molecule considered as well as the substrate and thereby influence the interaction between them.

As the dipole-dipole interaction is only strong for molecules with similar vibrational frequencies, the last two effects can be differentiated by isotopic mixture experiments.

The coupling of neighboring dipoles not only influences their frequency but also the observed intensity. With increasing coverage the interaction between the molecules gets stronger and leads to depolarization. While at low coverage the

intensity of the absorption band grows linearly with increasing coverage the depolarization for higher coverages reduces or even inverts the intensity growth [71]. Furthermore, the intensities are strongly dependent on the geometric orientation of the molecules and their dynamic dipole moment due to the metal surface selection rule. An additional effect which can be observed if two different species with similar vibrational frequencies are present is 'intensity borrowing' [73]. By dipole coupling, the absorption intensity of the lower band is partially transferred to the higher frequency. This effect can be substantial and may lead to a larger intensity for the minority species. The sum of these effects leads to difficulties in a quantitative analysis of IR data.

2.2.4 FT IR spectroscopy

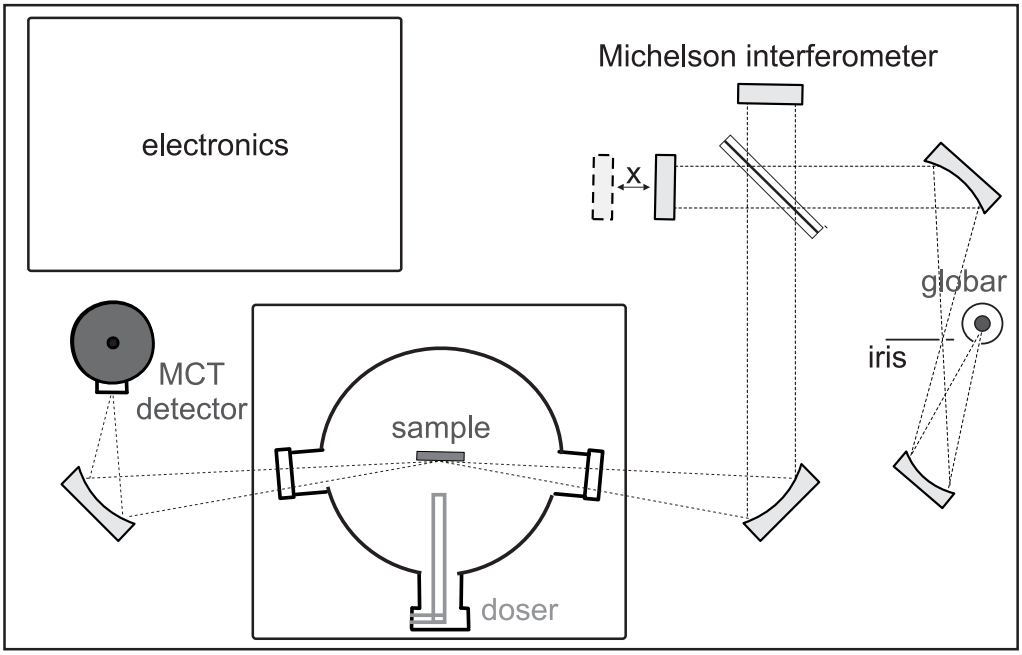

Figure 2.9: Schematic of a Fourier transform infrared spectrometer used in reflection geometry.

For data acquisition a Fourier transform (FT) IR spectrometer is used (Bruker IFS 66v/S). The setup is shown in Fig. 2.9. The infrared light is emitted by a SiC rod upon heating. This device, called a globar, covers a range of 560 to 8000 cm^{-1}. The light is guided into a Michelson interferometer, the core of the spectrometer. The semi-transparent mirror splits the light into two beams. One is traveling in a straight line to a movable mirror while the second one is reflected perpendicularly to its original orientation. It hits a rigid mirror. After reflection, both beams reach the semi-transparent mirror again where they interfere according to their path difference. The displacement x of the movable mirror determines the path

difference: $s = 2x$. The position is at all times determined by a He-Ne-laser. One beam exits the Michelson interferometer in the direction of the ellipsoidal mirror which focuses it onto the sample. The reflected beam is then directed onto a nitrogen cooled MCT detector.

The detected quantity is the total IR intensity as a function of the path difference. At zero path difference all wavelenghts interfere constructively. This leads to the center burst in Fig. 2.10 A). For a path difference $\neq 0$ some wavelengths can interfere constructively while others undergo destructive interference therefore the measured intensity is smaller than for $x = 0$. In an ideal experiment the interferogram in Fig. 2.10 A) would be symmetric. However, the measured interferogram is usually asymmetric due to phase shifts introduced by electrical and optical disturbances, and the phase has to be corrected for. To transform the intensity as function of the path difference into a function of the wavenumber a discrete Fourier transform is applied. The resultant is the single channel spectrum shown in Fig. 2.10 B). The intensity distributions of the single channel spectrum are mainly caused by the experimental setup including the emission function of the source, properties of optical elements used, reflectivity of the sample, and sensitivity of the detector. For this reason a single channel background spectrum, usually the adsorbate free surface, is measured. Division of the two single channel spectra results in the transmittance spectrum that is independent of the used parameters (Fig. 2.10 C)).

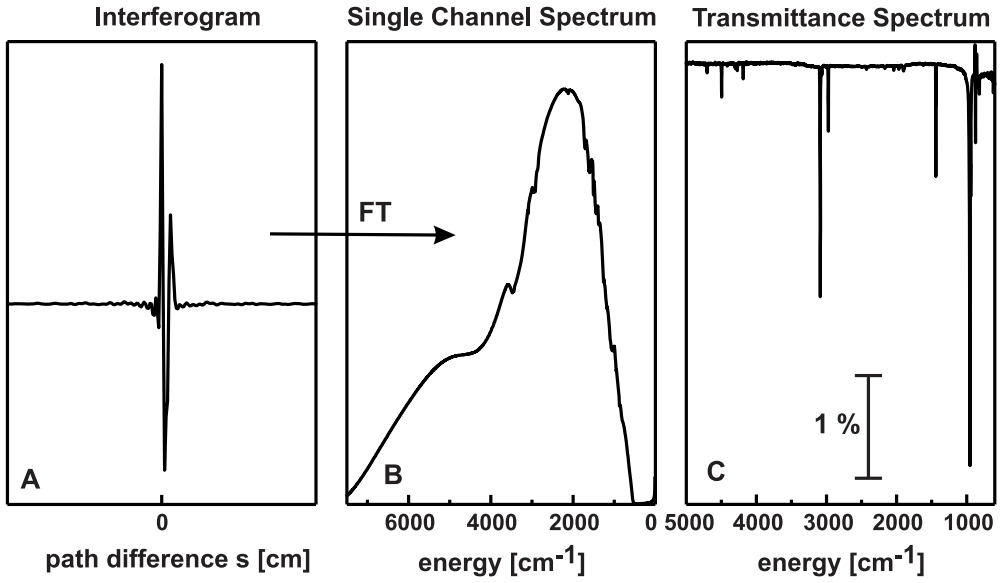

Figure 2.10: a) interferogram b) single chanel spectrum c) transmittance spectrum [50].

2.3 Scanning Tunneling Microscopy

Scanning tunneling microscopy offers the possibility to locally probe the geometric and electronic properties of a surface. Since the first implementation by Binning and Rohrer in the early 1980s [21] it has developed into a common technique for surface analysis. It images the local density of states (LDOS) in real space. In many cases, atomic resolution can be obtained. The technique is based on the quantum mechanical tunneling effect. The latter describes that a particle can cross a potential barrier higher than its initial energy with a certain probability (see, e.g., [6, 92]), and thereby travel through a classically forbidden zone. Depending on the polarity of the bias voltage, the electrons in STM tunnel from the sample under investigation to the tip or vice versa. The barrier can be either vacuum, air, or a liquid. In the quantum mechanical picture, a wavefunction overlap of the filled states on the tip side with the empty states in the surface takes place, or vice versa.This allows the electron to 'tunnel' through the barrier of high potential.

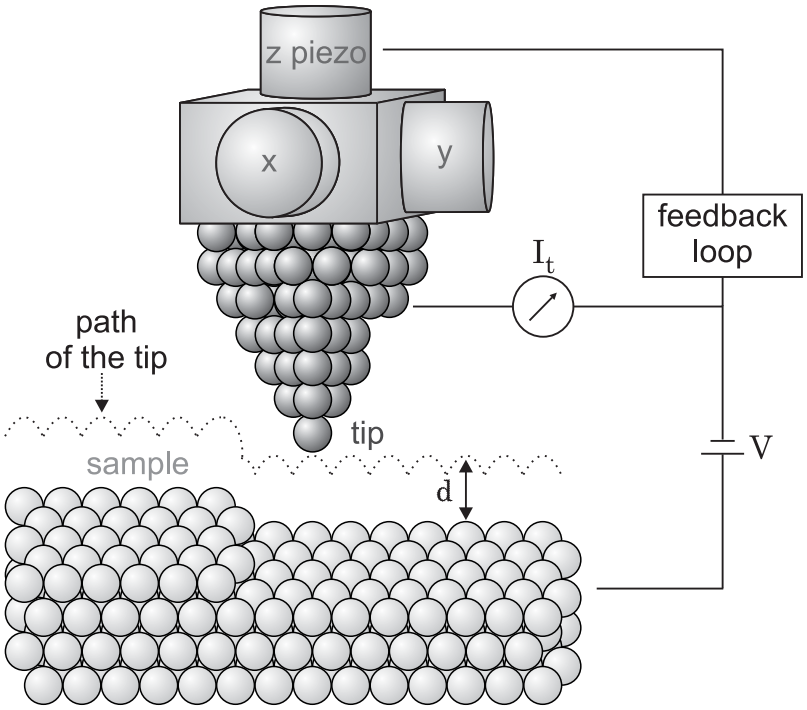

Figure 2.11: Schematic of the tip-sample interaction in STM.

In practice the probe is a 'sharp' tip that scans over a surface. The tip and sample have to be conductive to allow the flow of electrons and avoid charging. The basic idea of the experimental setup is shown in Fig. 2.11. The tip is brought close to the surface such that a tunneling current (I_t) is measured by applying a bias voltage (V) between sample and tip. To obtain currents in the pA to nA regime the distance (d) between sample and tip is on the order of a few Å.

For adjusting the tip position with sufficient accuracy piezo ceramics are usually employed. While the so-called 'z-piezo' regulates the tip height, the x- and y-piezo are used for lateral movement. Two different modes of operation are in principal possible. In the first, the separation between tip and sample is kept constant while scanning the surface. In this case the change in the current I_t is detected in dependence of the lateral position. In the second mode, I_t is kept constant by a feedback-loop while d is varied during scanning. The so-called constant height mode has the advantage of high scanning speed. However, the application is limited in the case of larger corrugations. Therefore, all images taken in this thesis were taken in constant current mode.

The tunneling current is proportional to the tunneling probability, which is exponentially dependent on d. Using a simple approximation, the tunneling current can be related to further measures as seen in eq. 2.53 [35]:

$$I_t \propto f(V) \cdot e^{-\beta\sqrt{\langle\Phi\rangle d}} \tag{2.53}$$

with f(V) being a function of the voltage between tip and sample, β being a constant, d denoting the aforementioned tip-sample distance, and $\langle\Phi\rangle$ being related to the work function of tip and sample. Assuming the simple case of a homogeneous metal surface at low temperatures, $f(V)$ is proportional to V; i.e. Ohm's law is applicable.

However, a full theoretical treatment of the tunneling interaction is difficult due to the missing translational symmetry of the tunneling junction as well as the number of contributing factors. Besides the tip-sample bias, V, and the distance the electronic states of the sample and the tip have to be described properly which includes knowledge of the exact tip geometry. Early theoretical models were based on one-dimensional perturbation theory. These can be traced back to Bardeen who described electron tunneling in a layer system consisting of metal, insulator, and superconductor [8]. He described the tunneling as electron transfer from an initial state on one electrode to a final state in the second one where the transition probability obeys Fermi's Golden Rule (compare eq. 2.27 and eq. 2.50). Tersoff and Hamann extended this model by assuming the tip to have s-character [43, 115]. By doing so, they could explicitly determine the transition matrix elements. These showed that the tunneling current, I_t, is proportional to the LDOS of the surface at the position of the tip. The model was later on refined to allow for p_z and d_z states [34, 35]. Although the treatment by perturbation theory implies a weak tip-sample interaction, and thereby a comparably large tip-sample distance, the approach was also successfully applied for smaller separations in the case of thin oxide films [66]. Obviously, to allow tunneling through thick oxide films high bias voltages have to be applied. This procedure can induce defects and morphology changes [130]. Therefore, the strongly insulating oxide films imaged with STM in this thesis are only a few MLs in thickness.

Chapter 3

Experimental Setup

The experimental setup for the equipment described here provided a number of design challenges to integrate EPR spectroscopy with more traditional UHV techniques. The final configuration of the system allows preparation of the single crystal, surface characterization with LEED, Auger, and STM, adsorption studies with IR spectroscopy, high pressure treatment, and the desired investigations with EPR spectroscopy. To understand the resulting system the considerations used in designing it are given in detail. As the main aim of the project is the integration of W-band EPR spectroscopy into a UHV setup, the spectrometer is the starting point for the following considerations. The working procedure of the spectrometer was already explained in section 2.1.8 and the X-band and W-band microwave bridges as well as the electronics are used in the common implementation manufactured by Bruker. However, adaptations to UHV have to be met at the site of measurement in our system. This is particularly critical for the magnet and the resonator which have to allow the precise placement of the sample in the center of the magnetic field center within a UHV environment. As the choice of a suitable resonator is one of the crucial aspects of the project, this issue will be addressed first. The principal setup of the resonator is given below in order to clarify the demands on the remaining system. A detailed discussion of the resonator design and its properties follows in a separate chapter (chapter 4).

3.1 Resonator for W-band EPR spectroscopy

Several types of resonators have been used at W-band frequencies, but before describing the resonators themselves, justification has to be provided why they should be used at all. A sample can be put directly into the waveguide and the signal is measured in transmittance. This is often done for frequencies still higher than W-band (e.g., [41]). However, the use of a resonator allows standing-wave patterns and thus increases the local energy density dramatically which, in turn, enhances the signal-to-noise ratio. Therefore, in the case of a limited total number of spins, as is the case for submonolayer surface species, a resonator should be used. A second advantage of a resonator is that its geometry determines the field

distribution within the resonator. In the ideal case the sample can be placed at an electric field node which is simultaneously at a magnetic field maximum. This maximizes magnetic transitions and shifts the competition between magnetic and electronic transitions in favor of the former.

The resonators used at W-band frequencies can primarily be divided into two classes depending on the number of modes present: single-mode resonators with the cylindrical cavity TE_{011} being the most commonly used and multi-mode resonators such as the Fabry-Perot resonator. The main advantage of single-mode resonators is the small cavity volume V_c which keeps the filling factor η high. η is defined by [110]:

$$\eta = \frac{\int_{\text{sample}} B_1^2 \, dV}{\int_{\text{cavity}} B_1^2 \, dV} = \frac{V_s \langle B_1^2 \rangle_s}{V_c \langle B_1^2 \rangle_c} \tag{3.1}$$

with V_s being the sample volume, and $\langle B_1^2 \rangle_c$, $\langle B_1^2 \rangle_s$ the average of the squared magnetic fields over the cavity and sample volume respectively. The filling factor is directly proportional to the sensitivity. Therefore, in general, higher sensitivities can be reached with single-mode resonators; for exceptions, e.g., when dealing with lossy samples see [80]. The dimensions of the cylindrical cavity are comparable with the wavelength which is about 3.2 mm at 94 GHz. A strict size restriction arises from the fact that the systems to be investigated are grown on metal single crystals. Metallic substrates have to be placed in an electrical field node as otherwise the field distribution is distorted by the presence of the metal. This restricts the lateral sample dimensions in a cylindrical cavity to an area of approximately 100×100 μm^2. A contribution of several different facets to the EPR signal is undesirable as the advantage of single crystal use – the well-defined orientation – would be partially lost. To avoid ambiguity only very thin samples can be inserted into the cylindrical cavity. In this case the EPR signal originates mainly from two out of the possible six surfaces. The proper mounting of such a fragile sample within the UHV setup and reliable measurements with the other integrating techniques employed would arouse extreme difficulties. In addition to the obstacles with sample preparation and handling, achieving ultra low pressure at sample site is also a challenge. The volume in the cylindrical cavity is delimited by metal walls and plungers. The possibility to insert slots into the walls is well known and exploited in electron nuclear double resonance (ENDOR) experiments [29]. Still, the pumping cross sections reached with such a resonator are very small and the pumping rate low. As there is no possibility to read the pressure in the desired volume the conditions at sample site would be ill-defined. The same arguments also exclude the use of open single-mode and loop-gap resonators which are also available for W-band spectroscopy (e.g., [4, 123]).

The alternative of using a multi-mode resonator was previously mentioned above. The frequently used Fabry-Perot resonator consists of two opposing mirrors between which reflection occurs. For the present application the metal single crystal under investigation can simultaneously be used as one of the Fabry-Perot

mirrors. Quite differently from the single-mode resonators this demands a rather large single crystal. This also poses some difficulty regarding sample handling in the UHV system which will be discussed in section 3.4. The shape of the mirror surface is determined by the requirement that the single crystal is planar. The second mirror used is of concave shape (reasons and details are found in section 4.1). The Fabry-Perot resonator belongs to the class of open resonators as there are no walls other than the mirrors delimiting the resonator. The lateral dimensions of the sample used are restricted by the surroundings, especially the need to maintain a UHV environment at the sample site in the magnet center. The extended dimensions in all three spatial directions as compared to the single-mode resonators lead to higher pumping cross sections although a direct pressure reading at the sample site is not possible for either type of resonator. In conclusion, the choice of a Fabry-Perot setup as resonator is based on the demands regarding sample size and handling as well as the need to maintain UHV conditions.

3.2 Design Considerations

After addressing the selection of the type of resonator to be used, the orientation between resonator and magnet has to be discussed. The magnet system consists of a cryogenically-cooled superconducting split coil for applying a static magnetic field of up to 6 T and an additional room-temperature Helmholtz coil for small field sweeps. The magnetic field points in horizontal direction. The magnet in the standard Bruker setup (at the time of purchase) has one bore along the vertical axis and two perpendicular, crossing horizontal clearance holes. The magnet center is at the crossing of the three bores. Schematic cuts through the magnet are shown in Fig. 3.1 a)- c). For clarity the magnet housing is omitted and only the split coil (blue), the resonator mirrors (red) as well as the vertical and one horizontal bore (dotted black line) are depicted. The diameters of the bores are of crucial importance in the current case. This is due to the fact that not only a common resonator has to fit into the bore but also a UHV housing at the sample site. Additionally, sufficient clearance must be allowed for transfer of the single crystal into measuring position in a UHV environment. The additional room-temperature coil is inserted in one of the horizontal bores. This reduces the inner diameter of this bore, in the standard implementation, to only 55 mm compared to the 62 mm diameter of the second horizontal bore. The vertical bore has a diameter of 60 mm. Bruker uses the vertical access to connect its resonators. In order to allow transport into the measuring position, the sample is mounted on a manipulator in the present setup. The overall travel length of the manipulator is determined by the distance between the magnet shell and center as well as the additional space required to transfer the sample onto the manipulator outside the magnet (the reason that a second manipulator is required in the system is described below). For mounting of the resonator as well as for bake out of the

UHV setup, the magnet and the UHV system have to be separated in order to isolate the helium cooled magnet from the baking parts. Using the vertical bore, lifting or lowering of magnet or UHV system had to be performed in this instance. The separation in horizontal direction is mechanically easier to conduct by simply mounting the magnet on rails, and it ensures better manual access than a vertical separation. For this reason the sample in the UHV environment is inserted through the horizontal bores. The disadvantage of the horizontal bores is the aforementioned reduced diameter of one bore due to the room-temperature coil. To gain space for the necessary UHV implementation within the magnet bore, the standard Helmholtz coil was replaced by one with a reduced sweep range but an inner diameter of 60 mm. In the current implementation the electromagnet covers a range of 600 G (instead of 800 G in the standard setup).

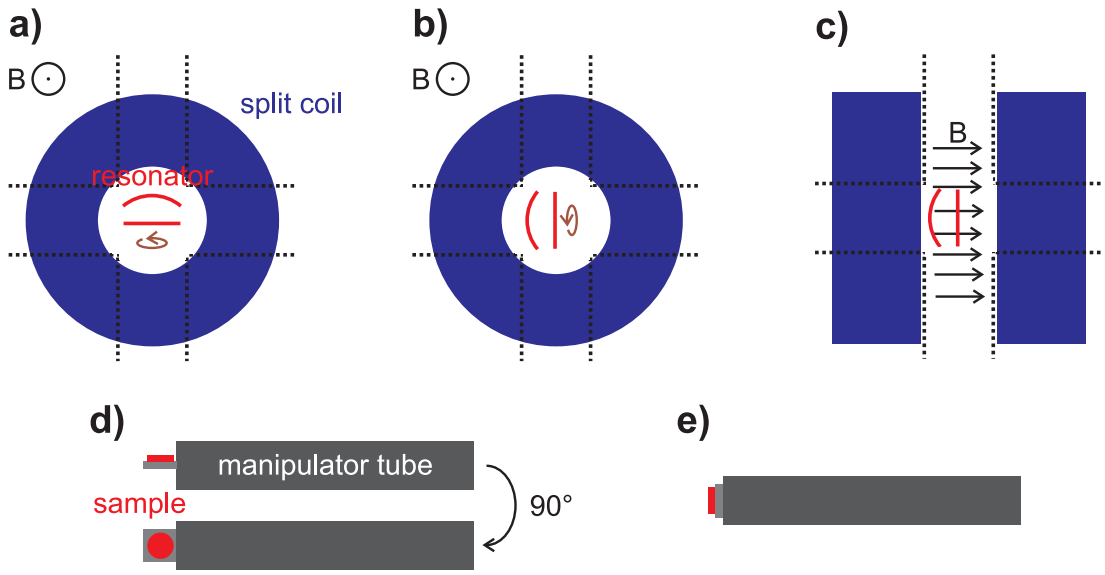

Figure 3.1: a)–c): possible orientations between a single crystal and the magnet; d), e): possible mounting of the sample on the manipulator; brown: rotations in the sample plane, dotted lines: magnet bores.

In addition to the question of which direction the sample should enter the magnet the issue of sample orientation has to be discussed. This will be done with the aid of the drawings in Fig. 3.1. In principal the sample plane can be oriented horizontally as seen in Fig. 3.1 a) or vertically as in Fig. 3.1 b) and c). In the horizontal orientation the magnetic field $\vec{B}$ will always be aligned with the sample plane. Rotation of the sample would allow probing of different directions in the surface plane, but measurement angles out of the surface plane are not accessible. This is different for a vertical orientation of the single crystal. The orientation of $\vec{B}$ to the sample in Fig. 3.1 b) is equivalent to a) but an additional orientation for a vertical sample is shown in Fig. 3.1 c). In this case, the magnetic field is aligned with the surface normal. Depending on the spin

system being investigated this additional orientation is necessary to identify all components of the g-tensor and other EPR parameters unambiguously. Knowing that both measurements with $\vec{B}$ parallel and perpendicular to the surface are of interest, the technical realization has to be discussed. As mentioned above, the sample is mounted on a manipulator to move it into the magnet center. In principal the sample can be mounted lying flat – in plane with the manipulator itself as seen in Fig. 3.1 d) –, or face-on as shown in e). Both orientations allow measurements in the surface plane as well as perpendicular to it. For the sample as mounted in Fig. 3.1 d) this is achieved by rotation of the manipulator tube. Possible orientations that can be reached include the sample-magnet orientation of Fig. 3.1 a) and c). For the sample mounted face-on, the orientations shown in Fig. 3.1 b) and c) are possible. In this case the change from incident parallel to perpendicular magnetic field is achieved by rotation of the magnet itself thus using both horizontal bores. The rotation in the surface plane for configuration Fig. 3.1 d) is challenging as it either requires tranfering the sample without visual access onto a rotation platform in the resonator or using a mechanism that allows rotation in the sample plane while mounted on the manipulator. For this reason configuration d) is discarded and e) used with the sample mounted face-on. In this case sample transfer from the manipulator is not only limited by the missing visual access but additionally by the limited space in the magnet center. Therefore, the sample sits on the manipulator during measurement and rotation is now simply performed by rotation of the manipulator. To allow rotation of the magnet about its main axis, it rests on a rotating platform. This setup then rests on rails and can easily be moved horizontally with a crank over a distance of 65 cm for bake out and mounting of the resonator. The possible magnet orientations and positions with respect to the remaining UHV setup are schematically shown in Fig. 3.2. Within this thesis only the orientation aligning the magnetic field parallel to the surface is used. The actions that must be taken to extend the system to the perpendicular orientation are outlined in section 4.2.2.

In conclusion, the careful analysis of possible access routes to the magnet and available orientations of the sample inside resulted in the design of a horizontally aligned manipulator with the sample mounted face-on. This design was realized and it influences the remaining setup as seen below.

3.3 General Setup

It was already mentioned that a second manipulator was required for the setup in addition to the manipulator that is used in the EPR experiment. The advantage of a single manipulator would lie in the reduction of the sample setup complexity as all connections for annealing, high voltage, and temperature reading could be rigidly implemented. In the current setup, however, the idea of relying on only one manipulator has to be discarded for the following reasons: The sample position in the EPR resonator predefines the orientation on this manipulator as face-on. STM

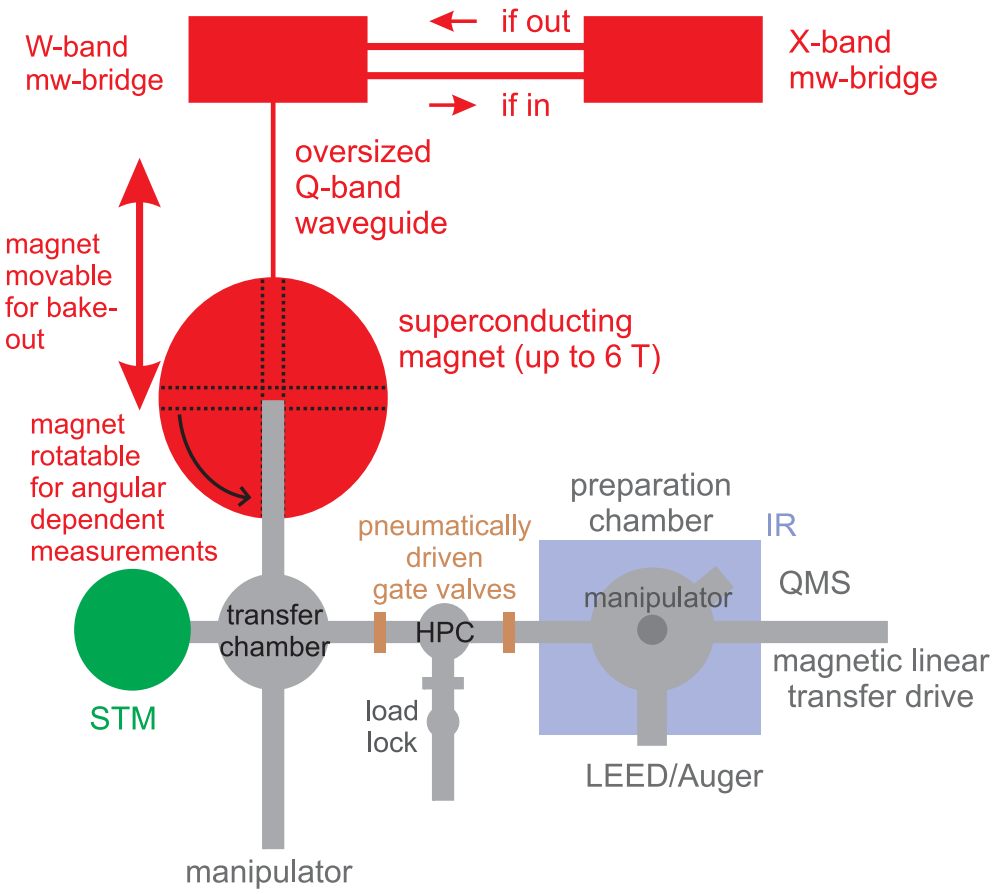

Figure 3.2: Top view of the UHV setup, schematic drawing.

setups that allow measurement with the sample mounted on a manipulator are of beetle type but they cannot operate horizontally. Therefore the sample has to be transferred from the horizontal manipulator into an STM setup. Another issue is the total length of the manipulator. Applying different techniques at the sample mounted face-on requires inserting the various probes in front of the single crystal at different positions of the setup for usage, and subsequently retreating them out of the way for free passage. This demands additional development as it cannot be achieved with standard available tools. Additionally, the overall travel length of the manipulator would be prohobitively for incorporating the different methods. The longer the manipulator gets the more susceptible the system is to vibrations. This is detrimental for EPR as the sample is mounted on the manipulator during measurement and the technique sensitive to vibrations. Thus in addition to the transfer necessary for the STM the remaining system is split into further components. The splitting has the advantage that preparation and measuring techniques can be placed in separable chambers. In practice, the UHV system is divided in three horizontally connected chambers which can be separated by pneumatically driven gate valves (Fig. 3.2 and Fig. 3.3). The preparation chamber

(PC) contains standard tools for the preparation of single crystalline surfaces as well as common techniques for surface characterization. The high pressure cell (HPC) allows sample exposure at elevated pressures. The transfer chamber (TC) connects the W-band EPR spectrometer and the STM to the system. A transfer rod mounted in the preparation chamber allows sample transport between the chambers. The UHV system together with the superconducting magnet as well as the microwave bridges for the EPR experiment are mounted on an optical bench (4x2 m, Newport, RS 3000). This bench rests on an active vibration isolation system to further reduce vibrations (HWI Scientific Instruments, AVI 400)(see section 4.2.4). Below, the shared pumping system of the setup is described before more detailed descriptions are given of the individual chambers and the sample setup.

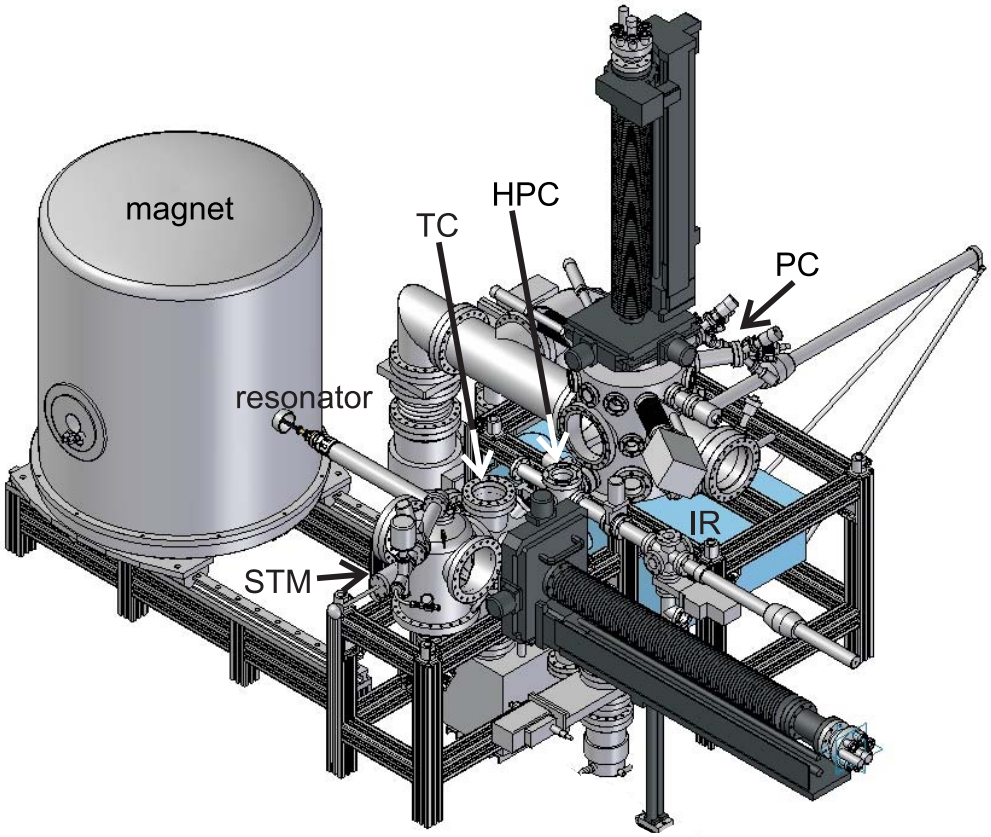

Figure 3.3: Schematic view of the multi-chamber system; PC: preparation chamber, TC: transfer chamber, HPC: high pressure cell.

3.3.1 Pumping System

As stated above the EPR resonator is sensitive to vibrations. The pump-system is therefore designed to minimize the vibrations created by the pumps while allowing individual pumping of the three UHV chambers. The first aspect leads to the use of only one roughing pump (a rotary pump) for the UHV system and the possibility to shut down all turbo molecular pumps (TMP) and the rotary pump if certain conditions are met. To reduce the noise level of the rotary pump it rests adjacent to the optical bench and connections are tightened to the concrete floor.

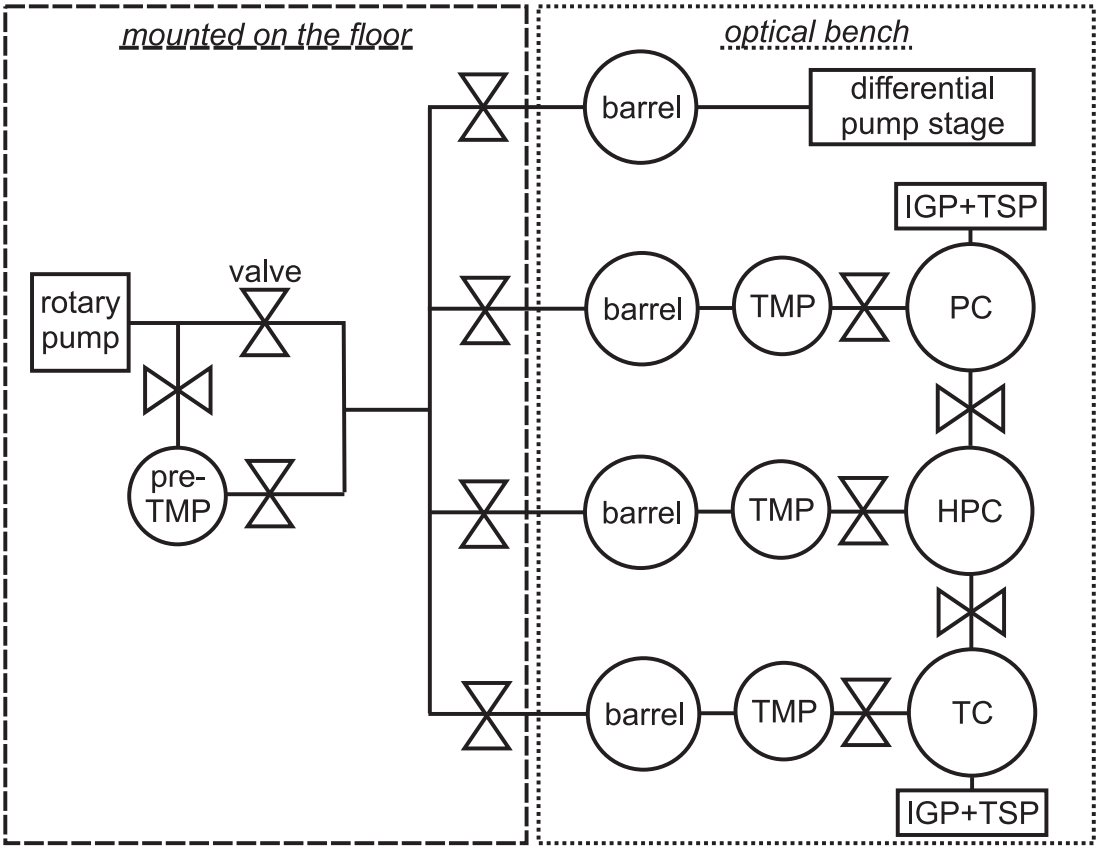

Figure 3.4: General overview of the pump-system and the main valves integrated into the UHV system.

The schematics of the pump-system are shown in Fig. 3.4. Each of the three UHV chambers has a TMP. These can be separated from the chambers by pneumatically driven gate valves. Each of the pumps is connected to a vacuum reservoir of 30 to 50 l volume. These reservoirs are located in the barrels indicated in Fig. 3.4. The fourth barrel shown is connected to the differential pump stages of the two manipulators. An additional TMP (pre-TMP) pumps the barrels either all at once or in turn with angle valves put between the barrels and the TMP. If run in automatic mode the control unit (Electronics Lab, FHI) for all pneumatically driven gate valves of the system selects the barrel having the highest

pressure and pumps it down to a stated value before the next barrel is connected to the pre-TMP. The vacuum reservoir lasts for about 8 h. During this time the rotary pump and the pre-TMP can be switched off. For pumping down of a chamber the rotary pump bypasses the pre-TMP and is directly connected to the corresponding barrel. Details for pumping the Fabry-Perot resonator are discussed later section 4.2.1.

The transfer and preparation chambers are additionally equipped with ion getter pumps (IGP) and titanium sublimation pumps (TSP) to maintain UHV. If no heavy gas load is applied, all TMPs can be switched off. The high pressure cell is in this case connected to one of the other chambers and pumped by it.

It is also important to consider that the magnet strongly interacts with the magnetic parts of the TMPs. The disturbance leads to overheating and shut down of the TMPs. To avoid this the TMPs of the transfer chamber and the high pressure cell are shielded against the magnetic field. Materials such as mu-metal are commonly applied as shields. Their advantages are extremely high maximum permeabilities and easy machining. However, the stray magnetic fields of up to 1 T saturate these materials. Instead the TMPs are surrounded by a cage of pure, magnetically soft iron with high maximum permeability and a saturation flux density above 2 T. The walls of the cages have a thickness of 2 cm with small openings for the necessary connections. The TMP of the preparation chamber suffers the highest stray fields due to its orientation and distance to the magnet. The initially installed iron cage around this pump induced a mechanical distortion of the superconducting magnet. The helium amount necessary for cooling increased by approximately a factor of 10 after the installation. This led to removal of the iron shield. For this reason the TMP of the preparation chamber has to be switched off if the magnetic field is on.

3.3.2 Transfer Chamber

The design of the transfer chamber is governed by the fact that the sample needs to be transferred into the resonator position with high precision. As discussed in section 3.2 the sample setup sits on a horizontally mounted manipulator with the sample face-on. The manipulator (PINK) is equipped with xy-stage, free rotation about the main axis, and a traveling distance of 70 cm. It has one motor each for z-drive and rotation. The manipulator houses a helium flow cryostat (KONTI Cryostat, CryoVac) whose mount is especially designed for the EPR experiment and will be described later (section 4.2). The chamber has a long extension in the horizontal direction opposite from the manipulator (Fig. 3.5). This extension arm fits into the magnet bore. It is made of titanium ensuring a relative magnetic permeability < 1.001 while the stainless steel used for the chambers has a specification of $\mu_{rel} < 1.05$. The resonator housing is directly connected to the titanium tube (see section 4.2). The waveguide as well as power connections for the resonator exit the magnet directly opposite from the titanium tube. Alignment of the manipulator, the titanium tube, and the

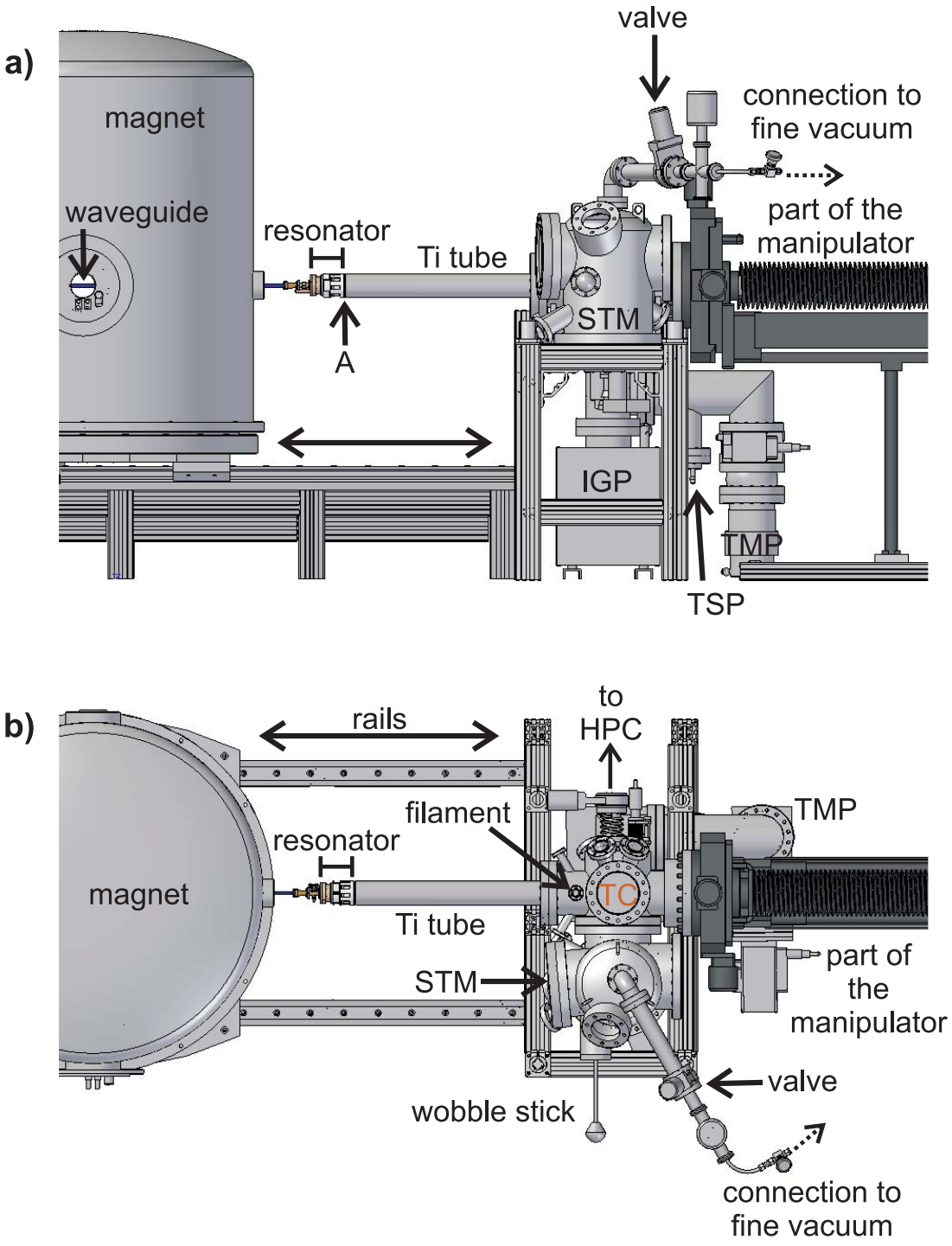

Figure 3.5: a) transfer chamber with magnet and STM chamber in the front, b) view of the transfer chamber from above.

magnet bores is of uttermost importance due to the limited space and the long travel distances involved. For this reason the chamber flanges for the manipulator and the titanium tube are specified to be aligned with respect to each other with less than 0.1° inaccuracy.

With the inner diameter of the titanium tube being 50 mm and the outer diameter of the manipulator tube being 44 mm the position of the latter for entering the titanium tube must be known precisely. Visual access is not possible in the closed setup. In practice, the coordinates for the sample being centered in the titanium tube flange are tabulated once. For this process the resonator housing with the concave mirror is removed. This way visual access to the sample in the titanium tube is possible. Consequently the sample position is determined with the chamber vented to the atmosphere. The sample is centered in the titanium tube at position **A** indicated in Fig. 3.5 a) and the coordinates are recorded for later use. In UHV one has to rely on those values. Furthermore the optimum sample position at point **A** of the titanium tube does not exclude the possibility of an unknown tilt due to cooling or slight differences of tightening the flanges which cause the manipulator to contact the titanium housing. For this reason the manipulator is driven slowly through the entrance of the tube. To ensure a correct alignment, a metal ring being slightly larger than the rest of the manipulator tube is mounted and electrically insulated from the sample setup (see Fig. 3.6). The ring acts as a sensor by creating a short if it touches the titanium tube. In this case the manipulator motors stop immediately and readjustment of the sample position is carried out.

The alignment of the bores in the magnet, as stated by the manufacturer, is less precise than that within the chamber. Still, two orthogonal horizontal orientations between magnet and titanium tube allow full insertion of the 54 mm thick titanium tube into the magnet bores, thus allowing EPR measurements parallel and perpendicular to the surface plane.

Besides enabling the sample access to the resonator the transfer chamber is directly attached to a standard VT SPM (variable temperature scanning probe microscope) chamber from Omicron which houses a storage carousel for up to nine samples and tips near the microscope. The current implementation only allows room temperature measurements due to the requirements of the sample setup. The Omicron system triggered the use of the Omicron standard sample plate. Its compatibility with the entire system is dealt with later (section 3.4). Sample transfer between the STM, storage carousel and manipulator is achieved by a pincer-grip wobble stick from Omicron (Fig. 3.5 b)).

On the bottom of the transfer chamber is an outlet to TMP, IGP, and TSP (Fig. 3.5 a)). The chamber further contains a leak valve for background dosing and a ionivac for pressure reading (not shown). A filament for annealing and electron bombardment is mounted on a z-translator and can be placed in front of the sample (Fig. 3.5 b)). The possibility to connect an electron beam evaporator is given. Viewports assure safe sample handling. A manual gate valve connects the transfer chamber with the resonator finevacuum system whose importance will

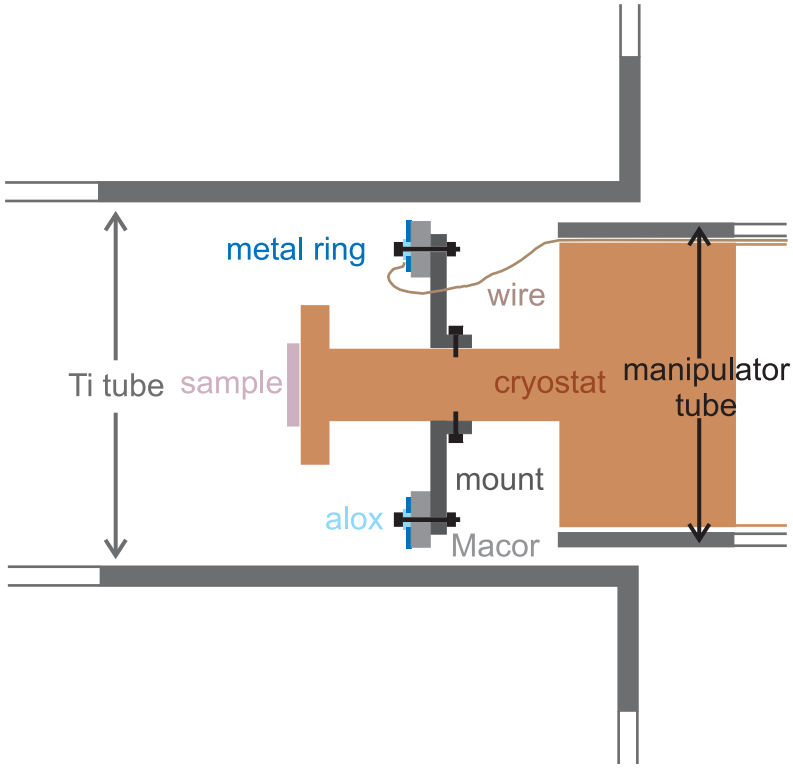

Figure 3.6: Schematic cut through cryostat and Ti tube; the metal ring creates a short to the UHV chamber if in electrical contact with the Ti walls.

be seen later (section 4.2.1). The sample is moved to and from the manipulator on the above mentioned transfer rod that connects all chambers.

3.3.3 Preparation Chamber

The preparation chamber consists of three levels as seen in Fig. 3.7. A vertical mounted manipulator (VAb) transfers the sample between the levels. It is equipped with an xy-stage for lateral movement, free rotation about the main axis, and a traveling distance of 60 cm. The manipulator houses a helium flow cryostat (KONTI Cryostat, CryoVac). The manipulator is equipped with two motors, one for linear drive and one for rotation. A control unit for all four motors of the two manipulators (the one of the preparation chamber and the one of the transfer chamber) was built (Electronics Lab, FHI) and provides a hand-held control for the system.

The topmost level of the chamber carries up to three electron beam evaporators (Omicron, EFM3 or triple EFM) for deposition of metals. A quartz microbalance (QMB, intellemetrics, IL 150) can be placed in sample position to calibrate the evaporation rate. A differentially pumped ion gun (DPIG, NGI 3000-Se, LK Technologies) is affixed to clean the single crystal surfaces. A quadrupole mass

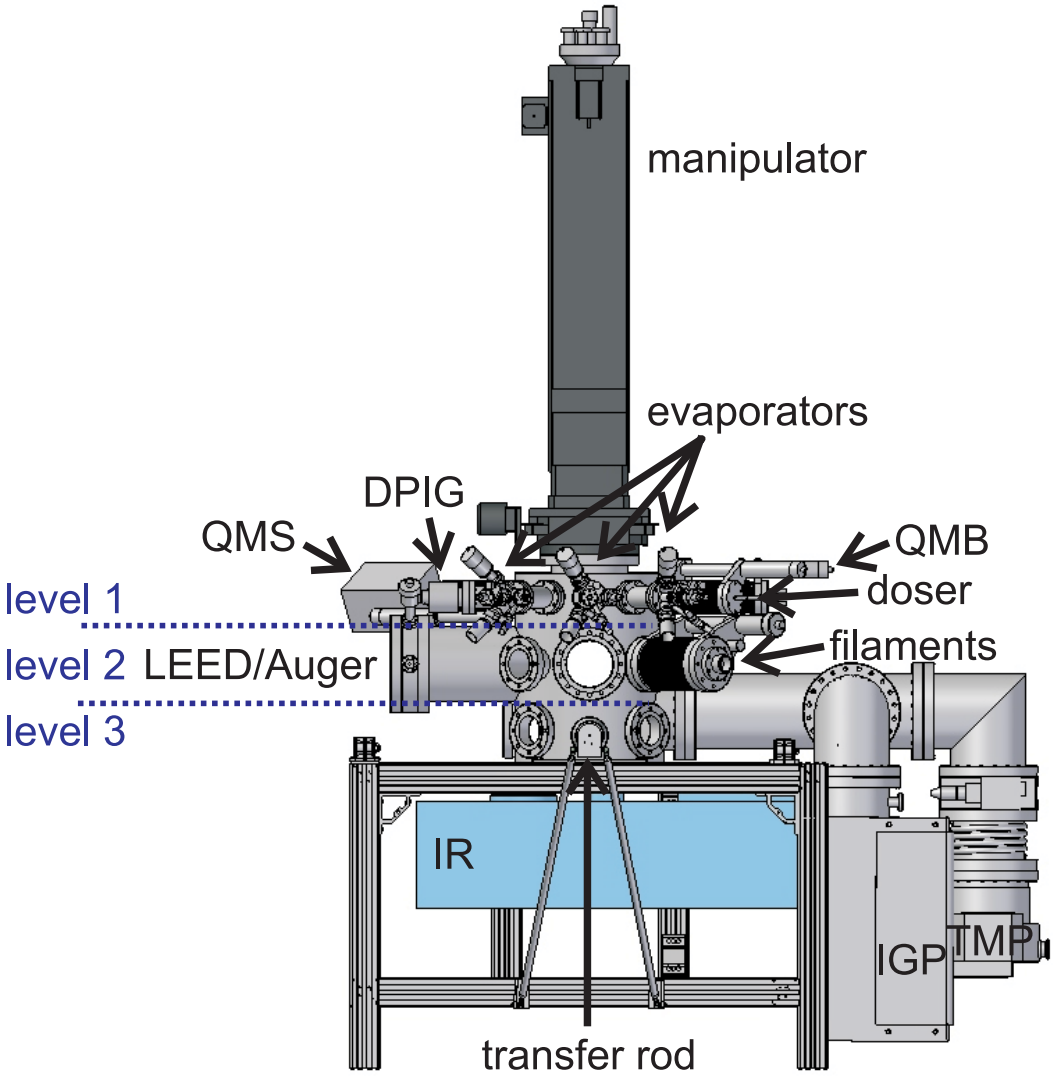

Figure 3.7: View of the preparation chamber, the connection to the HPC is on the rear side (not shown).

spectrometer (QMS) is attached (HIDEN). A pin-hole gas dosing system completes this level. The doser is described in detail elsewhere [50]. Core is a 0.125 mm thin molybdenum disc (PLANO) that has a 10 μm hole at its center which restricts the gas flow (Fig. 3.8). Level 2 comprises a combined LEED/Auger system (Spectaleed, Omicron) for observing and controlling sample preparation, two filaments for STM tip treatment and electron surface interactions mounted on a z-translator, and an additional leak valve (not shown). The third level carries the ionivac and the outlet to the pumping stack consisting of TMP, IGP, and TSP (hidden by the IGP). Opposite the port connecting the preparation chamber to the neighboring high pressure cell, the transfer rod (MLRM, VG) used for sample transport between the chambers is mounted. The head of this transfer drive provides a positive locking mechanism (Omicron) allowing to grab and release the sample plate eyelet for transfer and storage purposes. This mechanism includes two so-called anti-rotation rods ($\varnothing$ 2 mm) that have to be locked in a counterpart to allow grabbing and releasing of the sample plate. Not further specified here are the number and positions of the necessary viewports for safe sample handling.

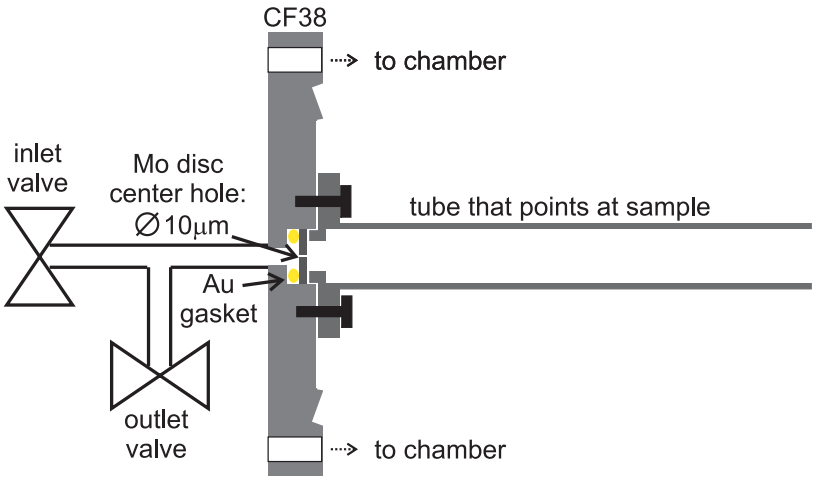

Figure 3.8: Doser in the preparation chamber.

Below the third level, a small UHV chamber is attached which is assigned for infrared measurements. A similar setup has been implemented and described elsewhere with comparable dimensions [50]. This chamber is lowered into the internal sample compartment of the vacuum FTIR system (IFS 66v/S, Bruker) which allows to use the internal MCT detector of the spectrometer (see section 2.2.4). The UHV chamber has two KBr windows which enclose an angle of 170° allowing the infrared beam to reflect from the surface at an angle of 6° from the surface plane. A topview of the IR chamber in the FTIR system was already shown in Fig. 2.9. In Fig. 3.9 a schematic cut through the IR UHV chamber is shown. Below the connecting flange to the preparation chamber a stainless steel plate is welded onto the IR chamber. This forms a vacuum seal to the internal

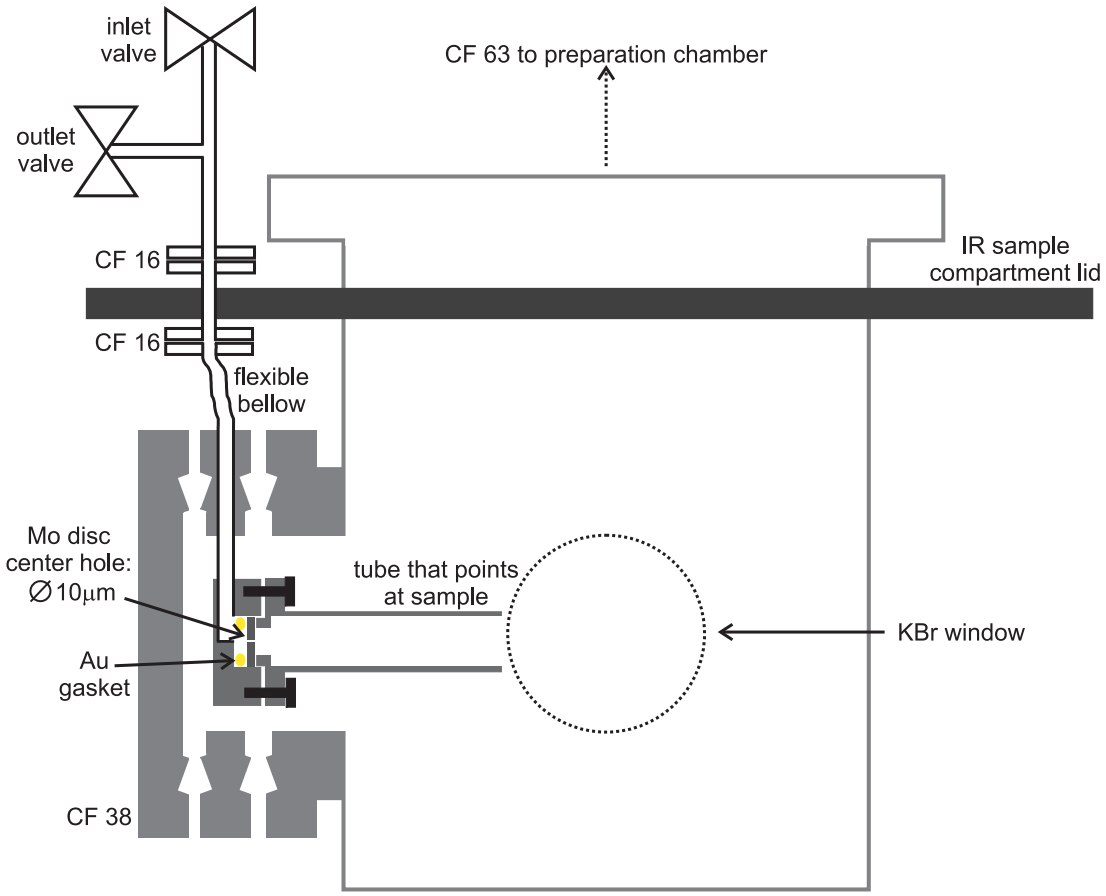

Figure 3.9: Schematic of the dosing system in the IR chamber.

sample compartment of the IR spectrometer. The construction of the pin-hole gas doser slightly varies from the one of the preparation chamber. Due to space limitations in horizontal direction the gas line leads through a double sided CF 38 flange to the actual doser. The gas is transported by only one tube that passes through the stainless steel plate. Pneumatically driven valves for the gas inlet and outlet are at ambient pressure for easier handling. They are electronically controlled which allows automatic opening and closing of the valves by specifying the desired dosing-time (Electronics Lab, FHI). The FTIR rests on a table that facilitates removal during bake out. For this purpose the table can be lowered by a vertical lift. The table rests on rails in the lowered position. The IR spectrometer can then be pulled away from the UHV-optical bench area by sliding the spectrometer along these rails.

Many of the tools mounted in the preparation chamber directly or indirectly produce charged particles. As the stray field of the magnet at the site of the preparation chamber can still be as high as 1 T at 6 T main field, these techniques cannot be used simultaneously with the magnet. LEED/Auger, the ion gun and the mass spectrometer are not used while high magnetic fields are present. The

ionivac reading is easily off by one order of magnitude. All these restrictions require that the magnetic field is only switched on shortly before an EPR measurement is performed and switched off afterward as soon as a new sample needs to be prepared.

3.3.4 High Pressure Cell

The high pressure cell is located between the transfer and preparation chamber. Similar high pressure cells have been described elsewhere [61]. The basic design is shown in Fig. 3.10. The main compartment is accessible by the transfer rod on the preparation chamber. A second, shorter transfer rod (MLRM, VG) is mounted perpendicularly to the first one. This rod can be used to retract the sample into a smaller compartment used as a load lock, which is pumped using the TMP. The load lock can be separated from the high pressure cell by a manual gate valve (see Fig. 3.10 b)). The mounted ionivac can be separated from both compartments together with the TMP by the pneumatically driven (p.d.) gate valve. Pumping down after sample change in the load lock is achieved by a roughing pump via a bellows valve (Swagelok). The main compartment is in this case connected to one of the other two UHV chambers.

For high pressure experiments, a leak valve for the gas inlet is attached onto the main compartment. To keep a constant gas flow, the chamber can simultaneously be pumped through the bellows valve on the load lock compartment. The sample itself rests on a vertically mounted z-translator which is equipped with a gold reflector lamp (Osram) and a sample holder made of Macor on top. The sample plate is clamped down by tantalum springs onto the Macor holder which provides a cutout for the plate. The crystal faces the reflector lamp. Earlier experiments within the Fritz-Haber Institute showed that heating up of the chamber walls can lead to undesired side reactions [61]. For this reason the main compartment is double-walled and can be water-cooled. The expected working conditions range up to 50 mbar oxygen pressure and sample temperatures of up to 500 °C [61].

The Macor holder of the main compartment provides a sample stage and a necessary anti-rotational device for the rods of the transfer drive of the preparation chamber. Reading of the sample temperature is possible by using the mounted thermocouple. Thermocouple and power connections for the lamp exit the chamber below the z-translator. During sample transfer, the Macor holder and lamp are lowered by the z-translator.

The sample plate fits into a shallow recess on the head of the short transfer rod in the high pressure cell. Springs made of molybdenum clamp the plate onto the head which further functions as an opening for the anti-rotation rods of the linear drive within the preparation chamber.

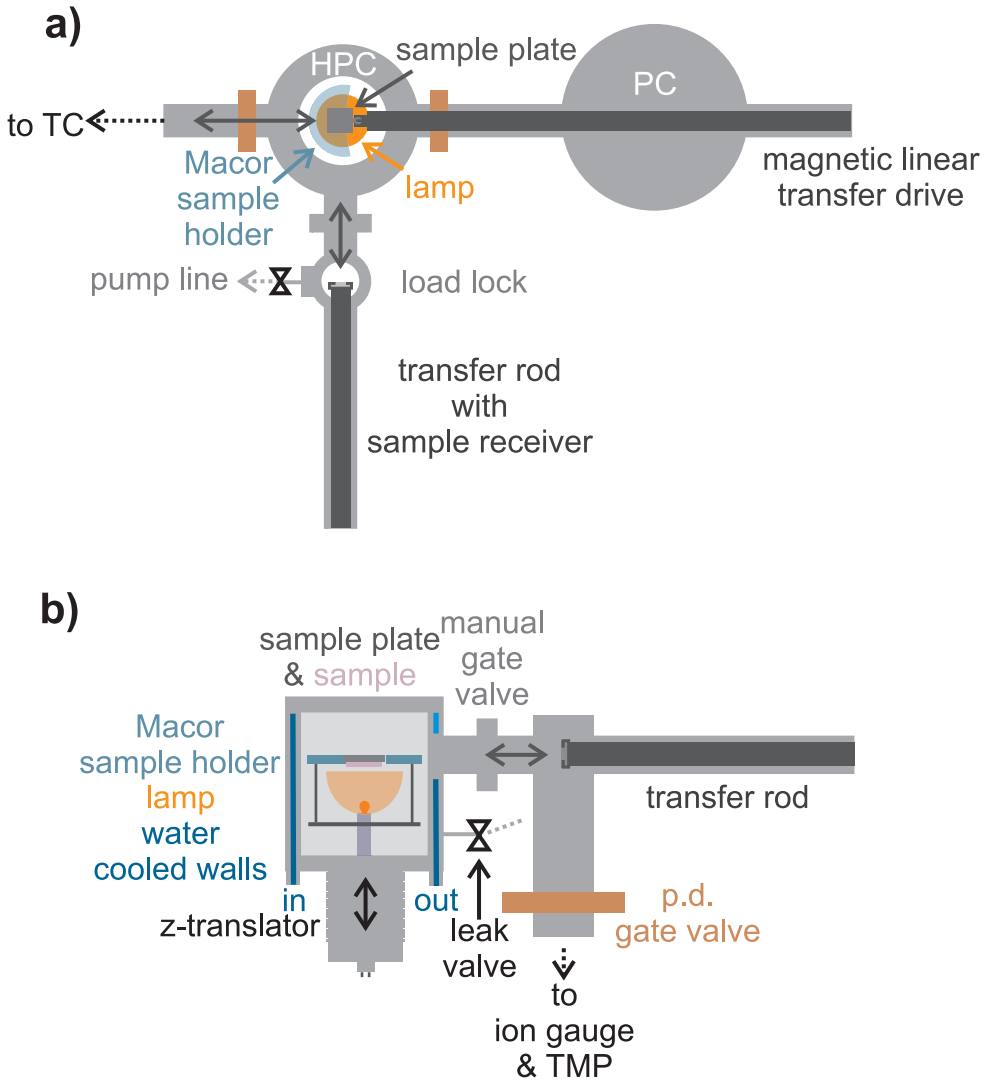

Figure 3.10: a) topview of the high pressure cell as the sample is inserted from the transfer rod of the preparation chamber, b) side-view of the high pressure cell with the sample in treatment position.

3.4 Sample Setup

For mounting the single crystal on a sample plate, there are several interrelated factors to consider. As pointed out previously the crystal is also the planar mirror of the Fabry-Perot resonator and therefore needs an extended surface area to minimize losses. However, the space in the magnet bore is limited and the diameter in the resonator narrows to 34 mm. As the maximum plate dimensions are close to those of the standard Omicron STM sample plate, this plate is used in the setup for reasons of convenience. Practically, the Omicron sample plate can be used with transfer mechanisms provided by Omicron, and therefore there is no need to develop a new transfer system. The single crystal dimensions on the sample plate itself are further limited by the need for proper electrical and thermal insulation. Additionally, there must be sufficient space on the edges of the sample plate for a contact area with the sample holders. In order to prepare oxide films on single crystal surfaces high temperatures are needed. This cannot be achieved by direct heating of the sample. Instead electron-beam heating is employed, requiring a filament close to the sample, where a high voltage is applied between the two. The sample is also typically biased at voltages up to 1000 V during metal evaporation in order to repel positive ions. Any potential sample configuration should allow temperature reading during preparation and measurement.

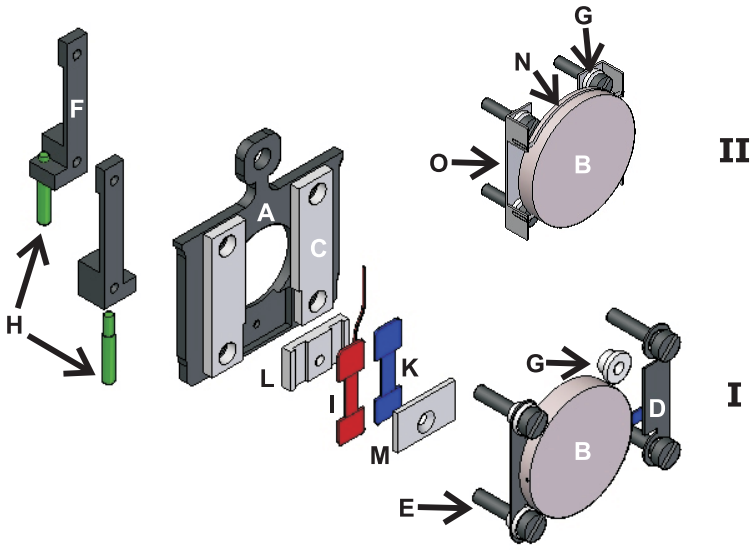

Figure 3.11: Sample setup, for details see text.

Taking these considerations into account, two sample setups emerged as shown in Fig. 3.11. The single crystal under investigation is mounted on the standard Omicron STM sample plate made of molybdenum (15×18 mm^2, **A**). The compromise of sample size is met by choosing the single crystal in the shape of a circular

disc measuring 12 mm in diameter (**B**). The crystal rests above two 1 mm sapphire pieces (**C**). These ensure electrical insulation. Additionally, the thermal conductivity of sapphire keeps the plate from warming too much during heating cycles while allowing proper cooling of the single crystal by the cryostat at low temperatures. The crystal has a thickness of 2 mm to facilitate mounting to the plate. Depending on the requirements of the sample preparations, two different approaches to attach the sample are applied. In both setups two parallel slits are cut into the single crystal for mounting. In setup **I** two flat springs made of molybdenum foil (0.2 mm, **D**) enter these slits and the foil is pressed onto the sapphire strips (**C**) by four cylinder-head bolts (M1.2, **E**). In setup **II** the crystal is held by two molybdenum wires (⌀ 0.25 mm, **N**) that are inserted into the slits. The wires are spot-welded to elbow-shaped foils (0.2 mm Mo, **O**) that are fastened by the cylinder-head bolts (**E**). In both setups the bolts are insulated from the sample by sapphire or alox bushings (**G**). The mating threads for the head bolts are not in the sample plate itself, but in two molybdenum holders on the rear side of the sample plate (**F**). To insulate the holders and the bolts from the sample plate sapphire or alox bushings equivalent to **G** are inserted into the sample plate holes from the rear side (not shown). This is necessary as the molybdenum holders (**F**) are further used as mounts for the thermocouple connections and shorting of the thermocouple leads has to be prevented. Temperature measurement is done using a type C (W/Rh 5%/26%) thermocouple. The thermocouple junction is inserted into a hole on the short edge of the single crystal and held there solely by mechanical friction. Pins of thermocouple material (**H**) are screwed into each of the molybdenum holders. The thermocouple wires coming from the sample are spot-welded onto the pins which serve as the contacts to counterparts on the cryostats of the preparation and the transfer chambers as well as the sample holder in the high pressure cell.

For heating and application of high voltage two tantalum pads (**I**, **K**) are mounted. A 1 mm thick sapphire with two slots for the pads fits into an eroded recess on the sample plate (**L**). On top of the pads rests a 1 mm sapphire strip (**M**). It has a countersunk hole and a mating M1 screw anchors the stack of sapphires and pads on the sample plate. This stack is higher than the 1 mm sapphire pieces insulating the crystal. Therefore the crystal is partially filed down on its back side in setup **I**. To use electron beam heating, a filament is spot-welded onto one pad and the sample plate (**I** and **A**). The wire thickness and composition is chosen such that pressure increase during heating is low and stability of the filament during oxidation is high. The second pad (**K**) is connected to one flat spring (**D**[**I**], **O**[**II**]) via a thin tantalum foil which allows biasing the crystal at a high voltage. For maximum pumping cross sections the sample plate has an 8 mm wide hole beneath the crystal.

As mentioned above the choice between setup **I** and **II** depends on the requirements of the sample preparation. The advantage of setup **I** is the well-defined orientation of the single crystal and sample plate. The wires in setup **II** allow some flexibility in sample mounting and it is not trivial to avoid a small tilt

between sample (**B**) and plate (**A**). The disadvantage of setup **I** is the direct contact of the sample (**B**) with the sapphire pieces (**C**). These pieces start degassing appreciably if the temperature rises locally above a 1000 K. This leads to an increase of the local pressure that can change the background pressure by up to one order of magnitude and is therefore counterproductive with respect to the crystal cleaning. Hence, in cases where high temperatures are required setup **II** is used.

3.4.1 Sample Mounting in the Preparation Chamber

The sample holder is attached to the primary heat exchanger of the cryostat via a copper block. The holder is made of molybdenum and its setup shown in detail in Fig. 3.12. The holder (**A**) has a cutout to fit two insulating sapphire

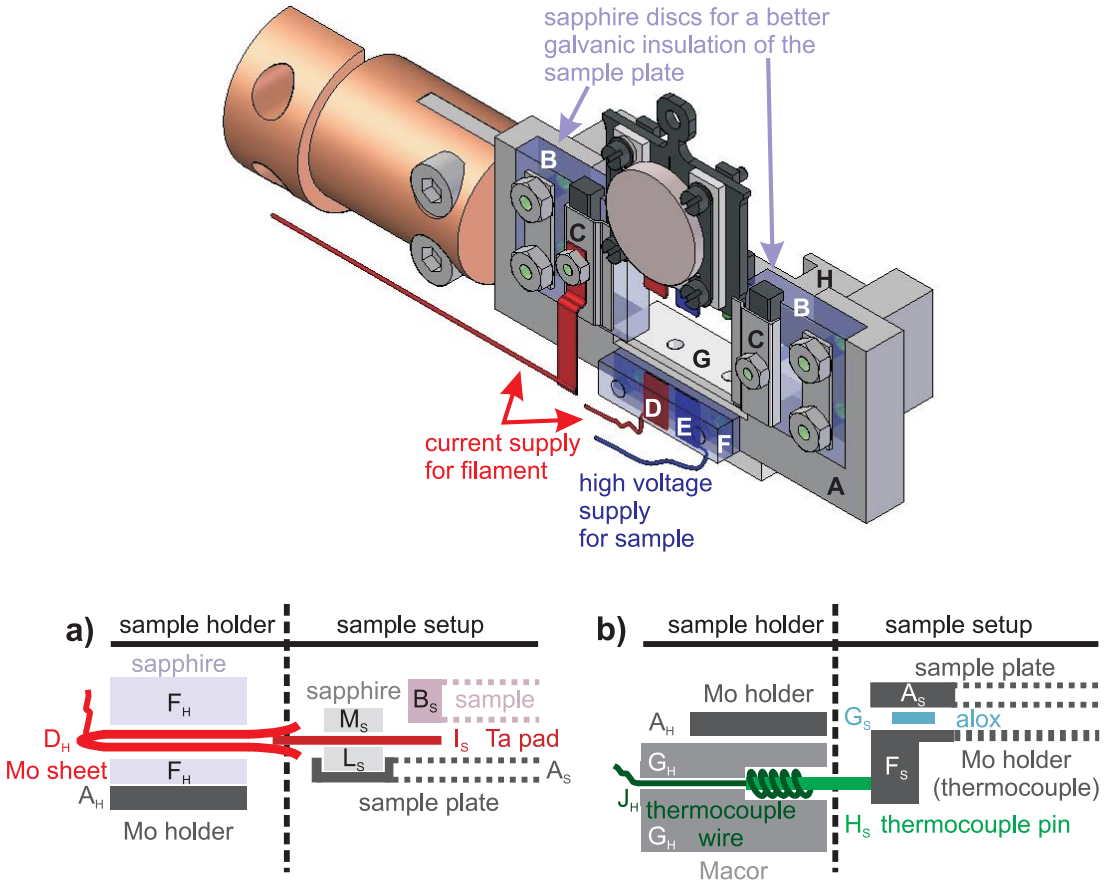

Figure 3.12: Sample holder in the preparation chamber; a) details of the power connections between the cryostat and sample, b) details of the thermocouple connection; the subscript 'S' denotes parts of the sample setup, 'H' those of the cryostat holder.

plates (**B**) which act as supporting area for the sample on its sample plate. The sapphire dimensions are 15×15×3 mm^3. The sample plate rests on the edges of

the sapphire with an overlap of about 1.8 mm on each side and is clamped onto it with molybdenum springs (**C**). One of the springs is used as a return line for the filament. 0.1 mm thick molybdenum foil is folded upon itself such that a double layer is formed where the tantalum pads of the sample setup insert between the two layers (**D**, **E**). A schematic cut along the foil - pad connection only including the parts above the sample holder plane is shown in Fig. 3.12 a). The two double layers are embedded in sapphire (**F**) which itself is screwed onto the molybdenum sample holder. The thermocouple pins of the sample enter two bores of 6 mm depth in a Macor block (**G**) with the Macor being screwed onto the molybdenum holder (**A**). Again, the details are shown separately in Fig. 3.12 b): a cut along one thermocouple connection including the parts below the sample plate plane. The bores of the Macor are filled with coils of thermocouple wire (**J**) which act as springs upon insertion of the pins. The thermocouple wires exit the Macor block through small holes on the rear side. Those as well as the three connections for the filament and high voltage then run to the according feedthroughs on the cryostat head. An aluminum block with a cutout for the anti-rotation rods of the transfer rod is mounted on the rear side of the sample holder (**H**).

Chapter 4

Resonator Setup

It was previously mentioned in section 3.1 that a Fabry-Perot resonator is used in the UHV adaption of the EPR spectrometer. This chapter begins with a theoretical introduction of Fabry-Perot resonators in general followed by a detailed description of the development of the resonator as it is used within this setup.

4.1 Fabry-Perot Resonators

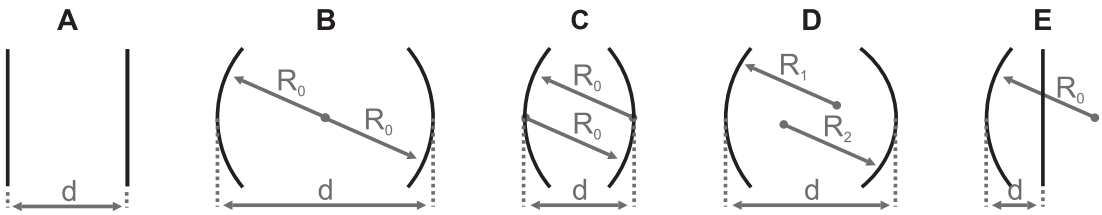

Figure 4.1: Different Fabry-Perot resonator geometries: A) plane-parallel, B) concentric, C) confocal, D) different curvatures, E) semi-confocal ($d = R_0/2$).

Fabry-Perot resonators always consist of two mirrors facing each other. The mirrors can be of different curvature or planar. Examples are shown in Fig. 4.1. Fabry-Perot resonators are most commonly found in laser implementations. An important difference between common lasers and EPR resonators is that when using microwaves the wavelength of radiation is no longer small in comparison to the dimensions of the resonator. Despite this difference, the theoretical explanation of the wave pattern is the same for both systems and the theory derived for optical applications also applies to microwave resonators.

To build a stable resonator – one that efficiently traps light – the following stability criterion has to be fulfilled:

$$0 \leq \left(1 - \frac{d}{R_1}\right)\left(1 - \frac{d}{R_2}\right) \leq 1 \tag{4.1}$$

with d being the separation between the mirrors and R_x the radius of curvature ($R_x = \infty$ for plane mirrors). This equation can be satisfied using a confocal setup ($R_1 = R_2 = d$) where the two mirrors share a common focus (Fig. 4.1 **C**). This is a highly metastable system as it corresponds to a singular point on the intersection of the stable and unstable areas. However, the confocal arrangement possesses very good sensitivity as will be seen below. In practice, the exact confocal arrangement is avoided also due to an existing mode degeneracy discussed below. Instead the distance between the mirrors is slightly decreased. Similarly, in the case of a plane and a concave mirror a nearly semi-confocal setup is the preferred arrangement (Fig. 4.1 **E**, [81]) which obviously fulfills the criterion in eq. 4.1 well. For this implementation a Fabry-Perot resonator consisting of one concave and one plane mirror was selected for the following reasons: The systems to be investigated consist of para- or ferromagnetic species that are created by chemical reaction, electronically induced, or deposited on single crystalline oxide films grown on metal single crystals. The advantage of using single crystals is that their defined orientation allows species in different geometric environments to be disentangled. A well-defined single crystal requires a planar surface. In order to place a planar metal single crystal in the center of a symmetric Fabry-Perot resonator the same restrictions apply as for a sample in the cylindrical cavity (see section 3.1): To place the single crystal in an electric field node it has to be very thin compared to the microwave length. This hampers a simple handling within the UHV system. However, a much simpler solution exists by using the metal single crystal itself as one mirror. In principal, the second mirror could be either plane or concave. The disadvantage of a resonator with plane-parallel mirrors is that their diffraction losses are orders of magnitude higher than for a concave setup and more sensitive to proper alignment [26]. A semi-spherical setup is therefore more sensitive to alignment than the confocal resonator but far less than a plane-parallel resonator. A near-semi confocal arrangement was the idea behind the prototype of the first UHV resonator. Why a deviation from this distance to curvature ratio is appropriate in the current case is explained in section 4.3. The theoretical basis regarding Fabry-Perot resonators will be derived for two spherical mirrors and in appropriate cases commented for the semi-spherical setup used.

Starting with two spherical mirrors the modes in a Fabry-Perot resonator can be described by scalar Gaussian beam theory [33, 38, 81]. Here only excerpts of the derivation will be given. For coherent light a field component or potential u satisfies the scalar wave equation:

$$\bigtriangledown^2 u = k^2 u = 0 \tag{4.2}$$

with $k = 2\pi/\lambda$ being the propagation constant. The axis connecting the two mirrors is denoted by z. Then the following ansatz for a wave propagating along the z-axis is chosen:

$$u = \psi(x, y, z)\, exp\,(-ikz) \tag{4.3}$$

ψ describes the difference between a beam in the Fabry-Perot resonator and a plane wave and is a slowly varying complex function. Two major differences from the plane wave are the nonuniform intensity distribution and a curvature of the phase front in the resonator case. After insertion of eq. 4.3 into eq. 4.2 the latter can be solved for ψ. The solution for the Gaussian fundamental beam of the field component u can be written in the form [81]:

$$u(r,z) = \frac{w}{w_0}\, exp\left\{-\frac{r^2}{w^2} - i\left(kz + \Phi - \frac{kr^2}{2R}\right)\right\} \tag{4.4}$$

where $r^2 = x^2 + y^2$. $z = 0$ is located in the center of the resonator. Φ represents the phase shift between the Gaussian beam and a plane wave as a function of the z-coordinate of the resonator and is defined as:

$$\Phi = arctan\left(\frac{\lambda z}{\pi w_0^2}\right) \tag{4.5}$$

The exponential $exp\,(-\frac{r^2}{w^2})$ is the Gaussian beam profile shown on the right of Fig. 4.2 for the magnetic field component. The beam waist $w(z)$ is the radius at which the field drops to $1/e$ of its maximum on the axis. It can be calculated using:

$$w^2(z) = w_0^2\left\{1 + \left(\frac{\lambda z}{\pi w_0^2}\right)^2\right\} \tag{4.6}$$

where w_0 is the waist with the highest contraction of the Gaussian beam as shown on the left of Fig. 4.2. At this point the phase front is planar. Knowing the dimensions of a symmetric resonator w_0 can be calculated by:

$$w_0^2 = \frac{\lambda}{2\pi}\,\{d\,(2R_0 - d)\}^{1/2} \tag{4.7}$$

For a fixed radius of curvature the beam waist w_0 is maximized for $R_0 = d$. This corresponds to the confocal setup. If the finite size of the mirrors is taken into account this arrangement has also the lowest diffraction losses for a fixed Fresnel number N_f where the latter is defined as [81]:

$$N_f = \frac{a^2}{\lambda d} \tag{4.8}$$

with $2a$ being the mirror height as shown in Fig. 4.2. Thus, this setup combines high magnetic field concentrations about the resonator axis with low diffraction losses. For a semi-symmetric resonator w_0 in eq. 4.7 coincides with the planar mirror. To apply the equation to the semi-symmetric case $2R_0$ is replaced by R_0. The optimum w_0 is in such way obtained for a semi-confocal setup.

Although the phase front of the symmetric resonator is planar for $z = 0$ it is spherically curved for $z \neq 0$ in the region close to the resonator axis. The radius of curvature of the phase front is described by:

$$R(z) = z\left\{1 + \left(\frac{\pi w_0^2}{\lambda z}\right)^2\right\} \tag{4.9}$$

At the intersection of the phase front and the mirrors the surfaces of the latter are coincident with the former ($R(\frac{d}{2}) = R_0$).

Determining the real part of u in eq. 4.4 the single field components can be expressed by:

$$E(r,z) = \frac{w}{w_0}\, e^{-\frac{r^2}{w^2}} sin\left(kz + \Phi - \frac{kr^2}{2R}\right) \tag{4.10}$$

$$B(r,z) = \sqrt{\frac{\epsilon_0}{\mu_0}}\,\frac{w}{w_0}\, e^{-\frac{r^2}{w^2}} cos\left(kz + \Phi - \frac{kr^2}{2R}\right) \tag{4.11}$$

where ϵ_0 is the vacuum permittivity. These equations describe the field distribution for unpolarized light. As will be seen below the field in the Fabry-Perot setup used is polarized. Nevertheless, parameters such as the beam waist vary only slightly in value if polarization is included. It is the simplicity of the Gaussian beam theory that explains its use for the case of polarized light as well.

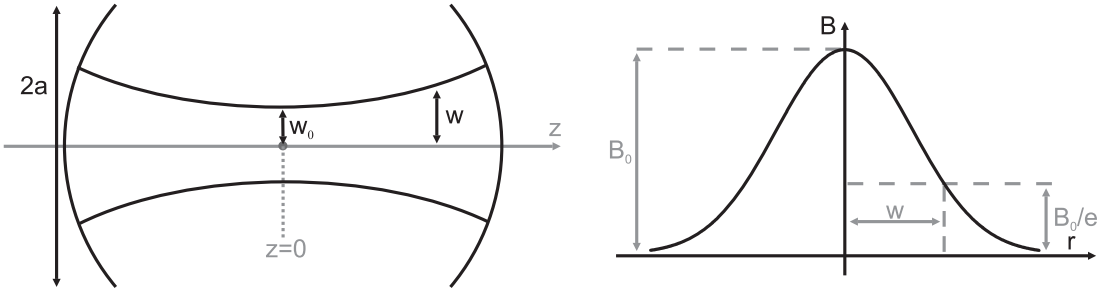

Figure 4.2: On the left: symmetric Fabry-Perot resonator with the beam waist indicated for the fundamental mode, on the right: amplitude distribution of the fundamental beam.

The derivation done so far only applies to the fundamental modes indexed by TEM_{00n} where n is the number of half wavelengths that fit within the resonator. In general circular modes are labeled TEM_{pln}, p indicating the radial and l the angular mode order. With the boundary condition that the phase shift from one mirror to the other has to be a multiple of π the resonance frequencies have to fulfill the following condition [81]:

$$\frac{2d}{\lambda} = (n) + \frac{2}{\pi}(2p + l + 1)\, arctan\left(\sqrt{\frac{d}{2R_0 - d}}\right) \tag{4.12}$$

By keeping d and R_0 fixed, λ can be determined for different values of p, l and n. In the special case of the confocal mirror with $d = R_0$ eq. 4.12 simplifies to:

$$\frac{2d}{\lambda} = (n) + \frac{(2p + l + 1)}{2} \tag{4.13}$$

The resonance frequency is the same for modes where n or p is increased by 1 or l by 2 indicating that the modes are highly degenerate. As mentioned above the confocal arrangement is metastable. By moving the mirrors slightly towards each other, degeneracy of modes and metastability are both avoided. The degeneracy argument also holds for the semi-confocal resonator as the mode picture is the same as for the confocal one with the planar mirror at the minimum of the beam waist. Therefore, a slight deviation from a semi-confocal arrangement is desirable.

A resonator with a fixed distance d is resonant for different frequencies ν. The minimum separation between two adjacent longitudinal resonances is given by the free spectral range $\Delta\nu$:

$$\Delta\nu = \frac{c}{2d} \tag{4.14}$$

An important parameter for the characterization of a Fabry-Perot resonator is the finesse $\mathfrak{F}$. It is the ratio of the free spectral range to the bandwidth of the frequency that is to say the full-width at half-maximum $\delta\nu$:

$$\mathfrak{F} = \frac{\Delta\nu}{\delta\nu} \tag{4.15}$$

Different resonators are also characterized using their quality factor Q. It is defined in the following way:

$$Q = 2\pi \times \frac{\text{Energy stored}}{\text{Energy dissipated per cycle}} \tag{4.16}$$

Experimentally Q is accessible by sweeping the microwave frequency through the resonance frequency ν_{res} and measuring the full-width half-maximum $\delta\nu$ of the dip. The three values are related by:

$$Q = \frac{\nu_{\text{res}}}{\delta\nu} \tag{4.17}$$

Q can be related to the finesse introduced in eq. 4.15 by:

$$Q = n\mathfrak{F} \tag{4.18}$$

with n representing the number of half wavelengths that fit within the resonator. As eq. 4.18 shows, the quality factor depends on the number of modes excited whereas the finesse is independent of the number of modes present. While it is very common in laser applications to describe the quality of a resonator by its finesse, in EPR spectroscopy the Q factor is more often used due to its long history with monomodal resonators. In the case of a Fabry-Perot resonator the Q factor is appropriate as long as the same mode is investigated. For different modes the Q factor should be converted to the finesse by eq. 4.18.

The scalar Gaussian beam theory described above inherently neglects the vectorial properties of the incident microwave. The result is a cylindrically symmetric field distribution. The light in the present setup however, is coupled into the Fabry-Perot resonator through a rectangular waveguide whose dominant mode is TE_{10}. As described in literature, the light is linearly polarized with the electric field component parallel to the short edge of the rectangle, one magnetic component parallel to the long edge, and one along the direction of propagation [110]. The polarization in the waveguide determines the polarization in the resonator, therefore the lines of field flux are not centrosymmetric in the Fabry-Perot setup used. If a W-band bridge from Bruker is implemented in its standard orientation the waveguide exiting the bridge is oriented with the electric field component in the vertical direction and the magnetic field consequently in the horizontal plane. In order to induce transitions the magnetic field component of the microwaves has to be perpendicular to the main magnetic field. As discussed in section 3.2 the main field is aligned horizontally. Therefore the W bridge in the present setup has to be rotated by 90°out of the normal orientation suggested by Bruker. Only this orientation, with the TE_{10} waveguide inserted horizontally into the magnet, has the correct field distribution to create the $\vec{B}_1$-field perpendicular to $\vec{B}_0$ at the sample site.

A vectorial solution of the field distribution in a Fabry-Perot resonator has been found applying the complex source-point method [40]. In this approach an electric and a magnetic dipole originating at the complex point $(0, 0, -iz_0)$ are the source of the electromagnetic field in the resonator. The electric dipole is oriented along the x-axis and the magnetic dipole along the y-axis. Using this ansatz, vectorial beam wave expressions for all components of the electric and magnetic field can be obtained. When doing this to order $(kw_0)^{-2}$, the components of the magnetic field $\vec{B}$ for the modes of a semi-symmetrical resonator can be given as [40]:

$$B_x = \sqrt{\frac{\mu_0}{\epsilon_0}} \frac{2xy}{k^2 w_0 w^3} e^{-\frac{r^2}{w^2}} cos\left(kz - 3\Phi + \frac{kr^2}{2R}\right) \tag{4.19}$$

$$B_y = \sqrt{\frac{\mu_0}{\epsilon_0}} \frac{w_0}{w} e^{-\frac{r^2}{w^2}} \{cos\left(kz - \Phi + \frac{kr^2}{2R}\right) - \frac{2}{k^2 w_0 w} cos\left(kz - 2\Phi + \frac{kr^2}{2R}\right) + \frac{3x^2 + 5y^2}{k^2 w_0^2 w^2} cos\left(kz - 3\Phi + \frac{kr^2}{2R}\right) - \frac{r^4}{k^2 w_0^3 w^3} cos\left(kz - 4\Phi + \frac{kr^2}{2R}\right)\} \tag{4.20}$$

$$B_z = \sqrt{\frac{\mu_0}{\epsilon_0}} \frac{2y}{kw^2} e^{-\frac{r^2}{w^2}} sin\left(kz - 2\Phi + \frac{kr^2}{2R}\right) \tag{4.21}$$

The same parameters are used as in the case of the Gaussian beam (eq. 4.5-eq. 4.9)

but they are now expressed in terms of the origin displacement z_0:

$$w^2 = 2z_0/k \tag{4.22}$$
$$w(z)^2/w_0^2 = 1 + z^2/z_0^2 \tag{4.23}$$
$$R(z) = z + z_0^2/z \tag{4.24}$$
$$\Phi(z) = arctan(z/z_0) \tag{4.25}$$

The resemblance of the field components with the scalar Gaussian beam (eq. 4.11) is obvious but now the vectorial dependence is expressed properly. In the xz-plane the magnetic field has only a y-component in agreement with the ansatz of a magnetic dipole aligned along the y-axis. The equations for the electric field components show the expected orthogonal behavior with respect to the B-field as well as the 90° phase shift along the z-axis (the expressions are found in [40]). In conclusion, the source-point method allows the vectorial character of the linear polarized light in the resonator to be analyzed. However, for many applications, such as the calculation of the beam waist and the distance between the mirrors, the scalar Gaussian beam theory is already sufficient.

4.2 Integration of the Fabry-Perot Resonator

In the following section a description is given as to how UHV conditions are achieved at the sample site within the resonator. The additional problem of coupling the microwaves into the system is dealt with afterwards. Fig. 4.3 shows a schematic drawing of the resonator depicting the half symmetric mirror arrangement and its connection to the remaining system. The planar mirror is the single crystal under investigation facing a spherical concave mirror. The resonator is connected to the microwave waveguide through a hole in the center of the concave mirror. It is not possible to integrate the whole resonator into UHV as the coupling hole is too small to pump the space behind it efficiently which would result in a permanent leak, preventing pressures in UHV regime. Instead UHV is only maintained at the crystal surface. The crystal and the concave mirror are separated by a quartz window (Suprasil). The requirements for the window are such that it should not have disturbing paramagnetic defects in the region of interest and be transparent for microwaves. The number of defects can be kept small and often below the detection limit in Suprasil windows. The transparency criterion for microwaves is not met by Suprasil at W-band frequencies. The absorption coefficient α is 3.69 m^{-1} for fused quartz at 94 GHz [122]. To evaluate the absorption losses the Lambert-Beer law ($I = I_0 exp^{-\alpha x}$) is applied. Its derivation is based on the condition that the wavelength is small compared to the thickness of the material penetrated. This is not the case for the quartz window and the microwaves used ($\lambda_{mw} \approx 3.2$ mm), but an estimation of the losses involved is possible. For a single transmission the intensity decreases to 99.94 % taking the thickness x as 150 μm. Doubling the thickness lowers the value to 99.89 %. Although both values are close to unity one has to keep in mind that a

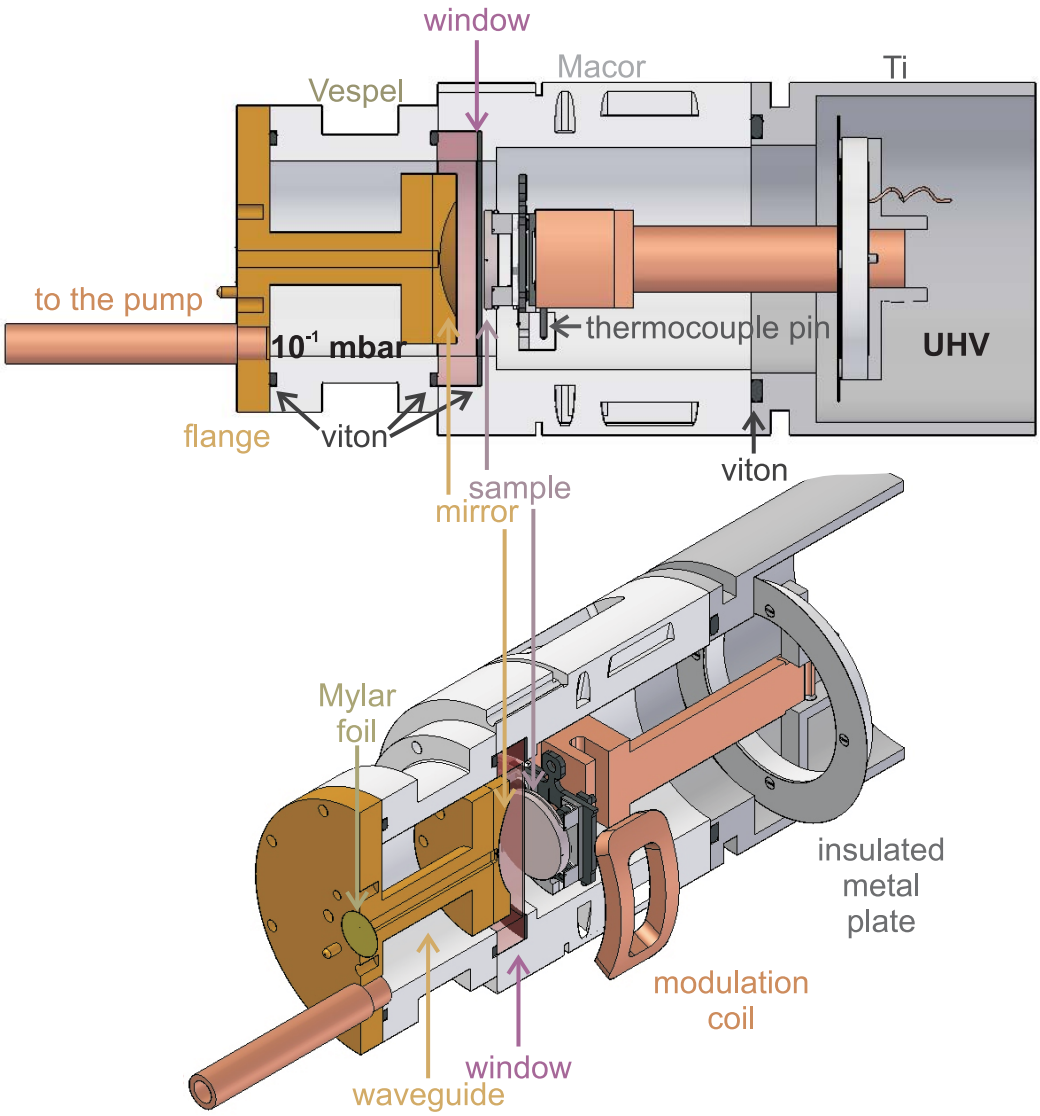

Figure 4.3: Schematic drawing of the resonator connection to UHV.

resonator is used to allow multiple reflections between the two mirrors. After 500 transmissions the intensity for the 150 μm window is still close to 75 % whereas for 300 μm the intensity drops below 60 %. Besides the absorption properties of the window its mechanical stability is very important. The window has a diameter of 30 mm. The force that acts on the window is determined by the window area and the pressure difference on both sites. Assuming UHV on one side and ambient conditions on the opposing one, the glass has to withstand about 70 N which is far beyond the stability of submillimeter thick windows. Under these conditions a window of either thickness would certainly break. For this reason the concave mirror is not kept at ambient conditions but sits within a fine vacuum compartment. The pressure difference can be kept below 0.1 mbar which reduces the applied force by four orders of magnitude. Under these conditions even a window thinner than 150 μm could withstand the force, but the absolute pressure differences would have to be kept small while pumping and venting the resonator which is not feasible for the combined UHV-fine vacuum system. Choosing a window with a thickness of 150 μm allows the absorption losses to remain low while guaranteeing mechanical stability for pressure differences of a few mbar. A detailed description of the evacuation of the resonator while maintaining small pressure differences is given in section 4.2.1.

The sealing of the window and resonator housing against ambient conditions is depicted in Fig. 4.3. The choice of housing material is largely governed by the necessity of field modulation for the lock-in detection of a cw-EPR experiment. For this reason the housing has to be mainly metal free in the direction of the modulation field. The current implementation only allows measurements with the modulation and thereby the main magnetic field parallel to the sample surface. The design described in the following satisfies the conditions that are set by the modulation coils for this field orientation. Measures that have to be taken to adjust the setup for perpendicular orientation of the static magnetic field with respect to the sample surface are discussed in section 4.2.3.

On the UHV side the housing is made of Macor which is flanged onto the titanium tube of the transfer chamber. The titanium flange has a groove and sealing is achieved by a viton O-ring (37×2.5 mm^2). To attach the Suprasil window the thin window is melted onto a ticker quartz ring (o.d. 39 mm, i.d. 30×6.0 mm^2) made by the manufacturer Hellma. For the area of the window in the center out to a diameter of 20 mm a tickness of 150 μm is guaranteed, but past this point it is less well-defined due to the melting process. The Macor body has a recess built that the window rests on. A flat viton gasket (o.d. 39 mm, i.d. 32×1.5 mm^2) is put between Macor and window. The housing of the fine vacuum compartment is made of Vespel. This material bears the mechanical stress caused by tightening the screws better than Macor and is suitable for the use in fine vacuum. The Vespel body has grooves on both ends and viton O-rings (35×1.5 mm^2) are used for sealing. To close the fine vacuum a flange made of brass is used. The flange has a feedthrough for the pumping line and a W-band waveguide soldered through its center. A 6 μm thick Mylar foil is pressed

between the outer flange and the adjacent W-band waveguide piece housing the coupler to seal the fine vacuum compartment. The coupler is connected through a taper from W- to K_a-band and via a long K_a-band waveguide to the microwave bridge. The K_A-band waveguide is used as it reduces transmission losses due to its larger dimensions. The Mylar foil easily withstands the pressure difference between fine vacuum and ambient pressure as the resulting force is small due to the size of the waveguide cross section (1.27×2.54 mm^2). The pumping line leaving the brass flange runs through the horizontal magnet bore before it joins a prevacuum system shared with the transfer chamber. The pressure behind the magnet bore is about 10^{-3} mbar. A determination of the pressure closer to or inside the resonator is not possible due to the space limitations.

The space inside the resonator is strongly reduced compared to the inner diameter of the titanium tube (50 mm, see section 3.3.2). This has various reasons. The thickness of the housing material itself is chosen such that it can bear the mechanical stress. The Macor, for example, needs more material to support tapped holes than the Vespel. Additionally the housing thickness is increased as the window frame has to be clamped between Macor and Vespel sections, connecting the two housing parts. To allow sealing between the Macor housing and the titanium tube the inner diameter of the latter narrows to leave space for screws. Besides the space limitations arising from the housing and its connections the need for modulation coils close to the sample has to be taken into account. A Helmholtz pair is used to induce the alternating magnetic field B_{mod} at the sample parallel to the surface. One coil and its position are indicated in Fig. 4.3. The Helmholtz pair is glued into cutouts on the outer shell of the Macor piece. To place the Helmholtz pair inside the resonator housing and thus closer to the sample is not possible as it would interfere with the window. The distance between window and sample is generally ≤ 1 mm (see also section 4.3.2). The advantage of having the modulation coils at ambient conditions is that no additional feedthroughs into vacuum are necessary. The disadvantage of this arrangement is the greater separation of the coils which allows a maximum B_{mod} of 5 G. Above this value microphonic effects significantly spoil the signal-to-noise ratio. The inner diameter that remains at the sample site taking these points into consideration is 34 mm. Due to the recess for the window the Macor ultimately narrows down to 30 mm, but this does not pose any further constraints as only the single crystal with the diameter of 12 mm enters this area. On fine vacuum side the inner diameter is 30 mm due to the sealing.

A proper alignment of the two mirrors with respect to each other is important to minimize losses. Three different kinds of misalignment are possible: the separation between the two mirrors does not fulfill the resonance condition, the mirrors are laterally displaced, or the mirrors are tilted with respect to each other. In the following the evolutionary development of dealing with alignment issues is discussed before the sample setup on the EPR cryostat is described in its final version.

The position of the concave mirror is fixed. Its housing orients the mirror

perpendicular to the main axis of the titanium tube. A lateral displacement of the two mirrors can be achieved by moving the sample mounted on the manipulator with its x, y-stage. The starting point for x, y-adjustment is given by the position determined for entering the titanium tube as explained in section 3.3.2. The precision of the manipulator is sufficiently high for lateral adjustment, however it only functions correctly if the cryostat or manipulator tube do not touch the walls. As pointed out previously, the alignment of the different tubes (cryostat, manipulator, titanium tube, magnet bore) is very important to avoid collisions but also to allow good mirror-sample alignment. If a displacement in the x, y-plane leads to wall contact the setup bends, resulting in a lateral displacement as well as the sample tilting.

The first sample setup on the cryostat was designed to allow for exact placing of the sample in resonance position and the ability to compensate for a tilt between the two mirrors. It is shown in Fig. 4.4. The core piece is a piezo stack consisting of three components: Two goniometers and a z-piezo (ANGt100, ANGp100, and ANPz100, attocube systems, Fig. 4.4). All three piezo devices are stick-slip motors. If unmoved they have zero potential and thus do not interact with the stray fields of the superconducting magnet in their idle positions. Furthermore, they have a comparably large range with high resolution. With a traveling distance of 5 mm and nanometer precision the z-piezo can reach different modes within the resonator. The goniometers allow the single crystal to be tilted by 6.6° about the x-axis and 5.4° about the y-axis. The two piezos are combined to have one common center of rotation. This center determined the sample position in the early setup. The ideal angles were found by adjusting the goniometers to obtain the maximum signal response. The drawback of this mechanism is the fragility of the piezos. While the sample is transferred between the EPR cryostat and the transfer rod of the preparation chamber or the wobble stick of the STM, uncontrolled forces are applied. During this procedure all three piezos have to be protected. As seen in Fig. 4.4 the piezo stack is enclosed by a cage made of titanium. On the side facing the sample the cage is partially closed with a pin extending from the roof-plate. The piezo stack with the mounted sample holder share a locking plate as a counterpart to the pin. During sample transfer the piezos have to be adjusted such that the locking plate tightly embraces the locking pin and the cage takes the force. To find the locking position a laser was directed onto the locking plate through a CF16 viewport at an angle of 30°to the titanium tube. The reflection left the chamber by a second viewport on the opposite site of the titanium tube. The laser spot was then used as a guide to drive the piezos into their original position and lock them for sample transfer. Practically, this procedure did not work with sufficient reproducibility. For this reason the piezos were removed. Besides the difficulties with mechanical stability of the piezo stack, the piezos themselves could not be used as heat conductors for cooling of the sample. Additional conducting wires connecting the cryostat and sample plate had to be implemented within the limited space. The removal of the piezos enhanced the stability of the sample setup and simplified the cooling

of the sample.

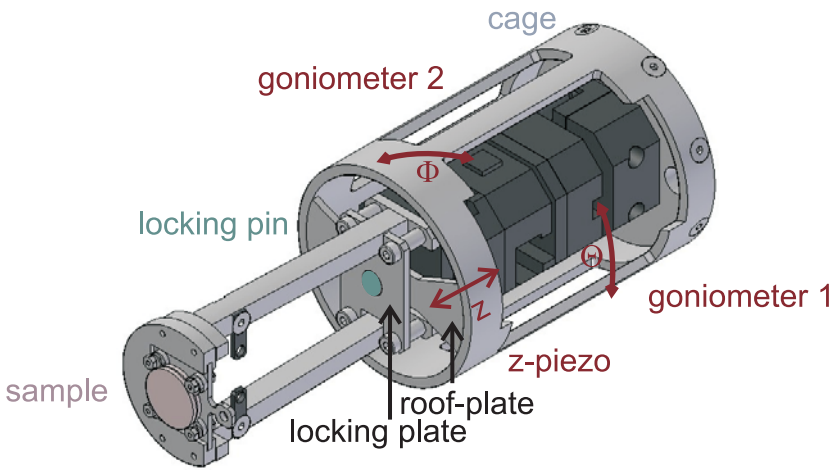

Figure 4.4: Schematic drawing of the original EPR cryostat mount with 3 piezos and a locking mechanism for transfer.

The modified sample setup on the EPR cryostat is shown in Fig. 4.5. The sample plate is inserted in a molybdenum sample holder with a diameter of 28 mm. This diameter leaves the necessary clearance for a sufficiently high pumping cross section and just allows all parts to fit. The sample is clamped down with springs made of molybdenum. The copper base has a cutout for the anti-rotation rods of the transfer drive. The holder possesses a receiving part for the thermocouple made of Macor as described for the preparation manipulator (section 3.4.1). Due to space limitations the wide bores where the thermocouple pins enter are only 3.5 mm deep thus leading to shorter thermocouple coils which reduces the contact length. The thermocouple connection is shown in Fig. 4.3. The length of the copper extension shown in Fig. 4.5 was determined by the evolutionary development starting from a piezo stack as described above. The copper block is screwed directly onto the cryostat. To avoid sticking of the copper block to the gold plated copper cryostat a thin molybdenum foil is inserted between both. Furthermore, the insulated metal plate used to ensure a proper alignment of the setup in the titanium tube as described in section 3.3.2 is shown.

Due to the fact that the position of the planar mirror is now fixed on the manipulator, alignment must be achieved in a different manner. It proved sufficient to equip the manipulator with a reduction gear to correctly position the sample along the z-axis. More effort was needed to keep the tilting angle between the two mirrors small. As mentioned before the orientation of the concave mirror with respect to the titanium tube is well-defined. As their is no visual access to the two mirrors in the measuring position an ex-situ alignment of the sample and titanium tube suggests itself. To determine and eliminate the tilting of the sample not the tube itself but the flange connection on the UHV chamber is used. A plain sample plate was mounted on the EPR cryostat. The tilting angle of

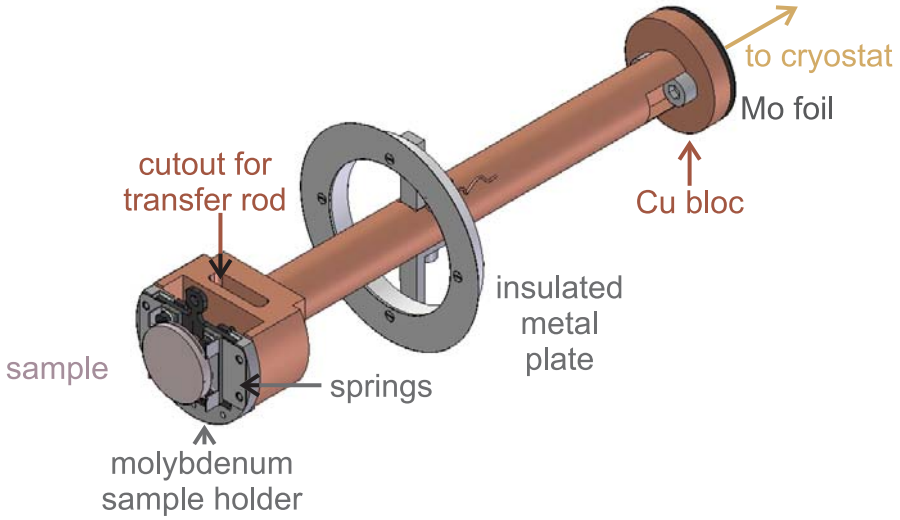

Figure 4.5: Schematic drawing of the setup of the EPR cryostat.

the plate was measured on the crossing of stainless steel chamber and titanium tube in comparison to the blind flanged chamber. The deviation was determined by the reflection of a laser beam from the surface. The formerly parallel planes of the copper block in Fig. 4.5 were then adjusted to reduce the tilting of the sample plate sufficiently with respect to the transfer chamber flange. To make this procedure work it is important that the single crystal surface and the sample plate are well aligned to each other (compare section 3.4). The disadvantage of this procedure is that no in-situ readjustment is possible. Even if the system is well aligned initially the mechanical stress induced by cooling/annealing as well as sample transfer can lead to displacement of the cryostat in the manipulator tube. This cannot be totally avoided and when this occurs the system has to be realigned after breaking the vacuum before experiments can continue.

4.2.1 Evacuation of the Resonator

As mentioned earlier, the thin quartz window can only bear small pressure differences. Therefore special care needs to be taken while pumping down from ambient pressures and venting. To ensure similar pressures in the fine vacuum compartment and the UHV chamber both systems have to be connected and evacuated with the same pump. Equivalently one valve should be used to vent the combined system. Furthermore, the pumping and venting speed have to be limited. Due to space limitations the pumping cross sections on the fine vacuum side are small. In the fine vacuum compartment the hole in the concave mirror especially limits the pumping speed as previously mentioned in section 4.2. Additionally, the pumping line through the magnet with an inner diameter of 4 mm

is narrow in comparison to all other cross sections involved (14 mm or larger). The problem with small cross sections is that the laminar flow stops at higher pressures. Instead the molecules behave as described by Knudsen flow which leads to a slower pressure equilibration in the system. To keep the stress on the quartz window small the pumping speed is limited to 1 mbar/s below 100 mbar.

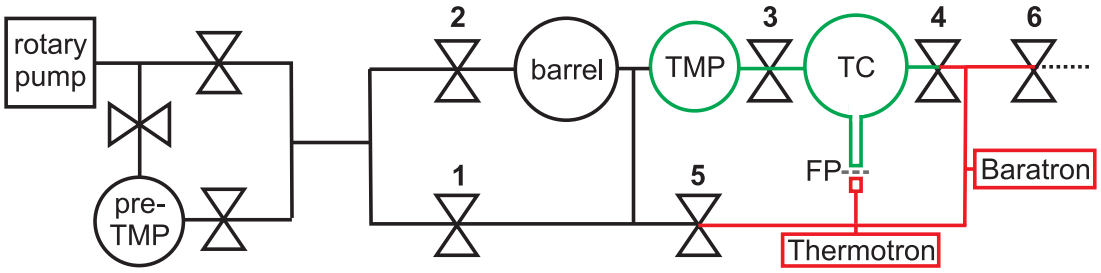

Figure 4.6: Shown is the part of the pumping system that is involved in pumping down and venting of the resonator; FP is the Fabry-Perot resonator with the dashed line indicating the separation induced by the quartz window; shown in red is the fine vacuum part of the resonator, in green the UHV part.

With these preliminary considerations the evacuation and venting of the system was realized as shown in Fig. 4.6. The fine vacuum compartment of the resonator (red) can be connected to the transfer chamber (green) by opening the manual gate valve **4**. The prevacuum system is used to pump the system down. The combined fine vacuum-UHV system is initially connected to the prevacuum system by opening valve **1** and the pneumatically driven gate valve **3**. Valves **2**, **5**, and **6** are closed. Valve **1** and **2** are angle valves. While valve **2** is pneumatically driven, the other one is manually operated and can be used to set the appropriate pumping speed. As the maximum pumping cross section is low for valve **1** number **2** is opened at low pressures. Valve **1** is then closed, because only valve **2** is connected to the control unit of the whole pump system which was introduced in section 3.3.1. Pumping through the turbo molecular pump (gate valve **3** open) instead of using the direct access through valve **5** has proven important as the TMP acts as a reducing element which suppresses peaks in the pumping speed. The pressure decrease is initially monitored by a Baratron (MKS, Type 626, Range 1000 mbar). Once 1 mbar is reached the pressure is read by a Thermotron on the fine vacuum side. Below 10^{-1} mbar valve **2** and **5** are opened while **4** is closed. The two resonator halves are separated. The transfer chamber can now reach UHV conditions with the additional pumps and by baking it out whereas the fine vacuum system simply continuous to be pumped solely by the prevacuum system. The base pressure reached in the transfer chamber is $< 2 \times 10^{-10}$ mbar. This proves that the construction of the Fabry-Perot resonator satisfies the UHV requirements.

For venting valve **4** is opened to reconnect the resonator halves. The prevacuum system is then disconnected by closing valves **1** and **2**. Number **5** is closed

as well. Gas is led into the system via valve **6** (a needle valve) on fine vacuum side right beside the manual valve **4** of the transfer chamber.

4.2.2 Microwave Coupling

A variety of possibilities to couple microwaves into a resonator exist (e.g. [110]). During this thesis three different approaches were considered, while bearing in mind the specific characteristics of the resonator. In all cases the microwaves enter the resonator through a hole in the concave mirror. In principal the resonator can be tuned with the magnet removed, but the shift in weight leads to slight mechanical changes that alter the coupling under measurement conditions. The ideal coupling mechanism therefore allows the final coupling with the magnet in measuring position where direct access to the coupling site is not available. The approaches considered closely followed systems constructed for ambient conditions. The microwave coupling schemes will be compared to their ambient counterparts and each other in terms of practicability.

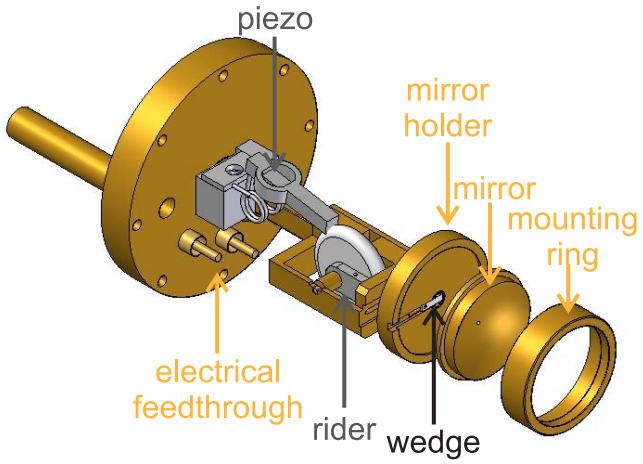

Figure 4.7: Realization 1: microwave coupling into the resonator by an iris.

The first realization is shown in Fig. 4.7 and the coupling mechanism is mostly inspired by Burghaus *et al.* [29]. The concave mirror made of copper has a round aperture as microwave inlet. This iris has diameters varying between 0.7 to 1 mm. The radius of curvature of the mirror is 15 mm and the diameter 19 mm. Those values were used in [29] for a symmetric Fabry-Perot resonator. The W-band waveguide is terminated by a $\lambda/4$ choke flange. The coupling is achieved by moving a ceramic wedge in a groove milled into the mirror holder. The mirror is tightly pressed onto the mirror holder by a mounting ring. The specific difficulties for the vacuum adaptation are related to the necessary movement of the ceramic wedge in fine vacuum. The wedge requires a movement perpendicular to the axis of the vacuum housing which cannot be accomplished by a colinear movement

outside the fine vacuum due to the limited space. Instead an elliptical piezo drives a wheel. By the rotation of the latter a rider sitting on the same axis as the wheel moves up and down. The wedge is pinned to the rider and thus is driven by the movement of the rider. The advantage of this setup is that the coupling can be adjusted independent of the position of the magnet. Adding an electrical feedthrough to the fine vacuum flange is all that is necessary for the coupling via the elliptical piezo motor. To improve coupling different iris diameters (0.7 to 1.1 mm) and wedges (e.g., Macor, teflon, silver plated Macor) were tried. Although the Q factors in a final stage reached about 3000, the biggest drawback of this setup was the reproducibility of the wedge position. Due to the translated motion and the small tolerance involved the wedge became stuck easily and instead of moving continuously, discontinuous jumps resulted. This made regular critical coupling impossible and excluded this coupling mechanism.

Instead, an alternative scheme was searched for that allowed continuous change of the coupling element. The setup implemented closely followed the scheme outlined in [88, 89]. The adaptation to the current system is shown in Fig. 4.8. The concave mirror is in this case directly pressed onto the blunt end of the W-band waveguide. The coupling hole in the mirror had the same dimensions as in the previous case. The coupling was achieved by introducing a dielectric slider in the W-band waveguide. The slider was on the resonator side rectangular and filled the hole space of the waveguide. Towards the microwave bridge it thinned wedge-shaped to a ridge.

This ridge ensures a continuous impedance increasing with increasing filling of the dielectric in the waveguide. In this manner reflection losses are avoided that do occur otherwise. The adjustment of the coupling is achieved by moving the slider along the waveguide. For this purpose two cuts along the longitudinal direction of the waveguide were made and two metal foils inserted. The foil was fastened to a holder that could move parallel to the waveguide and thus drag the foil pieces and the wedge forward and backward. The holder itself was moved by rotation of the center rod. This rod ran through the stabilizer. Due to the use of snap rings at the entrance and exit of the stabilizer the center rod could be rotated without displacement. The center rod ran through the holder and both rod and holder were threaded at that point so that rotation of the center rod drove the holder. To avoid tilting, two guiding rods ran between stabilizer and the mirror back plate. The results obtained with this coupling scheme were discouraging. The intensity was too low to start working with. This was not significantly improved by introducing a metal ball (diameter about 0.1 mm) on the resonator side of the slider as done by Kümmerer *et al.* [88]. One likely reason is the differences in TEM_{00n} modes used. While Kümmerer *et al.* use the TEM_{003} and the TEM_{004} modes [89] this is not possible in the present setup with the Suprasil window (see section 4.3). Larger separations were not used in [88, 89] as they were more difficult to couple. Kümmerer *et al.* also pointed out that their intensities are low but still sufficient for non-lossy samples. As in the present case high sensitivity is of utmost importance no further work on this coupling scheme

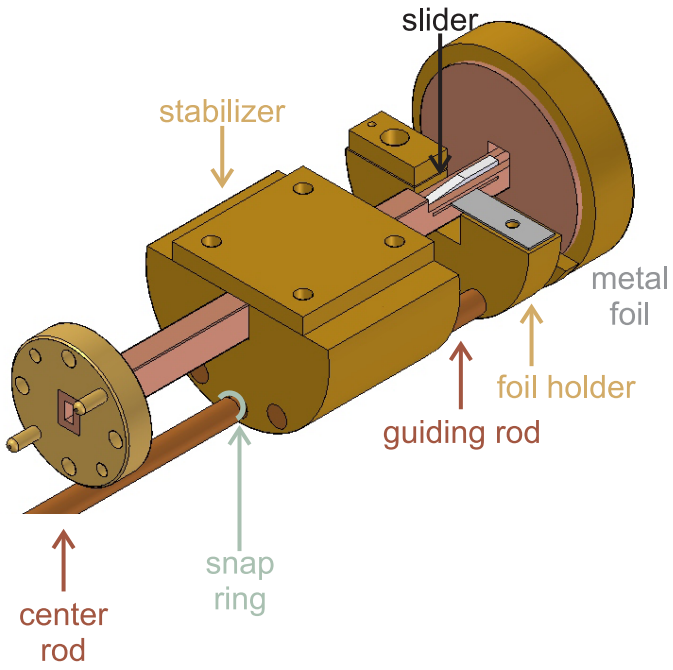

Figure 4.8: Realization 2: microwave coupling into the resonator with a wedge in the waveguide.

was done and a third alternative was implemented.

The transition from waveguide to resonator sits within fine vacuum in a small compartment. In order to use a coupling element in this compartment mechanical adjustment has to take place in vacuum. As precise positioning of the coupling element has to be achieved, direct access at ambient pressure is preferable. This lead to the implementation shown in Fig. 4.9. A combination of an antenna in vacuum and a phase shifter at ambient is used. The setup is based on a design for a Fabry-Perot resonator at 48 GHz [65] and adapted to W-band dimensions and the experimental conditions given. The microwaves enter the resonator through a 0.9×0.2 mm^2 rectangular slit in the center of the brass mirror. Behind the hole typical W-band waveguide dimensions (1.27×2.54 mm^2) are cut into the mirror material. The long edge of the slit is perpendicular to the broad dimension of the waveguide. The microwaves are coupled into the resonator using a dipole antenna made of 0.06 mm Kapton insulated copper wire. It forms a loop whose dimensions are about 1×0.8 mm^2. The Kapton not only prevents unwanted contact with the mirror but also increases the stability of the thin wire. The ends of the wire are pressed between the backside of the mirror and the flange of the adjacent W-band waveguide as seen in Fig. 4.9. The distance between the slit in the mirror and the pressing point of the wire is chosen to maximize the field in the resonator. In order to do so the antenna ends have to be connected where the electric displacement currents are at maximum. This is the case for a

quarter of the waveguide wavelength λ_{wg} away from the slit under the condition that waveguide and resonator are matched. The displacement currents induce an electric dipole oscillation in the antenna. The head of the loop slightly enters the space in front of the mirror where it radiates a TEM mode with the magnetic field component perpendicular to the loop plane. Thus the magnetic field component has the same orientation as in the waveguide.

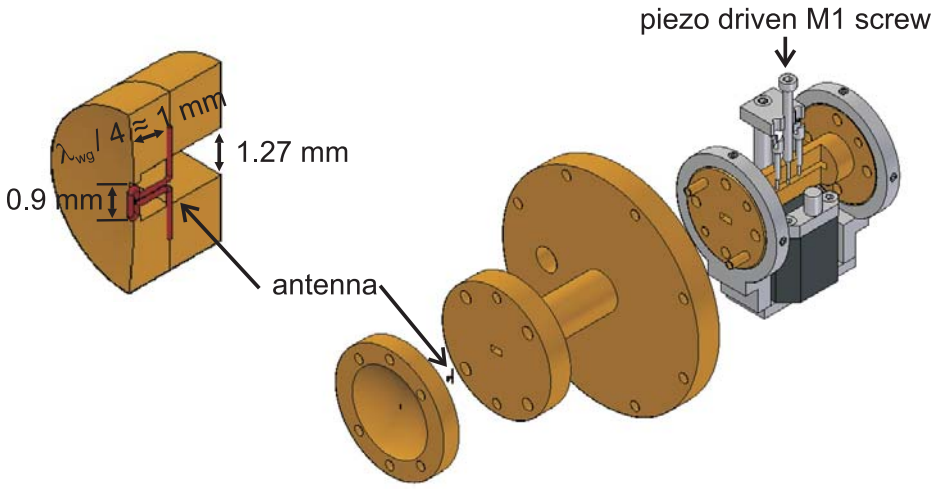

Figure 4.9: Realization 3: microwave coupling into the resonator using an antenna and a three-screw tuner.

Adjustment of the microwave phase is realized by a three-screw tuner. Different distances between the screws lined up along the longitudinal direction of the waveguide on the broad dimension are mentioned in literature ranging from $\frac{\lambda_{wg}}{8}$ to $\frac{\lambda_{wg}}{2}$ [39, 128]. Due to the small dimensions at W-band we chose a distance of $\frac{5 \cdot \lambda_{wg}}{8}$. M1 threads were directly drilled into the W-band waveguide. M1 brass screws were tapered down to diameters of 0.25 or 0.5 mm over the length that can at maximum enter the waveguide. The backlash of the threads hampers a precise coupling of the resonator. To reduce this effect viton was used to spring load the screws. The optimal dimensions for the stubs are determined experimentally. It was found that the optimal setting of screws depends upon the details of the antenna used, therefore the tuner setup is adjusted for every new antenna. In most cases the influence of one of the screws on the coupling was highest. The screws themselves are not accessible with the resonator being in the measuring position, instead an approximate coupling has to be done before the magnet is moved forward. To allow an adjustment with the magnet in position the screw with the highest influence was replaced by a stub that is held on a bridge above the waveguide and can be adjusted using a linear piezo (ANPz51, attocube systems, Fig. 4.9). One difference in the resonator housing between the case of coupling with an iris and the antenna is that the fine vacuum compartment is

smaller for the latter in order to keep the W-band waveguide short and place the phase adjustment as close as possible to the resonator.

4.2.3 Main Magnetic Field Perpendicular to the Sample

For completeness the steps that could be taken to modify this system to measure EPR with the static magnetic field oriented perpendicular to the single crystal surface will be outlined in this section. Preliminary tests were performed with coupling mechanism 1. As well as the main magnetic field the modulation field has to be applied perpendicular to the sample. This is only possible if the concave mirror is transparent for the modulation field, otherwise strong microphonic effects result – as the single crystal is made of solid metal and mounted on metal parts, metal can only be avoided on the concave mirror. For this purpose the mirror and mirror holder in Fig. 4.7 were manufactured from Macor and silver plated afterwards by precipitation and electrolysis. The W-band waveguide was glued into a slot cut into the mirror holder before the plating. The Q factors obtained with this setup were very satisfactory (up to 8000) but the coupling intensities were relatively low. This was most likely due to an insufficient plating of the waveguide-Macor transition or about the iris. At this point the realization of perpendicular measurements was postponed to a later stage. For the antenna coupling described above (Fig. 4.9) the plating of the single parts poses a smaller challenge as the antenna instead of the hole in the mirror transmits the field. It is certainly worth revisiting this in the future.

In order to rotate the magnet while maintaining vacuum conditions within the resonator the pumping line of the fine vacuum compartment can be sealed with a valve. Behind the valve the vacuum can be lifted and all connections running through the magnet removed allowing the magnet to be rotated. The modulation Helmholtz coils would have to be replaced by a solenoid to induce the desired modulation field. Feedthroughs and the pumping line could be reconnected and measurements perpendicular to the sample surface could then be performed. The estimated time of 15 min that it would take between closing the valve of the fine vacuum part and reconnecting the pumping line is sufficiently short to avoid cracking of the quartz window due to a pressure rise in the resonator.

4.2.4 Stabilization During Measurement

The resonator system as described above suffers from the individual mounting of the two mirrors. The brass mirror is fixed to the resonator housing and thereby to the titanium tube and the chamber. The sample under investigation in contrast is mounted on the cryostat which acts as long lever and easily picks up vibrations. As mentioned in section 3.3 the whole setup is mounted on an optical bench to reduce the mechanical noise and additionally rests on an active vibration isolation system which starts to damp vibrations above 1.2 Hz. Furthermore, local noise sources such as pumps can be switched off during measurement. A second

disadvantage of separated mirror mountings however remains: the different thermal coupling to the environment. While the cryostat and thereby the sample is inherently insulated from the surroundings as well as possible the titanium tube and thus the concave mirror is directly exposed to small temperature variations in the laboratory. Estimating the influence of a temperature change of 0.1 K on the position of the concave mirror by using the linear expansion coefficient of titanium (8.5 $\mu m/(m \cdot K)$ at room temperature) and a lever length of 50 cm leads to a displacement of 425 nm. Allowing a frequency shift of 2 MHz during the measurement which relates to a change in mirror separation of 60 nm the displacement reached by temperature effects is huge. This leads to small temperature gradients detuning the resonator. This happens within minutes which is not sufficient for the long scanning times of several hours that are often required in EPR experiments. A temperature stabilization of all parts involved to a precision <0.015 K is not feasible. Furthermore, the equilibration when cooling the cryostat with helium to the degree of stability reached at room temperature takes about 4 h. Thus, an active element for keeping the distance of the mirrors constant is necessary. The following requirements have to be fulfilled to reach stable conditions: the shift in distance has to be measured to a high degree and a device for compensating the mismatch with a feedback loop controlling the distance have to be implemented.

A cw-EPR spectrometer provides information on the distance displacement: the automatic frequency control (AFC) which has already been mentioned in section 2.1.8 tries to keep the microwave frequency on resonance. Its own range (about 2 MHz) is too small to compensate large drifts, but the control signal of the AFC can be used as it is proportional to the displacement along the resonator axis. Reading this signal and adjusting the position accordingly is therefore possible. However, there are cases where the AFC will not work: At low intensity of the mode, e.g., due to high attenuation of the microwave for lossy samples or if pulsed measurements are conducted in the future. In the latter case an alternating current AFC as implemented here cannot be used as it relies on a modulation of the microwave frequency. Especially in the initial experiments with resonator 1 the intensity of the mode was low and AFC-locking not possible.

With the current coupling mechanism and microwave attenuations of up to 25 dB the automatic frequency control can be used. The AFC voltage supplied by the X-band bridge is constantly read out and fed into a feedback loop (using a self-made Labview program). Originally the z-piezo was used to put the sample back into the proper position. The finite step size of the stick-slip motor led to jumps in the EPR signal. To avoid the detection of the z-piezo steps in the EPR spectrum the measurement had to be interrupted, the position corrected, and after a delay time the scanning could continue. The use of a continuous driven piezo was prevented amongst other things by the interplay of travel distance and mechanical stability (see section 4.2). An alternative that allows continuous scanning is the exploitation of the temperature induced effects that are the source of the problem in the first place. An adjustment of the relative position of the

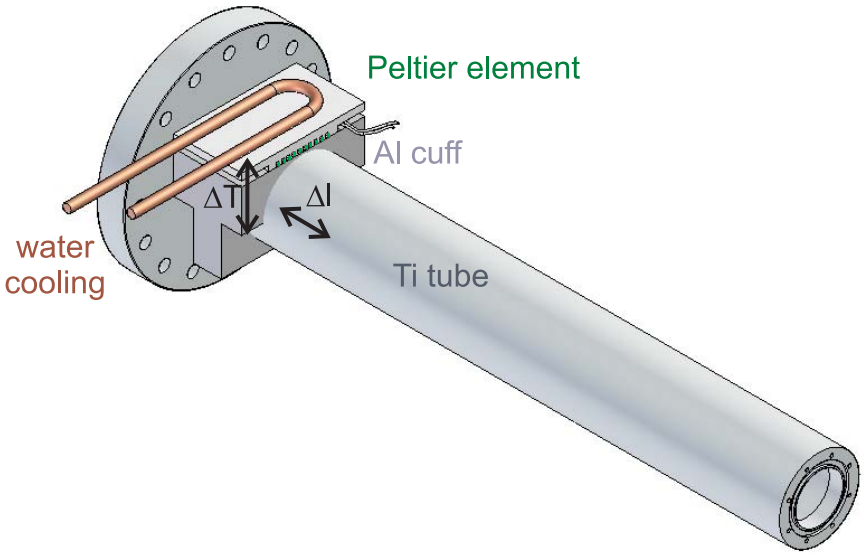

Figure 4.10: Inducing distance changes by the use of a Peltier element.

sample and concave mirror can be achieved by changing the length of the titanium tube which results in the resonator housing and the concave mirror shifting as well. For this purpose a Peltier element was mounted on an aluminum cuff which embraces the titanium tube (Fig. 4.10). On top of the Peltier element a water cooled copper plate is attached. The necessary distance adjustment is done by cooling and heating the tube accordingly. A careful choice of the PID parameters for the response of the Peltier element to the offset read by the AFC now allows sample repositioning during measurement and stability on the time scale of hours is achieved. The latter is non-trivial for cooled samples as particular care has to be taken to stabilize the temperature and the helium flux through the cryostat.

4.3 Influence of the Window

So far the Suprasil window was introduced as a seal between UHV and fine vacuum in the EPR resonator but nothing has been said about its possible influence onto the resonator properties. As mentioned before the thickness was chosen to avoid absorption losses. Beyond that a material was introduced into the resonator with a refractive index different from vacuum. In this section optical effects and geometrical adjustments due to the presence of the window are discussed. As the radical DPPH (2,2´-diphenyl-1-picrylhydrazil) was used in almost all measurements to test the performance of the EPR system its properties regarding EPR will be introduced before turning to the window itself.

4.3.1 DPPH

The molecular structure of DPPH is shown in Fig. 4.11. In dilute solution a quintet of lines is observed due to the interaction of the single electron with the two approximately equivalent ^{14}N nuclei [87, 162]. In the solid state – either crystalline or powder – a single Lorentzian-like line appears due to exchange narrowing that dominates over the also present dipolar broadening. The g-value for DPPH crystallized from a variety of solvents is given as 2.0036 ± 0.0002 [162]. The linewidth of the solid state X-band spectrum is strongly dependent on the solvent the DPPH solid was prepared from and ranges from 1.5 to 8.1 G [162]. This effect is explained by assuming different distances between DPPH molecules caused by the number, shape and size of remaining solvent molecules. Studies at higher magnetic fields and frequencies (220 GHz, 460 GHz) suggest that the spectra of powder samples display a residual g-anisotropy leading to an increase in linewidth with frequency [82, 87]. In the present case the linewidth should be constant for a given preparation to allow a convenient comparison between measurements with different parameters. This can easily be tested by using the same parameters in the beginning and the end of an experimental series.

In all experiments conducted with DPPH the powder purchased from Sigma-Aldrich (D9312) was used without further purification. The DPPH was dissolved in toluene and the solution was then deposited onto an aluminum disc that was mounted onto the sample plate as shown in setup **I** without connections for temperature reading, biasing, and annealing (section 3.4). The solvent was allowed to dry in air before a measurement was performed. After approximately one hour of drying the DPPH sample remains unchanged in the EPR-spectrum for weeks. Degradation of the deposited powder could not be detected on the time-scales of the experimental series. This is in agreement with measurements by Yordanov who found high radical concentrations in samples as old as 30 years [162] but contrary to observations of other groups [147, 153]. The discrepancy is most likely due to the different impurities involved. These can explain the different decay rates observed for DPPH dissolved in toluene. Slangen *et al.* found DPPH decay rates with a life time of one day for powder dissolved in toluene at ambient conditions [125] whereas our solution kept in the deep freezer (-20 °C) did not exhibit significant degradation after months.

A typical DPPH spectrum obtained on the aluminum disc is shown in Fig. 4.11 on the right. The following experimental settings used were: modulation amplitude (MA): 3 G, receiver gain (RG): 24 dB, time constant (tc): 20.48 ms, conversion time (CT): 40.96 ms, microwave attenuation (MW att.): 20 dB, single scan. The Lorentzian-like singlet is centered at $g = 2.0032$ and the linewidth is 3.1 G. A reduction of the modulation amplitude led only to minute changes in the observed linewidth. The values obtained are in good agreement with the literature value of $g = 2.0036$ and a linewidth of 2.6 G in toluene at X-band frequencies [162]. However, other preparations led to larger linewidths up to 4 G indicating the dependence on the remaining solvent molecules. The amount of DPPH deposited

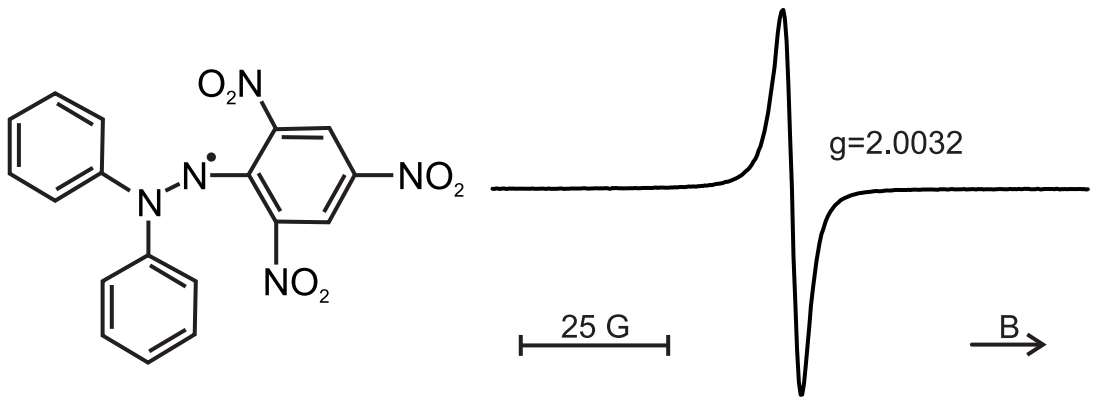

Figure 4.11: Molecular structure of DPPH and a typical EPR spectrum measured.

corresponds to 1.15×10^{15} spins assuming 100% activity. This is an overestimation of the true number of spins as the commercially available material contains only between 85 and 90% radicals [162]. The DPPH was mainly placed in the sample center. This leads to an enhanced signal in comparison to spreading the radical homogeneously on the aluminum due to the field distribution on the sample surface (which was shown in Fig. 4.2).

As the EPR spectrometer was set up with the intention of measuring species that are evenly distributed on oxide films a comparable spread is needed to estimate the sensitivity of the Fabry-Perot resonator in the setup. To get closer to a homogeneous distribution DPPH samples were prepared by spin coating using 2000-2500 rpm during the drying process. These samples looked macroscopically homogeneous but no on site measurement was possible to determine the distribution. Additionally, the amount of sample lost during the spinning procedure is unknown. For these reasons DPPH is not suitable for quantitative measurements in the present case which differs from conventional EPR investigations ([125,162] and papers therein). As DPPH was also applied at ambient conditions and not in UHV a different procedure was used to determine the sensitivity of the resonator. Direct adsorption of a paramagnetic molecule from the background in UHV gives a better estimate of the number of paramagnetic centers needed for detection. This is covered in section 5.4.

4.3.2 Position of the Window

From a technical point of view two different positions of the window in the resonator are simple to achieve. By flipping of the window frame in the resonator housing the glass pane is either close to the concave mirror or the sample assuming fixed positions of the mirrors. The two possibilities are schematically shown in Fig. 4.12 a) and b). In position a) the edge of the concave mirror is very close to the window and the mirror center is about 2.5 mm further away for a radius of curvature of 17 mm which was the radius initially used for antenna coupling.

In arrangement b) the sample-window distance is about 1 mm. Much smaller distances are avoided as their is no visual access while placing the sample.

Using a concave mirror with a $R_0 = 17$ mm it proved experimentally disastrous to place the pane close to the concave surface. In position b) the Q value is only slightly smaller compared to the window free case. The intensity of the mode decreases significantly, but the mode is still easily recognized. In position a), however, the mode intensity decreases to almost zero. In the following this experimental observation will be qualitatively discussed based on the optical effects occurring on the glass-vacuum interfaces.

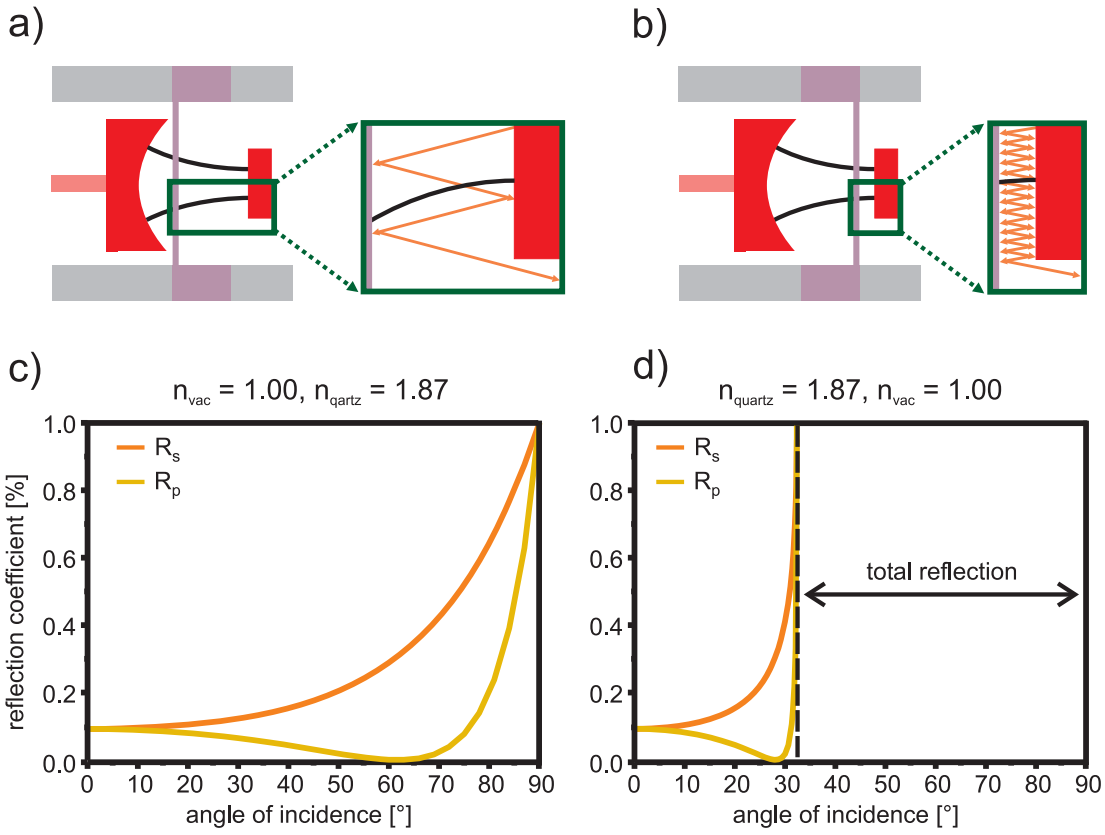

Figure 4.12: Influence of the window position: a) window close to the concave mirror, b) window close to the planar mirror, insets of a) and b): reflections between window and planar mirror, c) reflection coefficient at crossing the vacuum → window interface, d) reflection coefficient at crossing the window → vacuum interface.

In Fig. 4.12 c) and d) the reflection coefficients for *s*- and *p*-polarized light in dependence of the incident angle are shown for the vacuum → glass and the glass → vacuum interfaces. The graphs were obtained by using the Fresnel equations and the two different refraction indices n_x indicated [67]. Absorption losses are neglected for the moment by assuming that reflection and transmittance add up to 1. As the refraction index of Suprasil is not tabulated for 94 GHz the value for a related fused quartz (Herasil) was used [122]. The black curves in Fig. 4.12 a)

and b) indicate the Gaussian beam waists introduced in section 4.1. From those it follows that most of the radiation is only slightly inclined to the resonator axis. For angles smaller than 20° at the vacuum → glass interface and smaller than 10° at the glass → vacuum interface the reflection coefficients are close to 10 %. Due to the small angle distribution involved in case a) and b) a difference in reflection coefficiencts caused by different angles of incidence is not expected.

However, the diffraction losses caused by a reflection coefficient of 10 % are not identical for the two situations. This is schematically shown in the insets of Fig. 4.12 a) and b). By comparing the shape of the Gaussian beam waist at the vacuum → glass interface in case a) and b) higher average incident angles are observed for position a). Additionally, the distance between window and planar mirror is larger in a) than b). The combination of these two effects leads to the fact that the number of repeated reflections necessary for the radiation to escape the resonator is much smaller in a) than in b). The insets only depict the reflection occurring on the vacuum → glass interface. As a very similar reflection pattern also occurs at the neighbouring glass → vacuum interface the total amount of reflected light for one single transmission is almost twice as high as for the vacuum → glass interface alone which almost doubles the expected losses due to reflection. The behavior of the left half (concave mirror to window) and the right half (window to planar mirror) can be compared to the situation of a semi-symmetrical and a plane-parallel resonator. In section 4.1 it was already mentioned that the latter has higher diffraction losses [26]. Reflections bouncing back and forth between the concave mirror and the window are less critical due to the refocussing effect of the concave mirror.

Further aspects that contribute to a change of field distribution due to the presence of the window are absorption and polarization effects. Absorption losses due to the finite thickness of the glass pane were already mentioned in section 4.2. The differences expected for the two positions indicated are negligible. Higher angles of incidence also increase the distance traveled through the window, but the change in distance does not exceed 2 % and the effect is much smaller than the reflection effects expected.

In addition to the reflection problem in the resonator the window position influences the degree of polarization. For small angles the reflection coefficients for *s*- and *p*-polarized light are nearly identical but they substantially differ for medium angles as seen in Fig. 4.12. Higher angles of incidence which are more prominent for window position a) than b) lead to unequal reflection of the *s*- and *p*-polarized parts thus changing the ratio of the two. This in turn changes the orientation of polarization in the resonator and leads to two different effects: As discussed in section 4.1 the microwaves in the resonator are linear polarized. This polarization does not follow from the symmetry of the resonator but is due to the symmetry of the waveguide and the antenna used for coupling. If the direction of polarization changes in the Fabry-Perot resonator the antenna still only interacts with the magnetic field perpendicular and the electric field component parallel to its plane. Thus, the detected signal is reduced by rotation of the polarization.

The other effect occurring at changed polarization is a reduction of microwave absorption due to EPR transitions as these can only be induced by an oscillating B-field perpendicular to the static field. A decrease of this component by rotation of the polarization inevitably reduces the number of induced transitions.

These polarization effects could be demonstrated by rotating the W-band microwave bridge, the coupling scheme, and the connecting waveguides by 90° which aligns the microwave B-field with the external field. In the ideal case of linearly polarized light the microwave field cannot induce spin transitions in this geometry. However, as the orientation of the single components with respect to each other is not perfect some field component perpendicular to the external field remains and a small EPR signal is observed using a standard DPPH sample. Interestingly, the signal is stronger if the window is inserted in the resonator. For the common case of the microwaves being perpendicular to the external field the window always leads to reduction of the EPR signal. This indicates a rotation of the linear polarized light by the quartz window.

So far, the effect of window position was only discussed for the two geometries shown in Fig. 4.12 a) and b), but the absolute distance was not changed. As pointed out in section 4.1 a near semi-confocal arrangement is in most cases favored for semi-symmetric resonators. As mentioned above the initial radius of curvature was 17 mm for the setup with antenna coupling. This value is similar to those of other Fabry-Perot resonators used in W-band spectrometers [29, 151]. Determining the semi-confocal distance would lead to a mirror-mirror spacing of 8.5 mm ($R_0/2$). In Fig. 4.13 the beamwaists (w_0) at the planar surface are shown depending on the number of half wavelengths (n) within the resonator. The minimum beamwaists were calculated using eq. 4.7 and the necessary adjustment for the semi-symmetric resonator. The distance between the two mirrors is approximated by $d = n \cdot \lambda/2$ [151]. This deviates from the exact formula given in eq. 4.12. This approximation is justified by the fact that the contribution of the arc tangent term in eq. 4.12 is small compared to the distances involved and varies only slightly for neighboring fundamental modes. Using this approximation the TEM_{005} and TEM_{006} fundamental modes correspond to distances of 8 and 9.6 mm, respectively, taking λ as 3.2 mm. This is close to the semi-confocal arrangement, but sufficiently far to avoid mode degeneracy. The mode probed in Fig. 4.12 a) and b) corresponds to the TEM_{006} mode. This results from the window frame thickness of 6.15 mm, the depth due to the curvature of the mirror and a safe distance between pane and mirror. Experimentally the concave mirror can also be partially inserted into the window frame. This was achieved by using resonator housings of different lengths (Vespel part in Fig. 4.3). Insertion into the window frame allows the geometry to be changed in two possible ways: one can probe a smaller fundamental mode as the distance between the two mirrors decreases or rearrange the relative position of the glass pane to both mirrors by additionally adjusting the sample position with the help of the manipulator.

A decrease of the mirror-mirror distance to the TEM_{005} mode in the presence of the window showed a negative effect. Different from case a) measurements

were still possible, but in addition to a decrease in Q factor and mode intensity the signal amplitude was strongly reduced. This effect has to be attributed to the window. As seen in Fig. 4.13 the optimum beamwaist is slightly smaller for the TEM_{005} mode than the TEM_{006} mode, the resonator volume, however, increases due to the distance change from 5 to 6 half wavelengths and thus decreases the filling factor introduced in eq. 3.1. As the latter is directly proportional to the sensitivity a signal decrease for higher modes is expected regarding only this parameter. The changes in w_0 and the resonator volume are small between the TEM_{005} and the TEM_{006} mode and therefore suggest similar signal amplitudes for both modes in the absence of the window. To correlate the observed reduction in signal amplitude with the presence of the window the angles present in the Gaussian beam have to be discussed. The pane-mirror distance is very similar for both modes as ideally only the concave mirror was shifted. However, as the overall distance is shorter for the smaller mode on average, higher angles of incidence are present. This leads to higher diffraction losses as discussed above and explains the experimental result.

An even stronger reduction in EPR signal is observed if the resonator is kept in the TEM_{006} mode by retracting the sample simultaneously with the shift of the concave mirror. The increase in distance between sample and pane leads to a strong decrease of the mode intensity and Q. By shifting the pane closer to the middle of the two mirrors an intermediate case between Fig. 4.12 a) and b) is created that also leads to an intermediate result in EPR sensitivity. This observation suggests that a continuous increase of the glass pane-sample distance leads to concomitant decrease in EPR signal and is mainly attributed to a concurrent increase of diffraction losses.

Analysis of theses experimental facts led to the conclusion that the use of the TEM_{006} seems well suited to the current setup as neither a distance decrease between concave mirror and window nor an increase between window and sample had a positive effect. Going to higher mode numbers by retracting the concave mirror further has not been attempted using the window. Experiments without a window showed a decrease with increasing distance as would be expected in terms of the filling factor and for modes higher than the TEM_{007} the beamwaist as well.

Initially the idea existed that the absolute position of the window with respect to the electric and magnetic field maxima in the resonator was important. In an electric field maximum more absorption is expected than in a node. For this reason the distance between concave mirror and window was changed in steps of 200 μm inserting spacers between the Vespel-flange connection (Fig. 4.3) covering one half mode in total. The position of the planar mirror could then simply be adjusted with the manipulator. Although there was some variation in signal amplitude this effect is negligible in comparison with the relative position of the window to the mirrors. This experimental result indicates that the amount of absorption losses is small in comparison to the amount induced by the optical and geometric effects of this particular Fabry-Perot resonator. For this reason no

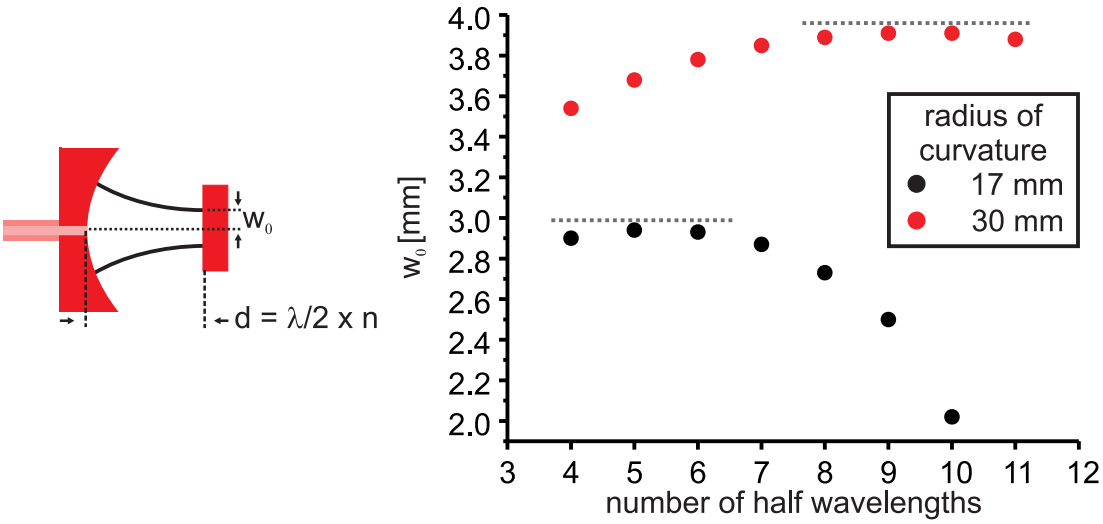

Figure 4.13: Minimum beam waist ω_0 according to eq. 4.7 and the necessary adjustment for the semi-symmetric resonator calculated for two mirrors of different curvature R_0, the dotted line is visual guidance to find the maximum beamwaist.

further effort was made to place the window in an electric node.

In conclusion, the window position in the resonator is crucial for the characteristics of the Fabry-Perot resonator. Experimentally is was shown that the microwaves should have near normal incidence to avoid destruction of the mode pattern. Qualitatively this is understood by the diffraction losses that vary with the distance between the planar mirror and the window. Additional effects such as absorption, polarization and window position with respect to the electric field distribution certainly influence resonator properties but to a smaller extent than the diffraction losses.

4.3.3 Mirror Size

As mentioned earlier the radius of curvature of 17 mm was chosen on the basis of the existing literature, but also because it was well suited to the experimental conditions. The radius of 17 mm allows the window to be placed in a near semi-confocal arrangement which maximizes the beamwaist on the planar mirror. Additionally this beamwaist is still small compared to the sample diameter of 12 mm. Larger ratios of beamwaist to sample diameter lead to higher diffraction losses meaning that higher Q factors and thereby higher sensitivity are expected for a smaller beamwaist. In the following it is discussed why a deviation from those preliminary considerations can improve the sensitivity in the presence of the window for the kind of samples used.

An increase in the radius of curvature leads to optimum beamwaists for larger mirror-mirror spacings. This is seen for a radius of curvature of 30 mm in Fig. 4.13. The maximum radii of the beamwaists increase, but they are also

shifted to higher modes. Assuming a constant power in the resonator the local field density is lower for larger resonators. As many EPR experiments are performed on samples that are small compared to the beamwaists shown here, e.g., protein single crystals, a maximum magnetic field in the available sample volume is desired. In contrast to those samples the paramagnetic species investigated in this work are spread over the whole mirror surface and an increase in beamwaist can be an advantage. To reach the maximum beamwaist for $R_0 = 30$ mm the resonator distance and thereby the volume, has to be doubled. This leads to a strong decrease of the filling factor introduced in eq. 3.1. However, even for smaller modes the beamwaist is significantly higher than for $R_0 = 17$ mm. It is not trivial to decide a priori whether a larger beamwaist with reduced local density or a smaller beamwaist with higher field density leads to better sensitivities in the case of paramagnetic species spread over the whole sample. Additionally, the influence of the window can be expected to vary for different radii of curvature. As discussed in the previous section the incident angles on the glass pane are very important for the resulting sensitivity. These angles become smaller by increasing the radius of curvature. For these reasons mirrors with different radii of curvature were compared. Experiments were performed with and without window to separate the effects induced by the presence of the quartz. The comparison was conducted for the TEM_{006} mode. In measurements with the window the sample was no further than half a wavelength away from the glass pane.

In total four mirrors with radii 17, 20, 25, and 30 mm were compared by measuring the signal-to-noise ratio (S/N) of DPPH samples. Each mirror was equipped with its own antenna. The use of only one antenna and transfer of the same between the mirrors is problematic due to its fragility. The single mirrors were tested with several antennas to estimate the performance and avoid influences of the antenna onto the experimental results. The comparison is shown in Fig. 4.14. The DPPH was prepared on two aluminum discs of different diameter (12 and 15 mm). Mounting of a 15 mm single crystal in the sample setup discussed in section 3.4 is not possible due to the connections and insulations necessary. However, a disc of this size can be mounted on an otherwise empty Omicron sample plate. The bigger planar mirror was included in this comparison to learn about the importance of the sample positioning in the x, y-plane. In the case of a significant sensitivity difference in favor of the larger planar mirror a precise positioning of the smaller sample would be considered more important. The DPPH solution was dried by the spinning procedure introduced in section 4.3.1 with 2000 rpm for the 12 mm disc and 2500 rpm for the 15 mm disc. The initial amounts dropped onto the aluminum discs were scaled to the surface area of the planar mirrors (about 1×10^{16} spins/cm^2). The final spin concentrations are not known due to the losses induced by spinning. As the tendencies observed are quite different for the cases with and without window they are discussed separately. First the window free case is treated.

For the sample with a diameter of 12 mm the S/N ratio increases slightly going from 17 to 20 mm radius. For $R_0 = 25$ mm it drops to about 60 % of the maximum

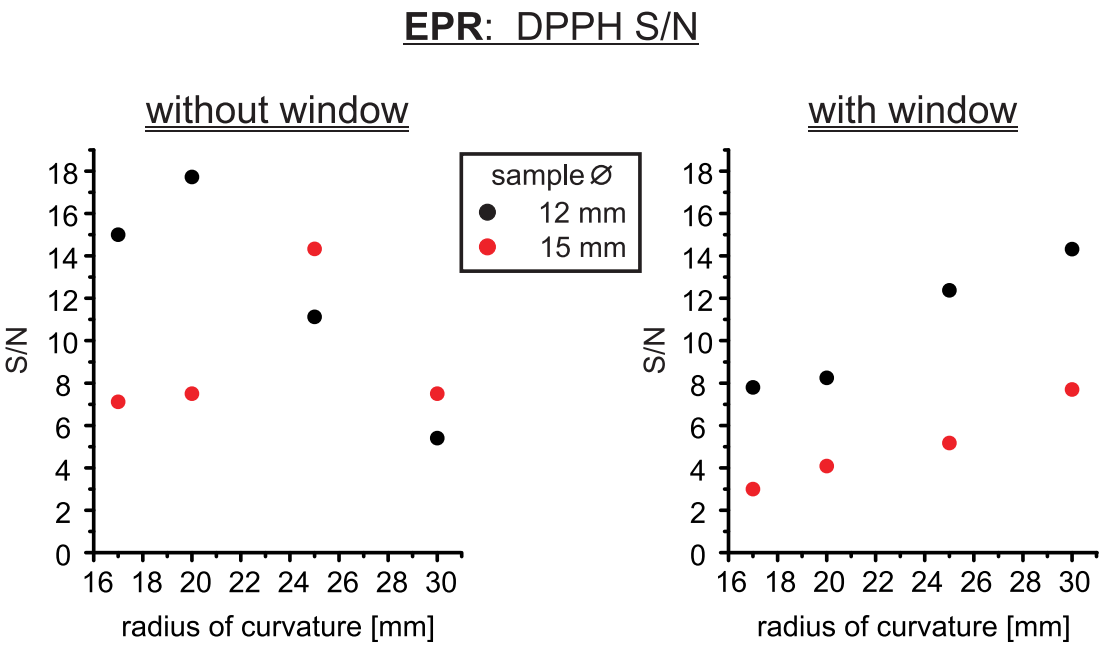

Figure 4.14: Shown is the signal-to-noise ratio for different mirror radii of curvature in the resonator with and without the quartz window; experimental settings: MA: 2 G, RG: 40 dB, tc: 5.12 ms, CT: 20.48 ms, MW att.: 20 dB, single scan.

value reached at the radius of 20 mm. For $R_0 = 30$ mm the S/N ratio decreases further to about 30 % of the maximum S/N ratio. For the sample diameter of 15 mm the S/N ratio is nearly identical for 17 and 20 mm. For $R_0 = 25$ mm the S/N ratio is almost doubled compared to the smaller curvatures. A further curvature increase to $R_0 = 30$ mm decreases the S/N ratio again to similar values as obtained for 17 and 20 mm. The maximum S/N ratio of the 15 mm disc with a value of ≈14 is lower than that of the 12 mm disc with ≈18. This is not only true for the S/N ratio shown in Fig. 4.14 but also for the absolute signal amplitudes (not shown): The higher signal intensity is observed for the smaller sample size. This is attributed to a reduced spin density on the 15 mm disc compared to the 12 mm disc due to the specific preparation technique used.

This complicates the aim to estimate the importance of positioning in the x, y-plane for the smaller sample size of 12 mm. However, the different behavior for increasing R_0 allows some conclusions to be made. For the 12 mm disc the best results are obtained for the radii of curvature of 17 and 20 mm. This is in accordance with the idea of a near semi-confocal setup which is almost reached for both curvatures. By increasing the radius further the beamwaist on the sample grows. Thus, the probed area is larger but the local magnetic field density reduced. Simultaneously, the diffraction losses increase due to the limited sample size. The decrease of the S/N ratio for larger R_0 indicates that the higher number of spins probed by the beamwaist cannot compensate the diffraction losses due to the sample size. This is different for the larger sample size of 15 mm.

Here, the maximum S/N ratio is observed for $R_0 = 25$ mm. The increase in beamwaist therefore also increases the number of EPR transitions although the local magnetic field density is smaller. Diffraction losses seem to play a minor role in this case. The decrease for $R_0 = 30$ mm is then explained by a changed influence of the three parameters beamwaist, field density, and diffraction losses. The latter two seem to outweigh the former one for this radius and sample size. The experiments demonstrate that in the window free case the positioning of the small sample in the x, y-plane is important. As the beamwaist drops exponentially a proper alignment about the resonator axis is necessary. Furthermore, the measurements show that the initial radius of curvature of 17 mm is very close to the best choice of R_0 for the window free resonator in the TEM_{006} mode.

The results obtained with the window in the resonator differ substantially from those without window. For the 12 mm as well as the 15 mm disc a steady increase in the S/N ratio with increasing radius of curvature is observed. Again the S/N ratio of the 15 mm disc is smaller than for the 12 mm one which is attributed to the spin density as above. In contrast to the case without window both sample sizes show the same behavior and suggest the use of a concave mirror with $R_0 = 30$ mm. The S/N ratio for the largest radius of curvature used reaches about 80% of the maximum ratio without window for the 12 mm disc and about 50% for the 15 mm disc. To understand the reasons behind these observations some additional experimental facts have to be known.

The Q factor for $R_0 = 17$ mm is about twice as high as for $R_0 = 30$ mm (about 3000 to 1500). The decrease in Q is accompanied by a reduction of the noise level. The decrease in noise is mainly responsible for the increase in S/N ratio when going to higher radii of curvature. The signal amplitude does not concomitantly increase, but is, for example, the same for the curvatures of 20 and 30 mm. The experimental observation that a lower Q factor for higher R_0 results in a reduction of the noise level should be explained. The experimental facts suggest that the noise figure measured at high Q factors is more sensitive to the mechanical instabilities of the resonator. Thus the decrease of Q for higher curvatures is accompanied by a decrease in the noise level.

Similar signal amplitudes for the radii of curvatures involved can be explained by the following considerations: The smaller curvatures have the advantage of a near semi-confocal arrangement and a higher Q. The advantage of the larger curvatures is a larger beamwaist and lower diffraction losses due to reflection. The latter is caused by the fact that the average angle of incidence is smaller for larger curvatures. For the radii of curvatures investigated the combination of the factors involved seem to balance leading to similar signal amplitudes in all cases. A different behavior for the two sample sizes used is not observed. If the position in the x, y-plane would significantly influence the signal amplitude this should be reflected in the S/N ratios and the signal amplitudes which is not the case. This is attributed to the fact that in the presence of the window the signal amplitudes observed result from the interplay of diffraction losses due to the window in dependence of the radius of curvature, the Q-factor, the beamwaist

and the probed sample area. The sample position is part of this interplay but is not dominating.

In conclusion, the best S/N ratio in the presence of the window is achieved by using a radius of curvature of 30 mm. This effect is mainly attributed to a decrease in noise level by a reduced Q factor. For the EPR measurements done in UHV a concave mirror with $R_0 = 30$ mm is used in this thesis.

Chapter 5

Experimental Results

5.1 MgO(100) on Mo(100) and Ag(100)

Magnesium oxide is an ionic oxide with insulating properties. It crystallizes in the rocksalt structure. Both experimentalists and theoreticians appreciate the simplicity of the structure as well as the highly ionic character that facilitate the analysis compared to more complex oxides. Thus, MgO plays a major role as a model system for heterogeneous catalysis, being used as bare oxide or as a support for metal particles [19, 37, 52, 53, 63, 70, 105, 161]. Furthermore, MgO has proved active as a solid-base catalyst, see, e.g., [7, 76] and lithium-doped MgO catalyzes methane conversion via a radical mechanism [75].

Besides the simplicity of MgO itself this oxide is chosen here because several projects on thin MgO films have already been completed in this institute [13, 15, 17, 83, 84, 94, 95, 124, 132–135, 139, 160]. Along with other methods the MgO film and its interaction with paramagnetic adatoms and adsorbates has also been characterized by X-band EPR spectroscopy [131, 137, 164] which allows extrapolation to W-band. The MgO film is therefore predestined to serve as a starting point for W-band measurements in UHV. All studies mentioned above employ silver or molybdenum as the metal substrate for the MgO film growth.

There exist several reasons to use either molybdenum or silver as a substrate. An important parameter influencing the epitaxial growth of a film onto a substrate is the lattice mismatch. It is defined as $m = (a_f - a_s)/a_s$, with a_f and a_s being the film and substrate lattice parameters, respectively. In the case of MgO and silver it is only $+2.9\%$ compared to -5.4% for MgO and molybdenum (the MgO lattice is rotated by 45°compared to the Mo substrate) [156]. The bigger lattice mismatch on molybdenum leads to stronger distortions in the growing MgO layers. The morphological changes have been investigated in detail for MgO films grown on molybdenum at room temperature after post-annealing them to about 1100 K [13, 14]. These studies show that a regular array of interfacial misfit dislocations forms to release the strain [13]. This results in tilting of MgO planes which is visualized by a complex spot structure in LEED. Observation of the simple 1×1 - structure expected for MgO indicates flattening of the surface

which happens with growing thickness. This is accompanied by the formation of screw dislocations to compensate remaining strain [13, 14]. Depending on the literature flattening of the films is described to occur between 7 and 15 ML, which is a wide range. However, the LEED pattern can be used to ensure that experiments are performed on rather flat films. The post-annealing step performed after preparation considerably increases the crystallinity of the film as reflected by a sharpening of the LEED spots.

In the thickness range between 2 ML and flattening of the film the crystallinity for an MgO film prepared on molybdenum at 300 K followed by annealing to 1100 K is similar to an MgO film prepared on silver at 200 K, but the average tilt angle is higher than for silver [14, 148]. MgO on silver grown between 300-350 K exhibits a mosaic structure at low coverages. The tilt angle decreases with growing thickness but due to the smaller lattice mismatch the effect is less pronounced than for molybdenum [156]. This introductory information would suggest to use silver in the case of thin films as they are flatter on this substrate whereas molybdenum has the advantage that the post-annealing can be used to increase the order of thick films and clean the surface.

In the case of silver single crystals one has to be aware of the fact that Ag(100) is not the thermodynamic stable surface (that is the Ag(111) surface). The silver single crystals used all developed opacity in some parts of the surface with time. That is, parts of the surface were mesoscopically rough. The influence of this roughness onto the film growth is not known. For STM measurements this is of minor importance as only flat surface areas are investigated, but for integrating methods such as EPR and IR uniform films are mandatory to draw conclusions.

A further issue to be addressed is the substrate temperature during deposition. It has been shown that MgO films grown on molybdenum at 300 K and 600 K are not equivalent in terms of EPR spectroscopy [16]. After preparation at 300 K a strong EPR-signal close to the free electron g-value was found at X-band whereas the 600 K preparation is EPR silent in this region. The signal is located in the bulk and is most likely related to trapped electrons which are thought to be located at dislocation lines [56]. It disappears after annealing the 300 K preparation to 1100 K. However, although the 300 and the 600 K preparation are morphologically similar, as shown by STM [106], after additional electron treatment a different behavior between the two films remains. Thus, from an EPR point of view molybdenum is an interesting substrate for the exploratory investigation planned at W-band.

In the following, preparations on both substrates are described followed by a characterization with Auger electron spectroscopy. The morphology of thin MgO films grown on silver was further imaged by STM to test the performance of the microscope.

5.1.1 MgO Film Preparation

Two different procedures were followed in cleaning the Mo(100) single crystal. In a first attempt the crystal was mounted on setup **I** as shown in section 3.4. Repeated cycles of oxidation (1×10^{-6} mbar, 1400 K), argon bombardment (5×10^{-6} mbar, 20 μA), and annealing (1500 K) were conducted similar to [103]. This procedure never succeeded in obtaining a carbon free surface after the final annealing step according to AES. Going to higher temperatures even worsened the situation. The thermal coupling between the sample and the rest of the setup led to a high background pressure during annealing ($\geq 1 \times 10^{-8}$ mbar) and increased the degree of contamination. In a second approach the single crystal is mounted as shown in Fig. 3.11, setup **II**. This allows annealing to 2000 K whilst keeping the pressure below 5×10^{-9} mbar. The single crystal is then cleaned by repeated cycles of oxidation at 600 K (1×10^{-6} mbar, 1 min) and subsequent flashing to 2000 K. This closely follows the preparation of molybdenum single crystals by the group of Goodman [158]. The difference is a higher oxygen partial pressure at a lower oxidation temperature in the present case. Goodman *et al.* apply 1000 to 1300 K and an oxygen atmosphere of 1.3×10^{-7} mbar. After several cleaning cycles no impurities can be found by AES and a sharp (1×1) LEED pattern is obtained.

The silver single crystal is mounted as shown in sample setup **I** (section 3.4) as only mild temperatures are needed during cleaning and growth. Repeated cycles of Ar^+ sputtering (5×10^{-6} mbar, 20μA) and annealing to 650 K remove impurities. Before MgO growth no contaminations are found by AES and a sharp (1×1) LEED pattern is observed.

The MgO is prepared by Mg evaporation in an oxygen atmosphere (1×10^{-6} mbar). The substrate is either kept at room temperature or at 600 K. The dependence of the film thickness on the substrate temperature is discussed below.

5.1.2 MgO Film Thickness

In the experiment the MgO film thickness is calibrated with a quartz microbalance (QMB). Deposition onto the microbalance is in all cases conducted at room temperature. However, the MgO films are grown at 300 K as well as at 600 K. A possible temperature dependence of the sticking coefficient would remain undetected by sole use of the QMB. Therefore, Auger electron spectroscopy is applied to compare the growth behavior at the two temperatures mentioned. To gain insight into the absolute film thickness the Auger results are also compared to values expected from literature.

To simulate the expected behavior of the intensity ratio the following expression for an overlayer covered substrate can be used [47, 120]:

$$\frac{I_L}{I_S} = \frac{I_L^{\infty}\left\{1 - exp\left(\frac{-d}{cos\,\theta \cdot \lambda_L^{MgO}}\right)\right\}}{I_S^{\infty} \cdot exp\left(\frac{-d}{cos\,\theta \cdot \lambda_S^{MgO}}\right)} \tag{5.1}$$

The left hand side of eq. 5.1 gives the ratio of the intensities of an overlayer element (L) and the substrate (S). In principal either the intensities of oxygen or magnesium can be used for the overlayer element. As the determination of the magnesium intensities is much more difficult than for oxygen due to the retarding field analyzer used here the latter intensity is employed. The Mg(KLL) transition is only measured to ensure the formation of an MgO film. The numerator on the right in eq. 5.1 describes the asymptotic rise of the oxygen signal with growing MgO thickness d. Respectively, the denominator specifies the decay of the substrate metal signal. I_X^{∞} is the intensity expected for infinitely thick material. In the case of silver and molybdenum this value is obtained by an AES measurement of the bulk material. For oxygen the value was extrapolated from measurements of thick MgO films. λ_X^{MgO} is the inelastic mean free path (IMFP) for the electron of the according Auger process in MgO. The factor $(cos\ \theta)^{-1}$ in the exponent accounts for the increase of the average traveling distance of the electrons caused by the large acceptance angle of the retarding field analyzer used here. For the present optics an average angle of 42° is appropriate [120]. The intensity of the primary electron beam is assumed constant for the thickness range investigated. In table 5.1 IMPF values for the two electron energies of interest are given. The values obtained from the three sources are based on different theoretical models that were built upon available optical data. The calculated thickness dependence is shown in Fig. 5.1 along with the experimental results.

The Auger intensities of oxygen and the metal substrate were determined for MgO films of varying thickness and grown at different substrate temperatures. The MgO deposition rates varied between 2 and 5 Å/min as indicated by the QMB. The higher rate was used if large amounts had to be deposited. No differences between the films grown at various rates were observed by AES. All Auger measurements in this section were performed without post-annealing of the MgO films. The Auger spectra were measured in differential mode. The modulation amplitude was kept such that the line shape in the Auger profile remained constant for the transitions of interest. This ensures that the peak-to-peak intensity is proportional to the Auger current in the signal [150]. The ratio of the O(KLL)

transition [$\mathbf{E}_{kin}$]	Akkerman *et al.* [2]	Tanuma *et al.* [143]	Kwei *et al.* [90]
Ag(MNN)[350 eV]	9.74 Å	11.38 Å	11.88 Å
O(KLL) [501 eV]	12.65 Å	14.90 Å	15.39 Å
Mo(MNN) [185 eV]	6.67 Å	8.00 Å	7.94 Å

Table 5.1: IMPF values for electrons with E_{kin} in MgO.

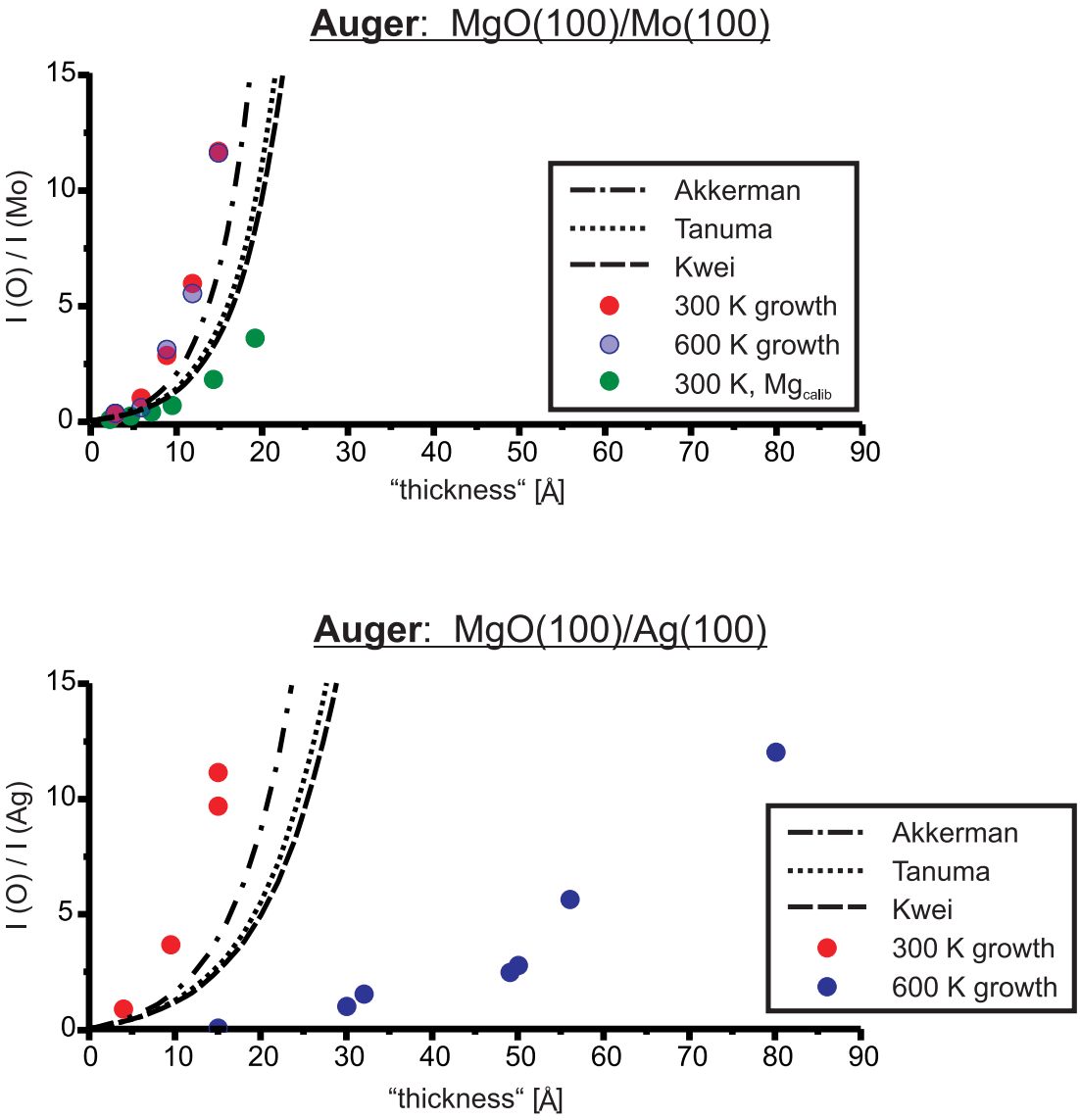

Figure 5.1: Measured and calculated Auger intensity ratios of oxygen to silver and oxygen to molybdenum; experimental settings: $I_0 = 3$ keV, 12 μA, $U_{mod} = 5$ eV.

peak-to-peak intensity to the according Ag(MNN) or Mo(MNN) intensity was determined.

In Fig. 5.1 the intensity ratios of the 300 and 600 K preparations are plotted as a function of the thickness given by the QMB. The top and bottom parts show the intensity ratio of oxygen to molybdenum (I(O)/I(Mo)) and oxygen to silver (I(O)/I(Ag)), respectively. The red dots indicate deposition at 300 K, blue dots 600 K. The quartz microbalance was calibrated while magnesium was deposited in an oxygen atmosphere using the parameters (density and acoustic impedance) of MgO with the exception of one calibration where magnesium was evaporated in absence of the oxygen atmosphere. In the latter case the growth of the oxide was evaluated taking the relative magnesium density in metallic magnesium and MgO into account. The result is shown in green in the upper plot of Fig. 5.1. All experimental curves follow an exponential growth. However, substantial differences depending on temperature and calibration type are observed. In the case of molybdenum the Auger intensity ratios of the 300 and 600 K preparation using the MgO calibration of the QMB basically coincide. The room temperature preparation using the magnesium parameters differs considerably. Compared to the MgO calibration the actual thickness of the film as determined by Auger spectroscopy is reduced by a factor of two with respect to the nominal thickness inferred from the QMB. Drastic differences are observed for the 300 and 600 K preparations on silver. To match the two experimental curves the QMB thickness of the 600 K preparation has to be divided by a factor of five.

For molybdenum the exponential curves calculated using the IMFP values from literature grow slower than the experimental values, but the spread within the theoretical models is in the same range as the deviation from the measured values. This statement also holds for the 300 K preparation on silver. For molybdenum as well as silver the best agreement between the 300 K preparation using the MgO parameters and the literature is obtained by using the IMFP values by Akkerman *et al.* (dashed-dotted curve in Fig. 5.1) [2]. The deviation for MgO on molybdenum is within 20% whereas for silver the QMB derived values are up to 35% higher than those by Akkerman *et al.*

Several reasons might be responsible for the deviation between the 300 K preparations using MgO parameters and the calculated curves. As the growth mode of MgO on the QMB is unknown a systematic error can be hidden in the used density. The calculated curves also contain several error sources. First of all, electron backscattering is not included in the model. As silver and molybdenum have higher atomic numbers than oxygen and magnesium neglecting the backscattering should lead to an underestimation of the amount of Auger processes in the MgO layer by the calculation [22, 96]. A correction in this regard shifts the theoretical curves towards the experimental ones. The model also does not properly reflect the roughness of the film. The metal substrates are not completely flat neither are the films grown on them. The Auger metal signal observed on rougher films is higher than for a flat film of the same average thickness [120]. This aspect shifts the theoretical curves to higher thickness and thus further away

from the experimental measurements. Another problem can be the IMPF values themselves. They are derived using the density of bulk MgO. For MgO on silver the oxide lattice is expanded compared to the bulk and for molybdenum contracted [156]. Therefore the electron densities of the thin films are slightly different from the bulk. As the density directly enters the equations to obtain the IMFP values they will be slightly changed [2, 90, 143]. A further source of error in eq. 5.1 is the determination of the absolute intensities I_X^∞ which are more error-prone than the intensity ratios as the absolute value depends on the slight variation in experimental conditions, e.g., sample position and angle or electron flux. As these parameters are similar for subsequent measurements, the errors introduced average out when the ratio of the intensities is taken.

Valeri *et al.* achieved good agreement between their Auger spectra and calculated values using 10 Å for λ_{Ag}^{MgO} and 13 Å for λ_O^{MgO} in the same thickness range as investigated in the present experiment [148]. The IMPF values are close to those by Akkerman *et al.* which also have the best agreement to the data shown here. However, they calibrated the QMB for magnesium and not MgO. For this reason the magnsium calibrated ratios are also shown in Fig. 5.1. Experimentally, the two calibrations differ in several aspects. Most importantly, the magnesium evaporation may be influenced by the presence of oxygen which can oxidize magnesium in the evaporator. Thus, the rate of evaporation might be slower for magnesium in an oxygen atmosphere. In this case the calibration for magnesium overestimates the film thickness of the oxide. This agrees well with the observation in Fig. 5.1. Additionally, equal sticking coefficients for magnesium metal and MgO have to be assumed. In the case of the Valeri group it has to be mentioned that in later work for MgO films grown on molybdenum the thickness derived from IMFP values and XPS deviates by a factor of two from STM estimations [13,14]. This might be taken as an indication that the absolute thickness is not easily determined. However, a trend can clearly be seen.

The main conclusion that can be drawn from the experimental data shown is that there is no difference in the film thickness as determined by AES on molybdenum comparing the two substrate temperatures used. For silver the two preparations are not nearly equal. In principal two mechanisms can be responsible for this effect: The first one is a change of the sticking coefficient with increasing temperature. This is in the current case unlikely. Even if the initial sticking onto the silver is different at the two temperatures the MgO growth on existing MgO layers should follow the same behavior as for films grown on molybdenum. The second explanation involves the high mobility of silver atoms on the (100) surface [3, 163, 167]. During film growth the mobile silver atoms are expelled and form silver islands. MgO films on silver are in most cases prepared at temperatures around 300 K. However, there exist some studies on films where the preparation temperature is between 500 and 600 K [84, 86, 114, 134]. From these studies only Schintke *at al.* mention that adatom diffusion leads to partial covering of MgO islands in the submonolayer regime [114]. This is in agreement to NiO(100)-films grown on Ag(100) where NiO partially sinks into the silver substrate during

growth already between 300 and 400 K [60, 121]. How far silver migrates during MgO growth at 600 K is not reported in the literature. Recently measured XPS data in our institute show the same behavior for the 300 and 600 K preparation on silver as introduced here by Auger: the thickness going from 300 K to 600 K has to be adjusted by a factor of four to obtain the same XPS intensities [129]. This is close to the factor of five extracted in the current work. Excepting a model of silver migration during MgO film growth the question remains whether all silver can be covered and which thickness is necessary to do so. At least in infrared measurements using CO after gold deposition silver is not observed above a thickness of 40 Å [129].

In conclusion, the quartz microbalance readings for the room temperature preparations are in line with the thicknesses obtained by Auger spectroscopy and IMFP values. Furthermore, the 600 K preparation on molybdenum shows the same behavior as the room temperature preparation in AES. For silver the deposition temperature strongly influences the thickness as derived by AES. This seems to be caused by silver migration at elevated temperature. The extent of the migration is not known so far. In the remainder of this thesis the thickness of the MgO films is given in MLs as determined by the QMB. With the MgO lattice constant of 4.2 Å a 2 Å deposition at room temperature equals about a 1 ML thick film. To indicate the problematic situation regarding the thickness of the 600 K preparation on the silver substrate quotation marks will be used.

5.2 Atomic Resolution in STM

The morphology of the silver single crystal itself as well as MgO on silver was imaged by STM. To test the performance of the Omicron STM and adjust some parameters measurements on the reconstructed Si(111) surface were performed first. The reasons to start with silicon are the well reproducible preparation of the (7×7) reconstruction of the Si(111) surface, the imaging properties of the surface structure, and the vast knowledge about the system (for an overview see, e.g., [35,155]). The procedure and outcome on the silicon surface will be discussed briefly before turning to silver and MgO.

The preparation of the silicon was done in the following way: A stripe of silicon ($10 \times 1 \times 1$ mm^2) was mounted on an Omicron sample plate. Similar to setup **I** in section 3.4 the narrow edges of the single crystal rest on sapphire pieces and the silicon was clamped down with molybdenum springs. One of the springs was grounded in this case. The second one was connected to the high voltage pad. Direct heating was used for annealing and the temperature was read with a pyrometer. Initial preparation of the silicon crystal consisted of slow annealing to degas the sample. The pure silicon is a poor conductor at room temperature. In order to run current through the sample a slowly increasing voltage was applied. At a certain point – about 80 V for the present conditions – the voltage broke down to 16 to 18 V due to a marked increase of conductivity. Degassing at

600 K was continued until the chamber pressure settled at about 3×10^{-10} mbar. The final preparation step consisted in several flashes to 1300 K followed by slow cooling. At high temperature sublimation of the surface oxide layer takes place, while the reconstruction to the (7×7) surface occurs during the cooling at about 1160 K [155].

The tungsten tip used here was prepared by putting it into the standard Omicron tip holder plate and mounting it onto the cryostat of the preparation chamber. The tip was brought into contact with a filament and heated until a white glow was observed. The result of this preparation regarding the sharpness of the tip was monitored by field emission. On average, application of 1.4 kV to the filament while keeping the tip grounded led to emission currents of about 1 μA at a separation of 0.3 mm.

In Fig. 5.2 images of the silicon surface are shown along with a model of the surface structure as derived by Takayanagi *et al.* using transmission electron diffraction [142]. The so-called DAS model (dimer-adatom-stacking fault) in Fig. 5.2 a) consists of one adatom layer and two reconstructed layers beneath. The 12 silicon adatoms per unit cell are arranged in a (2×2) structure (colored circles). The first reconstructed layer is a stacking-fault layer (larger open circles), the second reconstructed layer is characterized by vacancies at the corners of the unit cell and nine dimers on the sides of each of the triangular subcells (smaller open circles). The unreconstructed silicon underneath is indicated by solid circles and dots. While the atoms of the stacking-fault layer of the right-hand triangle in Fig. 5.2 a) sit in the regular position, the atoms of the left-hand triangle have the faulted sequence.

In Fig. 5.2 b) the silicon surface was imaged using -0.8 V sample bias and a tunneling current of 0.3 nA. The image is governed by dark spots arranged in a hexagonal lattice and 12 bright spots that are enclosed by connecting 4 nearest neighbor dark spots. The dark spots correspond to the vacancies at the corners, while the bright spots correspond to the 12 adatoms of a unit cell. One unit cell and the positions of the adatoms of another one are indicated in color. Imaging the silicon was done to test the performance of the STM and it proved that atomic resolution can be obtained.

Furthermore, as the lattice parameters of the reconstructed Si(111) surface are well-known the absolute values of the x- and y-axis in the surface plane could be adjusted. Additionally, the lateral displacement could be calibrated to avoid larger drifts along one axis than the other. An improvement is seen going from Fig. 5.2 b) to c). While the diagonals of the unit cell in the first case enclose an angle of 96° in the lower image the angle is 90.5° which is close to the expected value of 90°. Whereas in the upper image (Fig. 5.2 b)) the occupied states were probed, in the lower image (Fig. 5.2 c)) tunneling occurred via the unoccupied states. This differs from previous experiments where better contrast was generally observed at negative bias [146]. However, they did not exclude a better contrast for a certain positive bias range. In conclusion, the Si(111) (7×7) serves as an easy tool for parameter calibration and performance test of the STM.

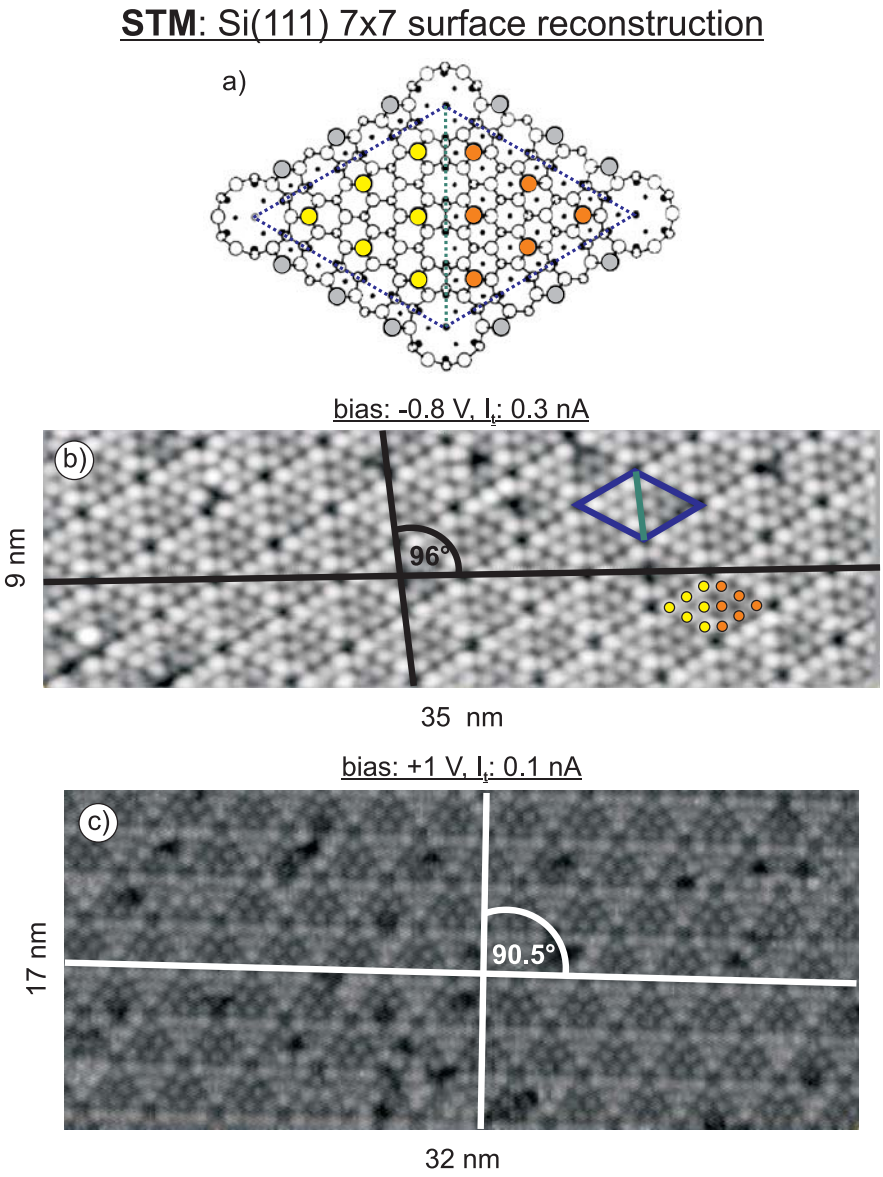

Figure 5.2: a) model of the Si(111) 7×7 surface reconstruction [142], for details see text; b) Si(111) 7×7 surface structure as revealed by STM; c) equalizing x- and y-drift seen in b).

5.2.1 MgO/Ag in STM

In Fig. 5.3 images of the silver single crystal after cleaning (sputtering and annealing) and an MgO film grown on top are shown. The silver surface exhibits broad terraces that can have a width of several 10 nm. No defects are seen in the area shown. This proves that the cleaning procedure can produce large defect free terraces. However, the STM image was taken on a flat area on the surface and is not necessarily representative for the whole crystal surface. As mentioned in section 5.1 the silver single crystal tends to exhibit roughness macroscopically with time. This aspect is not reflected in the STM image shown.

Growth of the MgO film was carried out at 600 K and "2.5 ML" were deposited. The image was taken at a high positive bias where tunneling occurs via the unoccupied states of the MgO film. Square-shaped islands are observed in accordance with previous data [114, 137, 149]. They are aligned along the [001] and [010] directions [114]. In the literature MgO terrace sizes of typically 50 nm width are given for MgO on silver at a 2 ML coverage [114]. In the current case the terraces appear to be smaller which might already be due to a higher step density on the silver substrate. To obtain larger MgO terrace sizes UHV cleaved crystals have to be used [9]. In this case the terraces are accompanied by adstructures and holes of considerable size.

The present image does not contain information about silver migration. At this stage the sole idea was to reproduce the morphology known from literature.

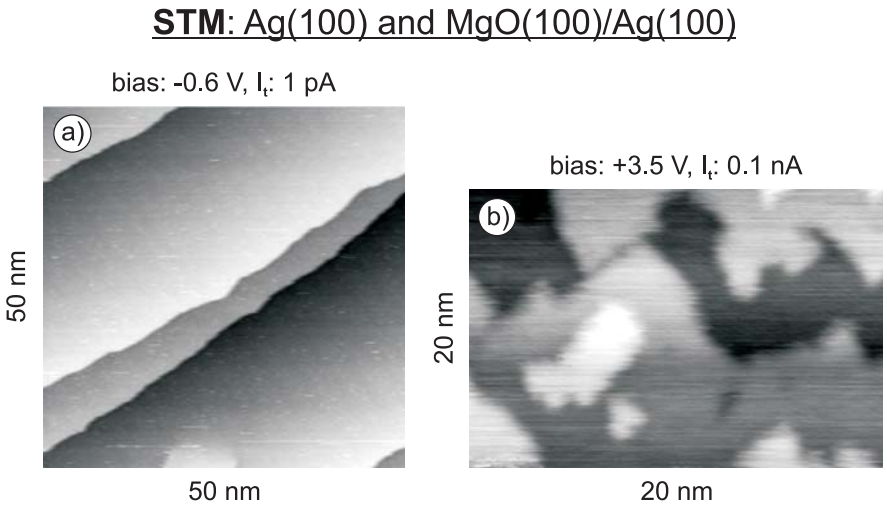

Figure 5.3: a) Ag(100), b) "2.5 ML" MgO(100)/Ag(100).

5.3 N_2O Adsorbed on MgO(100)/Ag(100) Probed by IR

In this section IR spectra of N_2O adsorbed on thin MgO(100) films are discussed as a function of coverage and temperature. All adsorption experiments were performed on MgO films grown on a silver substrate at 600 K. As discussed in section 5.1.2 the composition of this MgO film is not well-known, yet. However, the results can be directly compared to those obtained for MgO films grown on molybdenum in this laboratory [93] as well as N_2O on the silver single crystal. This allows a detailed comparison which may also help to resolve the structure ambiguity.

Apart from its importance as a greenhouse gas the general interest in adsorption of N_2O arises from its capability to serve as an oxidizing agent and an oxygen source. It has been shown in many powder experiments that paramagnetic color centers on the MgO surface (F_s^+-centers) react with N_2O according to [108, 136, 144, 157]:

$$F_s^+ + N_2O \longrightarrow O^- + N_2 \tag{5.2}$$

However, the general adsorption properties of N_2O on well-defined MgO surfaces have only been scarcely investigated theoretically and experimentally. Apart from the work done in this laboratory the analysis focuses on the well-ordered N_2O phase formed on ideal terraces of the MgO(100) surface [68, 159].

The IRAS spectra presented in the following were recorded using a spectral resolution of 4 cm^{-1}. The base pressure of the preparation chamber was $< 2{\times}10^{-10}$ mbar. The single crystal was cooled with liquid helium and the temperatures are given according to the reading of the type C thermocouple. For N_2O deposition the doser in the IR-chamber was used (see section 3.3.3, Fig. 3.9). Due to the experimental setup the coverage had to be determined by a calibration experiment which can distinguish between mono- and multilayer absorption. The pressure at the inlet of the doser was chosen such that the dynamical range allowed submonolayer dosage on the time scale of seconds.

Fig. 5.4 a) shows IR spectra of N_2O taken at 42 K on a "20 ML" MgO film prepared at 600 K as a function of coverage. Absorption lines are found in two spectral ranges: One between 2275-2230 cm^{-1} and one between 1300-1265 cm^{-1} which are assigned to the asymmetric (ν_3) and the symmetric stretching vibration (ν_1), respectively. The corresponding gas phase values are 2223.9 cm^{-1} and 1285.5 cm^{-1} [12]. At low coverage, the ν_3 region has a band at 2243 cm^{-1} and a small dip at 2270 cm^{-1}. Up to 0.35 ML the line at 2243 cm^{-1} increases in intensity and shifts slightly to the blue. Additionally, a new signal appears at 2232 cm^{-1} that has the strongest intensity at intermediate coverage (0.5-1.6 ML) and continuously shifts to 2235 cm^{-1}. Initially the bands at 2270 cm^{-1} and 2243 cm^{-1} are still seen as distinct shoulders of the new peak at 2235 cm^{-1}, but after 1.3 ML of N_2O deposition a single band is observed that is anisotropically broadened on the high frequency side. A further increase in coverage reveals a

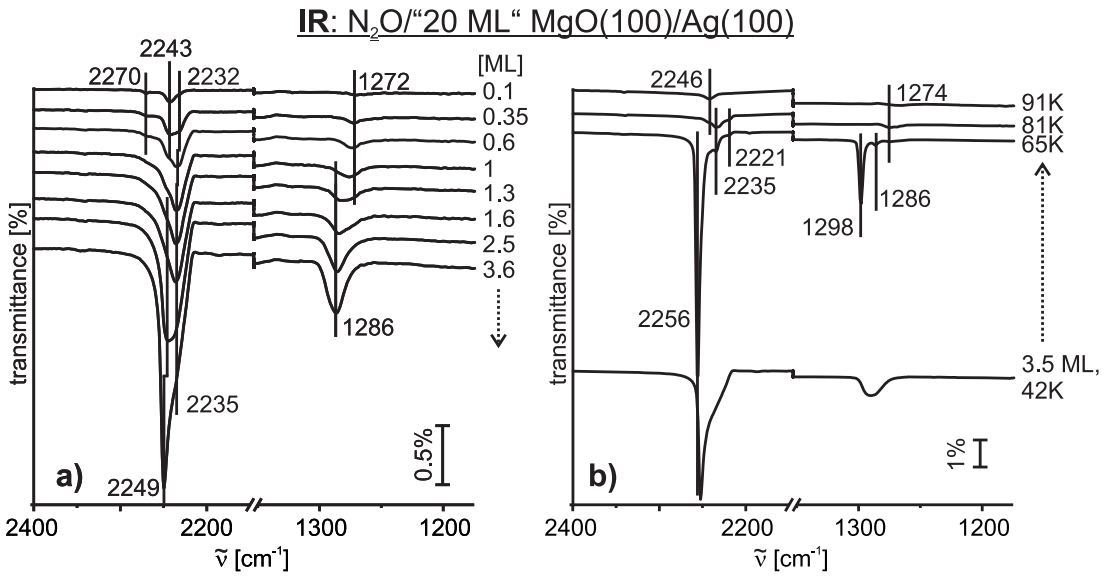

Figure 5.4: a) IR spectra of increasing coverages of N_2O, b) IR spectra taken after an initial dosing of N_2O and subsequent annealing to the temperatures indicated; all spectra are measured at 42 K, the dotted arrow indicates the time direction of the experiment.

new line at 2245 cm^{-1} that shifts to 2249 cm^{-1} at higher coverage and finally dominates this part of the spectrum while the band at 2235 cm^{-1} remains to be seen as shoulder.

The ν_1 band at about 1272 cm^{-1} is initially shallow. It gains intensity with coverage and shifts to higher wavenumbers. Starting at about 1 ML a new band grows at 1286 cm^{-1} which leads to one broad band in the ν_1 region for intermediate coverages. This line continuously gains intensity with increasing coverage. At high coverage only the line at 1286 cm^{-1} is observed.

The multitude of bands in the ν_3 region as a function of coverage suggests that different adsorption sites exist on the MgO surface. The annealing experiment shown in Fig. 5.4 b) reveals the temperature dependence of the different lines. Prior to adsorption of 3.5 ML of N_2O at 42 K the MgO film used in Fig. 5.4 a) was annealed to 600 K. After dosage the spectrum at the bottom of Fig. 5.4 b) is observed which exhibits the same two bands also dominating at high coverage in Fig. 5.4 a). After annealing to 65 K a sharp peak at 2256 cm^{-1} is found with two distinct features on the low frequency side at 2235 cm^{-1} and 2221 cm^{-1} that are of much smaller intensity. Upon annealing to 81 K the band at 2256 cm^{-1} disappeares while in addition to the lines at 2235 cm^{-1} and 2221 cm^{-1} the band at 2246 cm^{-1} is observed again. Annealing to 91 K extinguishes all ν_3 lines except the one at 2246 cm^{-1}. A band at 2270 cm^{-1} cannot be found in the annealing experiment. In the ν_1 region the first annealing step leads to a sharp band at 1298 cm^{-1} and two small bands at 1286 cm^{-1} and 1274 cm^{-1}. After annealing to

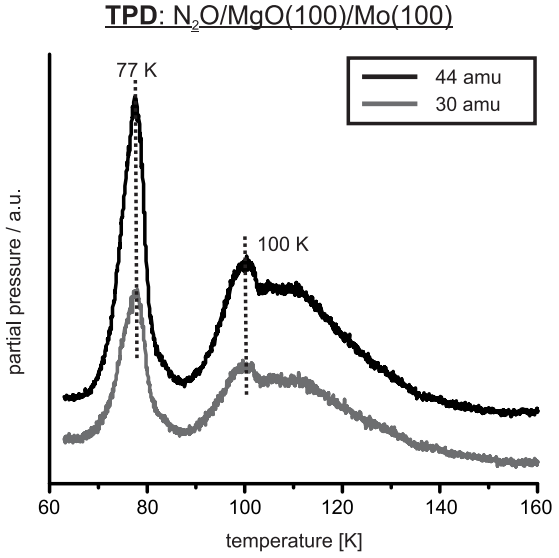

Figure 5.5: TPD spectrum taken after dosing 3 L N_2O at 63 K on a 20 ML thick MgO film, taken from [93].

81 K only the band at 1274 cm^{-1} remains observable which is very shallow after the final annealing step to 91 K.

To relate the temperature dependence of the infrared bands to N_2O desorption from the surface a thermal programmed desorption (TPD) experiment performed on a 20 ML thick MgO film on molybdenum is shown in Fig. 5.5 [93]. Subsequent to the preparation at 600 K the film was annealed to 1100 K and 3 L of N_2O were dosed at 63 K. It has to be mentioned here that the expression one monolayer in the present thesis is interchangeable with the quantity referred to as one Langmuir [L] in [93]. The monolayer is defined below. The detected masses of 44 amu and 30 amu represent N_2O and its fragment NO. As the ratio between both curves remains the same for the temperature recorded, CO_2 (44 amu) interference from the background is excluded. The first huge peak at 77 K is related to multilayer desorption [116]. On the high temperature side at 84 K a small shoulder is buried in the multilayer peak according to [93]. Another desorption peak is found at 100 K which is followed by a broad feature that ranges up to 140 K.

The initial step of the IR annealing experiment suggests that the structure within the adsorbed layer as well as the resulting IR band is dependent on the temperature the adsorbed layer was exposed to. Whereas the IR band is rather broad at the deposition temperature the first annealing step significantly sharpens the whole IR spectrum pointing towards an increase of internal order. This step is accompanied by an increase in intensity which might originate from readsorption as the initial annealing of the sample filament after deposition was accompanied by a substantial increase of background pressure ($\sim 7\times10^{-10}$ mbar). In comparison to the TPD experiment the sharp peaks at 2256 cm^{-1} and 1298 cm^{-1} can be assigned to the multilayer as they disappear after annealing to 81 K. The

exact position of the multilayer bands is temperature dependent. As was seen in the annealing experiment in Fig. 5.4 b) the dominating peaks at deposition temperature shift to higher wavenumbers upon heating. Due to this effect and the experimental observation that the equivalent peaks in the coverage series in Fig. 5.4 a) at 2249 cm^{-1} and 1286 cm^{-1} cannot be saturated (not explicitly shown here) they are attributed to multilayer adsorption. As at high coverage only the band at 1286 cm^{-1} is observed in the ν_3 region, this band consists of monolayer and multilayer contributions. The completion of the first monolayer and initial growth of the multilayer can be estimated by analysis of the ν_1 region in Fig. 5.4 a). One monolayer is taken as the coverage directly before the new intensity growth sets in on the high frequency shoulder of the band at 2235 cm^{-1} (at $\sim$ 2245 to 2249 cm^{-1}). The other coverages were denoted in comparison to the N_2O deposition time of the monolayer.

To assign the multiple lines in the monolayer regime the structure of the MgO film has to be recalled. As mentioned in section 5.1.2 the film composition of a "20 ML" thick MgO film grown at 600 K on silver is not properly known. More precisely, the presence of silver on the film surface could not be excluded by the experimental data at hand. For this reason N_2O was also directly adsorbed on silver which is shown below. Furthermore, the defect density on grown films is significantly higher than for UHV cleaved MgO single crystals [9,14,54,138]. Therefore, besides regular adsorption on terrace sites also adsorption on defect sites can be expected. An assignment to different adsorption sites on the MgO surface can be simplified by comparing MgO films with different defect concentrations. This is possible by exploiting the fact that MgO films grown on molybdenum exhibit a higher number of defects than on silver. Additionally, the defect density of MgO films on molybdenum can be influenced by an annealing step to 1100 K after the 600 K preparation [132,138]. A film obtained after the 600 K preparation is called 'pristine', after post-annealing to 1100 K the term 'annealed' is used. Before conclusions about N_2O adsorption on MgO(100)/Ag(100) are drawn adsorption on silver (Fig. 5.6) and two differently prepared MgO films on molybdenum (Fig. 5.7) are discussed.

Fig. 5.6 shows IR spectra of N_2O on silver taken at 30 K as a function of coverage. In the ν_3 region two peaks at 2278 cm^{-1} and 2226 cm^{-1} are observed at small coverages. The lower frequency band has a shoulder at 2213 cm^{-1}. The peak at 2226 cm^{-1} dominates the spectrum and at 1 ML coverage the shoulder at 2213 cm^{-1} can no longer be distinguished in the wing of the main band. Above 1 ML the main band shifts to higher wavenumbers and at final coverage a peak at 2246 cm^{-1} is observed with a pronounced low frequency shoulder. The band at 2278 cm^{-1} remains as a small shoulder on the high frequency side of the main peak. In the ν_1 region initially one band is seen at 1280 cm^{-1} which shifts to lower wavenumbers with increasing coverage. At 1.5 ML the line significantly broadens. A further increase in coverage leads to a peak at 1286 cm^{-1} that is accompanied by a shoulder at 1296 cm^{-1}.

Fig. 5.7 shows adsorption of one monolayer of N_2O on 20 ML thick MgO films

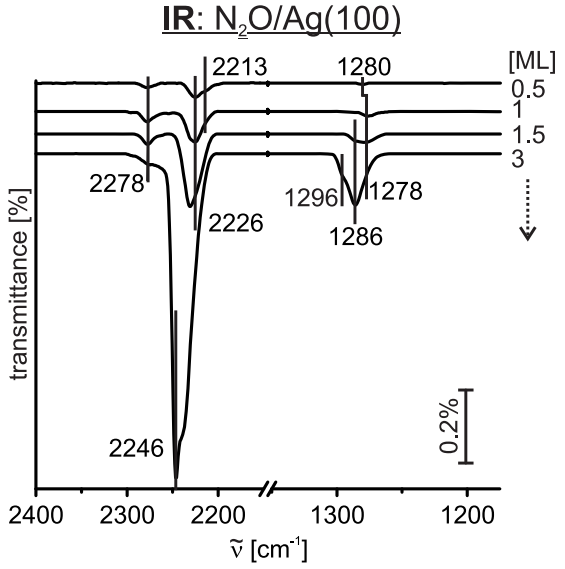

Figure 5.6: IR spectra of increasing coverages of N_2O adsorbed on silver, all spectra are measured at 30 K, the dotted arrow indicates the time direction of the experiment.

(600 K) grown on Mo(100) and Ag(100), respectively. The data for molybdenum are taken from [93]. The spectrum on silver is the monolayer coverage of Fig. 5.4 a). The preparation on molybdenum leads to three distinct features in the ν_3 region and one in the ν_1 region. The band in the ν_1 region appears at 1276 cm^{-1} and coincides with the band on MgO(100)/Ag(100) at this coverage. On the annealed film on molybdenum the ν_3 region is dominated by a peak at 2235 cm^{-1}. Two bands with similar intensity are found at about 2246 cm^{-1} and 2270 cm^{-1}. On the pristine film a pronounced increase of the band at 2246 cm^{-1} is observed. On MgO(100)/Ag(100) the band at 2235 cm^{-1} governs the spectrum at monolayer coverage and the two additional features at higher frequencies mainly lead to an anisotropical broadening of the main peak. The better resolution of the ν_3 region on molybdenum is attributed to the temperature of deposition as inferred from the annealing experiment on silver which results in similar sharp features (compare Fig. 5.4 b)).

Independently of the substrate – the silver single crystal or the various MgO films – the ν_3 region consists of several features in the monolayer regime indicating a noticeable interaction of this vibration with the substrate. This behavior is not seen in the ν_1 region suggesting a smaller interaction with the underlying substrate. In the following the features in the ν_3 region are discussed first. The band at about 2235 cm^{-1} reigns the spectrum for the preparation on MgO on silver and still dominates the spectrum for the annealed film on molybdenum. The peak at about 2246 cm^{-1} is most pronounced on the pristine film, still of considerable intensity for the annealed film, but considerably smaller on silver. The band at 2270 cm^{-1} is of similar size for the two preparations on molybdenum

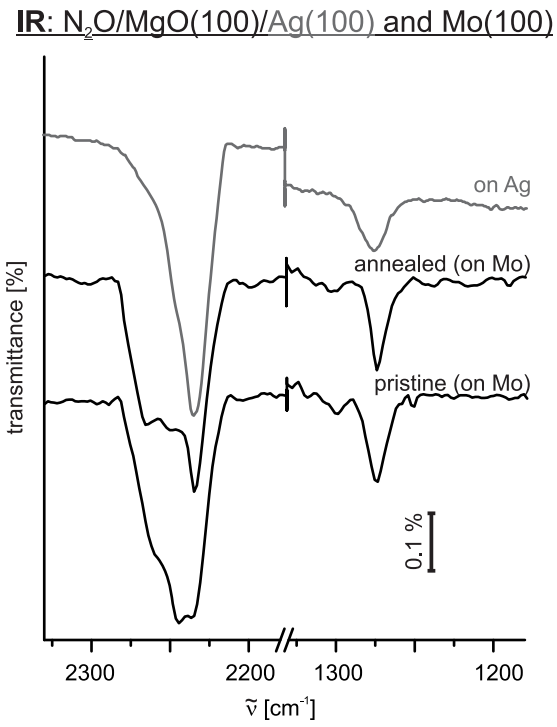

Figure 5.7: IR spectra of N_2O adsorbed on 20 ML thick MgO films grown on silver and molybdenum, respectively; deposition conditions for silver: 1 ML, 42 K, for molybdenum: 1 L, 63 K.

and contributes significantly to the integrated intensity whereas it is only weak for the MgO film grown on silver. Furthermore, the temperature behavior of this line is different for the two substrates. As seen in the annealing experiment in Fig. 5.4 b) the band at 2270 cm^{-1} cannot be identified after multilayer desorption at 81 K. On molybdenum, however, the peak is a distinct feature of the spectrum even after annealing to 90 K [93].

The behavior of the band at 2235 cm^{-1} is expected for a species that adsorbs on the MgO terrace as the number of these sites increases by going from the pristine film on molybdenum to the annealed one to the film grown on silver. The higher-frequency features can be assigned to defect site adsorption. This is supported by the annealing experiment in Fig. 5.4 b). The species found at about 2246 cm^{-1} is bound stronger whereas the band at 2235 cm^{-1} is not observed after annealing to 91 K. This is consistent with the idea that small molecules bind stronger to low-coordinated than regular sites which is well-established for CO on MgO(100) [42, 154] and theoretically confirmed for N_2O on MgO [159]. The IR band at about 2235 cm^{-1} is correlated to the shoulder at 84 K in the TPD spectrum (Fig. 5.5) [93] whereas desorption at higher temperatures is assigned to defect sites. On molybdenum the band at 2270 cm^{-1} was suggested to originate from adsorption on dislocations [93] which are known to be sensitive to the preparation conditions [13, 14]. This species should be even less frequent on the film

grown on silver. However, additionally this peak exhibits a different temperature stability as pointed out above. Due to this behavior it is not obvious whether this band arises from the same adsorption sites on the two substrates. The N_2O adsorption directly on silver does not exhibit ν_3 peaks that coincide with those on MgO. This indicates that the MgO film on silver does not contain larger amounts of silver agglomerates on the surface, but adsorption on silver atoms, ions or small clusters can currently not be excluded. Under these conditions a direct assignment to specific sites on the MgO surface other than the terraces remains currently impossible.

So far, the band at 2221 cm^{-1} appearing in the annealing experiment (Fig. 5.4 b)) has not been addressed. As bands with similar wavenumbers are observed for N_2O adsorption on silver (Fig. 5.6) adsorption on the metal would be one possibility. However, as the peaks on silver already appear at initial coverage whereas it is only observed after annealing on MgO this assignment is unlikely. IR data on UHV cleaved MgO single crystals at 80 K reveal two bands at 2229.6 cm^{-1} and 2217 cm^{-1} in the ν_3 region [68]. The authors assign these to the symmetric and antisymmetric collective vibration of the ν_3 band split by a correlation field. Both bands are further red shifted than the band arising from adsorption on terrace sites in the present case. However, the band at 2221 cm^{-1} appears after reorganization of the adsorbed layer by annealing and could be due to a collective vibration. As the antisymmetric band at 2217 cm^{-1} has a dynamical dipole parallel to the surface only the observation of the symmetric component in the present experiment is expected. In addition to the temperature dependence of the ordered structure, the higher defect concentration of the MgO films compared to the single crystal mentioned above can impede the formation of the densely packed N_2O layer.

As pointed out previously the ν_1 vibration in the monolayer regime does not exhibit dependency on different surface sites. However, the growth of the multilayer shifts the band to higher wavenumbers. In Fig. 5.4 a) the band at 1272 cm^{-1} slowly vanishes after the monolayer coverage is reached whereas the dominant monolayer feature in the ν_3 region at 2235 cm^{-1} which was assigned to terrace sites remains seen as a shoulder even at high coverage. Thus, the multilayer adsorption in the coverage series shifts the monolayer ν_1 band to 1286 cm^{-1}. After reorganization in the annealing experiment (Fig. 5.4 b)) the multilayer peak is at 1298 cm^{-1} and the line at 1286 cm^{-1} is more prominent than the band at lower frequencies. However, upon desorption of the multilayer also the peak at 1286 cm^{-1} vanishes whereas the line at about 1274 cm^{-1} gains intensity. This indicates that in contrast to the ν_3 band the frequency of the ν_1 band in the monolayer is strongly influenced by the adsorption of the multilayer.

In addition to an assignment of N_2O adsorption to specific surface sites the absolute shifts compared to the gas phase values have to be analyzed. In comparison to the gas phase value of 2223.9 cm^{-1} the monolayer bands in the ν_3 region between 2275 and 2230 cm^{-1} are blue shifted. The only exception is the band at 2221 cm^{-1}. The upward shift can partially be understood by dipole-dipole

interaction of neighboring molecules as it is also present in the multilayer with its band at 2256 cm^{-1} (2249 cm^{-1} after deposition at 42 K). The different blue shifts for different surface sites imply that electrostatic and polarization effects which are important for the IR frequencies play a considerable role in the adsorption of N_2O. This is also reflected in the different temperature stability of the species involved. In comparison, the ν_1 region consists of a single peak in the monolayer regime indicating that the according vibration is much less sensitive towards the adsorption site. However, the band is red shifted compared to the gas phase value of 1285.5 cm^{-1} and the multilayer adsorption at 1298 cm^{-1} (1286 cm^{-1} after deposition at 42 K). Dipole-dipole interactions explain the blue shift of this band with increasing coverage, but cannot contribute to the overall red shift. Instead modification of the electronic structure induced by the bonding to the surface must be responsible. Similar shifts were found for N_2O coordinated to Ru(II) in molecular complexes, on alkali-halide films, and α-Cr_2O_3 powder [25,85,165]. On α-Cr_2O_3 powder the adsorption was assigned to two different geometries: oxygen end down or nitrogen end down [165]. The species with a red shift in the ν_1 region and a blue shift in the ν_3 region comparable to the present case was interpreted as N_2O bound via the oxygen to the cation. That a bond in the case of MgO is also established between N_2O and the Mg cation is supported by theory that predicts very low binding energies to surface oxygen [159]. The calculations suggest that binding is preferentially done via the nitrogen end down, but the energy difference to the oxygen bound case is small (30 meV for five-coordinated Mg^{2+}, 40 meV for four-coordinated Mg^{2+}). Bonding to the five-coordinated cation is weaker than to defect sites which is in agreement with the temperature dependent IR data. However, as Scagnelli *et al.* failed to find N_2O bound to MgO terrace sites with a theoretical approach similar to [159] the reliability of the theoretical results are difficult to judge [113].

In conclusion, N_2O adsorption on terraces of MgO films could be identified and two possible defect sites observed using IR spectroscopy. The results obtained for MgO films grown on silver were compared to those grown on molybdenum which have a significantly higher defect density. The structure within the adsorbed layer is dependent on the temperature of exposure indicating a barrier for the formation of the ordered layer. The comparison with N_2O adsorption on silver showed that the absorption bands for the 'thick' MgO film differ in frequency from those on silver. However, adsorption on single silver atoms, ions, or small clusters cannot be excluded.

5.4 EPR measurements in UHV

For the first EPR experiments in a UHV environment a paramagnetic species was sought for that could be deposited onto the planar mirror in varying amounts under UHV conditions. Additionally, these species should allow the number of spins present on the surface to be estimated in order to determine the current

sensitivity of the spectrometer. Di-tert-butyl nitroxide (DTBN) was selected as it is a liquid with a vapor pressure of 1.4 torr at 25°C and therefore can be dosed into the UHV system [101]. Its molecular structure has already been shown in Fig. 2.2.

The choice of the substrate – the planar mirror of the resonator – for DTBN was based on the following considerations: Adsorption on a metal substrate leads to suppression of the EPR-signal of molecules in electronic contact to the metal surface due to spin exchange with the conduction electrons [79, 104]. Quenching of an unknown amount of adsorbed molecules would hamper the purpose of using DTBN to determine the sensitivity of the Fabry-Perot resonator. The exchange interaction with the metal can be impeded by an insulating oxide layer. It was shown for an Al_2O_3 film grown on NiAl(110) that a thickness of 5 Å is sufficient to observe submonolayer quantities of DTBN [78]. In the current case a molybdenum single crystal was used as the planar mirror. As an insulating layer, a 20 ML thick MgO(100) film was grown at 600 K. The thickness of the MgO film is far above the value where electronic substrate effects are expected. The reason to employ MgO as the insulating layer is motivated by the perspective to use this film for investigations of a number of point defects already known from X-band measurements (see section 5.1 and below).

The experiments were performed with a base pressure $< 2 \times 10^{-10}$ mbar in the transfer chamber. The lowest temperature reached with the EPR-cryostat while cooling with liquid Helium was 70 K measured with a type C thermocouple. This temperature is higher than that obtained on the cryostat of the preparation chamber (mentioned in section 5.3) which might be caused by the different cryostat setups, especially the copper extension on the EPR manipulator (Fig. 4.5). The DTBN was adsorbed on the sample surface at 70 K.

The DTBN radical was purchased from Aldrich (300721) with a declared purity of 90 %. The liquid (it solidifies at -6°C) was filled in a glass tube with a CF 16 flange and sealed with a valve. A T-piece enabled the glass tube to be connected to the leak valve of the transfer chamber on one side and on the other side to a pump that could be separated by a valve. Prior to use the DTBN was degassed by several freeze-thaw cycles. As DTBN reacts with the walls of the UHV system, those have to be passivated before the adsorption on the sample by background dosing is performed. For this purpose the transfer chamber was filled with DTBN for 600 s at 1×10^{-7} mbar. Afterwards the EPR cryostat was cooled down with helium. The MgO/Mo sample was annealed to 700 K prior to the experiment and then transferred into the transfer chamber. 700 K was chosen as no desorption of DTBN and its framgents was observed above 600 K on alumina [78].

In Fig. 5.8 EPR spectra of two different DTBN coverages as well as a background spectrum are shown. The experimental series was carried out in the following way: The sample on the EPR cryostat was positioned in the transfer chamber compartment. Background dosing in the resonator position is not possible as the cryostat acts as a cryopump and thus prevents molecules from reaching

the surface inside the titanium tube. 3 L were dosed onto the sample at 70 K. After placing the sample in the measurement position about 1 hour passes until a mechanical stability is reached that allows an EPR experiment. The range of the active stabilization element – the Peltier element introduced in section 4.2.4 – is sufficient to keep the resonator on resonance for several hours. After the EPR measurement the sample was transferred to the preparation chamber and annealed to 700 K. Above this temperature no further desorption of DTBN and its fragments was observed with the quadrupole mass spectrometer in line with the previous experiments on alumina [78]. Afterwards 0.38 L were dosed in the transfer chamber and the EPR spectrum was measured following the above procedure. Finally, the annealing step in the preparation chamber was repeated and a background spectrum recorded.

After dosing 3 L the spectrum in Fig. 5.8 is dominated by a single Lorentzian-like line that is centered at $g = 2.006$ and has a peak to peak linewidth of 18.3 G. This EPR line is significantly broadened for the 0.38 L DTBN coverage exhibiting a linewidth of 34.3 G. Furthermore, a small g-shift to higher magnetic field values is found. The background spectrum shows three distinct features that are shaded in red. These are also observed in the DTBN spectra (due to the scaling they are difficult to identify in the topmost spectrum). By comparing the spectra the phase shifts observed for the background features indicate that they are not on the sample surface for which the phase is set to allow only absorption under the conditions of critical coupling. Additionally, a broad feature is seen in the background spectrum that cannot be distinguished from the DTBN signal in the spectra above. Subtracting this feature from the 0.38 L spectrum introduces a slight asymmetry in the DTBN signal. The feature centered at $g = 2.012$ is also seen at this position but with varying line shape in other data sets. Nevertheless this signal can be used for internal comparison.

The DTBN line after absorption of 3 L is governed by exchange narrowing. The observed g-value for the single line agrees with values found in the literature (2.0056 on alumina [97], 2.0058 on oxidized copper [104]). DTBN multilayer measurements on Al_2O_3 show that the linewidth is strongly dependent on the temperature of exposure [78]. To this end it is important to realize that optimal exchange coupling requires certain geometric orientations of the molecules with respect to each other. Even though the results suggest that the molecules tend to arrange such as to optimize exchange coupling this arrangement requires a certain degree of mobility [77]. Thus, at X-band a wide range of linewidths between approximately 10 and 35 G has been observed depending on the preparation conditions [78]. The present linewidth of 18.3 G is in line with these observations. The broadened signal at 0.38 L coverage cannot be attributed to a temperature effect as the preparation procedure was not changed. Instead the smaller absolute number of molecules involved is expected to lead to a reduction of the exchange taking place. If the distance between adjacent spins increases, the strength of the exchange coupling weakens and might not be sufficient to completely average g- and hyperfine anisotropy, thus leading to a broadening of the line. This effect can

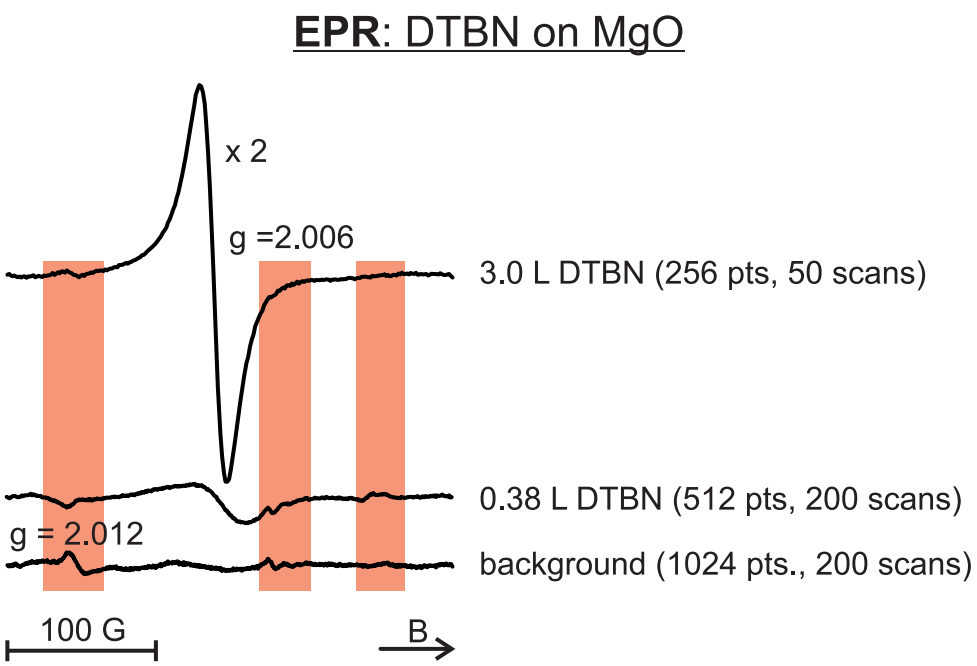

Figure 5.8: Different coverages of DTBN on the MgO surface; experimental settings: MA: 4 G, RG: 40 dB, tc: 20.48 ms, CT: 40.96 ms, MW att.: 20 dB, T_{sample} = 70 K.

also be the reason for the observed g-shift compared to the higher coverage. However, as the background is not featureless in the DTBN region it might contribute to this g-shift. At the current stage, those two effects cannot be discriminated.

The number of molecules N_{DTBN} on the surface while dosing at a certain pressure p for a time Δt is calculated by application of kinetic gas theory:

$$N_{DTBN} = \frac{pA\Delta t}{\sqrt{2\pi mkT}} \tag{5.3}$$

Inserting the following values: T = 300 K, M (DTBN) = 145 g/mol, k = 1.38×10^{-23} J/K, A = $\pi\times$(6 mm)^2 and assuming a sticking coefficient of one the number of DTBN molecules in dependence of p and Δt can be determined. As the purity of the purchased DTBN is declared as 90 %, the number of paramagnetic species reduces to $N_{spins} = 0.9\ N_{DTBN}$. The calculated values are tabulated in table 5.2. The table also includes the intensity I of the EPR signal as determined by a double integration of the spectra shown here after subtraction of the background features. This intensity is directly proportional to the number of spins. For unknown amounts of paramagnetic species the comparison of these intensities with quantified species allows conclusions about their number. The number obtained for the smaller DTBN coverage is about a factor of 20 smaller than the available surface oxygen sites (1.12×10^{15} O-atoms/cm^2). This indicates that DTBN adsorbs in a submonolayer and supports the argument that the EPR signal is broadened due to weaker spin-spin interactions.

species	I [a.u.]	N_{spins}/cm^2
DTBN, 3.0 L	24.1×10^3	4.55×10^{14}
DTBN, 0.38 L	5.22×10^3	5.69×10^{13}
MgO (300 K)	322	$3.1\text{-}5.4\times10^{12}$

Table 5.2: Number of spins observed inferred from kinetic gas theory and double integration of the EPR signal.

The intensity ratio expected for the two DTBN preparations is 8 to 1 comparing the nominal dosages. However, experimentally a ratio of 5 to 1 is found. Several uncertainties are involved in the method applied: Most error-prone is the double integration of the EPR spectra. The accuracy relies on an appropriate baseline correction that becomes more difficult the broader the signals are. In turn, the determination of the intensity of the 0.38 L deposition has a larger error margin. Although distinct background features are reproduced in subsequently measured spectra some vary in line shape and field position thus hampering an unambiguous background correction. A further source of errors in the intensities observed is the assumption that every molecule hitting the surface sticks and remains EPR active. This is not necessarily the case as DTBN can react with defects present on the surface as well as the walls of the chamber. To minimize the latter effect the chamber was passivated prior to the experiment as mentioned above. It proved that this did not always succeed to the same extent using the same dosing times and pressures. In the experimental series presented here the larger amount of DTBN was dosed first. This was done on purpose as it proved impossible to start with the smaller amount: no EPR signal was observed in this case after initial dosing. This suggests that at first contact between MgO and DTBN a reaction whose nature is not known leads to quenching of paramagnetic species. Under these conditions the error margins on the determined intensities are large as is seen by comparing the expected and the observed intensities for the two DTBN coverages, but the method should allow a determination of other paramagnetic quantities within a factor of two to three. The numbers obtained this way represent rather upper limits due to the assumptions involved.

The purpose of the W-band spectrometer is the characterization of paramagnetic species on oxide films that are in general only present in submonolayer quantities. The smaller DTBN coverage already indicates that the sensitivity of the spectrometer allows to observe those species. In the following the first W-band EPR measurements of a paramagnetic species in an oxide film under UHV conditions are presented.

As mentioned in section 5.1 an EPR signal is found at X-band after preparation of an MgO film at 300 K [56]. The paramagnetic species belonging to this signal are located in the MgO bulk and they are assigned to defects on dislocation lines or grain boundaries. Theoretical calculations support the existence of elec-

tron traps at line defects [100]. The signal disappears after annealing to 1100 K. Electron bombardment of this film produces a signal similar to the initial one with respect to the position and linewidth but much larger in amplitude. Alternatively, the annealed film can be reacted with hydrogen atoms. Again, a signal increase compared to the initial EPR spectrum is observed [16]. The electron as well as the hydrogen induced signal vanish after annealing. The g-value of the single line is in all cases centered at about 2.003 with only minor variations as measured at X-band. In the current case, one of these signals shall be reproduced at W-band to directly correlate the sensitivities that can be obtained with the two spectrometers. For this purpose 20 ML MgO were prepared on molybdenum at 300 K. After confirmation of the presence of MgO by AES the sample was transferred onto the EPR cryostat and cooled to 70 K. The EPR measurements on this sample are shown in Fig. 5.9.

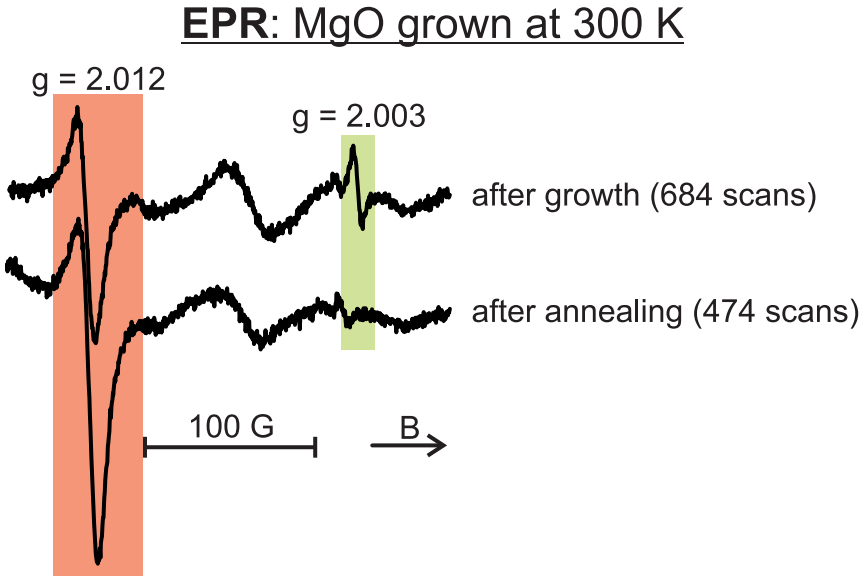

Figure 5.9: Top: MgO film after preparation at 300 K, bottom: after annealing the film to 1100 K; experimental settings: MA: 4 G, RG: 40 dB, tc: 20.48 ms, CT: 40.96 ms, MW att.: 20 dB, 1024 pts, $T_{sample} = 70$ K.

The spectrum obtained after the preparation at 300 K possesses two sharp lines at $g = 2.012$ and 2.003. The signal at 2.003 has a linewidth of 5 G and is preceded by a small sharp peak. Additionally, wave-like features dominate the baseline. The spectrum after annealing exhibits the same broad features but misses the signal at $g = 2.003$. The signal at $g = 2.012$ is the same as already seen in Fig. 5.8. As mentioned its origin is in the resonator and the presence allows internal comparison of g-shifts. Of higher interest for the current study is the vanishing of the signal at 2.003 after annealing. This is the behavior expected for the paramagnetic defects observed at X-band. To correlate the W-band signal with the X-band signal the Auger confirmation after preparation

has to be remembered. This measurement inherently bombards the sample with electrons. Thus, the species seen in Fig. 5.9 corresponds to the X-band signal after electron bombardment. The linewidth of 5 G is similar to the value obtained at X-band. This indicates that the linewidth of this class of defects does not intrinsically broaden with increasing microwave frequency. This is important as a linewidth increase not only complicates the detection of a signal but also would reduce the gain in spectral resolution that is aspired at higher frequencies. At X-band the signal is related to about 1.4×10^{13} $spins/cm^2$ on a 20 ML film [56]. At this point it has to be mentioned that the yield of the electron bombardment is strongly dependent on the temperature of the sample during bombardment but also on the electron energies and deposition times involved. In the present case the electron bombardment was performed during an Auger measurement at 300 K. The process in the MgO film is induced by the primary and/or secondary electrons with $U_{prim} = 2$ keV. Deposition times were about 15 min and the emission current 12 μA. At X-band the substrate temperature is kept at 300 K as well, but the primary electrons have much lower energies ($\sim$ 100 eV), and deposition times and sample currents differ substantially (1 min, 1 mA). Furthermore, the sample areas of the two setups are not identical. Thus, the absolute yield of electron signal expected for the two experimental setups can differ. In the present case the number of paramagnetic species is determined by comparing the signal intensity to the intensities of the DTBN signals and their calculated number of spins. Depending on which DTBN coverage is chosen the amount of the MgO signal corresponds to 3.1 to 5.4×10^{12} $spins/cm^2$ (table 5.2). The numbers obtained at X- and W-band agree well considering the different experimental conditions and the error sources involved in the determination. This proves that the W-band spectrometer is capable to detect paramagnetic species in submonolayer regime on oxide films.

Furthermore, the sharp peak preceding the MgO signal shows that even smaller lines can be detected. Without the knowledge about the origin of this background signal it can be concluded that a signal with an intensity that is a factor of three smaller than the MgO signal is still well distinguishable from the noise. The signal observed directly after a preparation at 300 K consists at X-band of 1.9×10^{12} $spins/cm^2$. This is a factor of seven lower than the electron bombarded signal. If this ratio is also valid for the Auger induced signal some effort is necessary at W-band to obtain a sufficient signal to noise ratio. However, more problematic at W-band is the signal to background problem. Currently a lack of baseline stability limits the 'sensitivity' of the resonator. As can already be seen by comparison of Fig. 5.8 and Fig. 5.9 several features dominate the background and some change their amplitude and shape during an experimental series. This impedes an unambiguous background correction and thus complicates detection of small or broad signals. Similar problems also arose during the implementation of the X-band spectroscopy. For about ten years small details of the sample and resonator setup were modified to reach the current level of background reproducibility. Still, even at X-band the 'sensitivity' is limited by the

background issue rather than by the signal to noise ratio. A similar development can also be expected at W-band. One starting point is, e.g., the insulation of the antenna wire (see section 4.2.2) which initially did not show an EPR response in the field range involved, but that might have changed with the increase of sensitivity accomplished since then.

A main focus in the future will therefore be on the improvement of the background stability which is largely related to the mechanical reproducibility. Thus, refinements in the sample setup as well as the sample holder need to be achieved. Additionally, ideas exist to enhance the signal to noise ratio. Currently, the sensitivity of the signals observed at W- and X-band differs by about a factor of five. From a theoretical point of view an increase in sensitivity is to be expected (see section 2.1.7). This indicates that there is still room for improvement of the present Fabry-Perot resonator. As discussed in section 4.3.2 and section 4.3.3 the quartz window in the resonator changes the expected behavior of the field distribution in the resonator substantially. Not all possibilities to adjust to this experimental fact have been exploited, yet. Besides using higher radii of curvature also larger modes with the sample close to the window will be tested in the future. This will hopefully bring the sensitivity of the W-band spectrometer to that of the X-band spectrometer or beyond. Another aspect regarding signal intensity is the sample temperature during measurement. While the X-band measurements mentioned here are performed at $\sim$ 40 K the W-band limit is currently $\sim$ 70 K. In terms of Curie´s Law a change in sample temperature is inversely proportional to the signal intensity (see eq. 2.33). As the sample setup is more complex in the W-band system than the X-band system lowering the temperature further is not trivial, but slight improvement might still be possible keeping in mind the minimum temperature of the preparation cryostat of $\sim$ 40 K. One idea is the design of a cooling shield around the cryostat extension in Fig. 4.5.

In conclusion, the first measurements with a W-band EPR spectrometer under UHV conditions have been presented. An estimation of the detected number of spins has been given by dosing of the organic radical DTBN. This proved that sensitivities in the submonolayer regime can be reached under the current conditions. A first W-band EPR signal related to the defects in an MgO film has been shown. The paramagnetic centers observed are in the bulk and known from X-band measurements. As no increase in linewidth is detected by the change in frequency, the gain in spectral resolution at a higher magnetic field supports the idea of better discrimination of similar species in the future. The signal to background level as well as the signal to noise ratio are currently still lower than at X-band but ideas for improvement exist and have been discussed.

Chapter 6

Summary

Electron paramagnetic resonance (EPR) spectroscopy is a powerful method to determine geometric and electronic properties of paramagnetic species. However, on single crystalline surfaces the technique is scarcely used, chiefly because of its lack of inherent surface sensitivity. Nevertheless, EPR allows for studying paramagnetic species, e.g., defects on oxides that are difficult to probe by other surface science techniques. So far, the EPR spectrometers implemented for ultra high vacuum (UHV) conditions work at 9.5 GHz (X-band). The spectral resolution obtained at this frequency has proven to be insufficient for several systems of interest. That is to say similar species cannot be distinguished unambiguously. In this thesis is described the construction and preliminary tests of a UHV system that allows EPR spectroscopy at 94 GHz (W-band) – thus increasing the frequency by a factor of ten – and combines this technique with common surface science methods such as scanning tunneling microscopy (STM), infrared (IR) spectroscopy, low energy electron diffraction (LEED), thermal desorption spectroscopy (TPD) and Auger electron spectroscopy (AES). This combination with other techniques is of high significance in the case of EPR spectroscopy as EPR offers important information on the paramagnetic centers on the surface, which are usually present in low quantities. Thus, EPR spectroscopy needs to be complemented by other techniques for a profound picture of the processes on and the morphology of the surface.

The main challenge in this work was achieving an appropriate construction of an EPR resonator that fulfills the UHV condition and simultaneously maintains a high sensitivity towards paramagnetic species. On the basis of theoretical considerations a Fabry-Perot resonator was selected. In particular, a resonator was chosen that consists of a planar and a concave mirror. The sensitivity to mechanical disturbances, e.g., vibrations, is higher and the alignment of the mirrors more critical than for an equivalent resonator with two concave mirrors, however, the planar mirror offers the advantage of using the sample itself as the second mirror. Furthermore, in this design, the sample position is optimized regarding the field distribution with a minimum influence on the resonator properties. The adaption to UHV of this resonator succeeded by placing a 150 μm thick quartz

window to act as vacuum seal between the mirrors. This, however, demanded that the second mirror was also placed under low vacuum to limit the forces acting on the window. The resulting problems and their solutions were analyzed in detail within this thesis. For example, a proper microwave coupling into the resonator is more complicated under the condition of vacuum on both mirror sites. Three different methods for adjusting the coupling were tested. Finally, a combined method of antenna coupling in vacuum and a three-screw tuner at ambient conditions was selected. Furthermore, the mechanical stability of the resonator proved challenging: Due to the spatial limitations in the magnet the concave and the planar mirrors are not in good mechanical and thermal contact. For this reason the system is sensitive to vibrations and thermal drifts. To reduce the coupling of vibrations into the system, the setup was built on an optical bench that is mounted on an active vibration isolation system. Temperature gradients in the laboratory led to detuning of the resonator that could not be compensated by the automatic frequency control (AFC) of the EPR spectrometer. A feedback loop was developed that uses the offset determined by the AFC to correct the position of the concave mirror. This is achieved by a directed length change of the UHV chamber with the help of a Peltier element. Additionally, the influence of the quartz window onto the resonator properties was analyzed in detail. It was shown that positioning of the window close to the planar mirror is mandatory for optimum sensitivity. Furthermore, the presence of the window demands a different geometric design of the concave mirror. It was proven that concave mirrors with higher radii of curvature led to better signal-to-noise ratios which is different from the window free case.

The performance of the completed UHV assembly was tested on selected systems. The capability of the STM to produce atomically resolved images was proven on the reconstructed Si(111) surface. Furthermore, the morphological properties of thin magnesium oxide (MgO) films grown on Ag(100) could be reproduced. The MgO surface was used afterwards to probe the adsorption behavior of N_2O by infrared spectroscopy. This investigation was compared to prior studies on MgO(100)/Mo(100). The comparison showed that the IR spectra of N_2O reflect the different defect densities of the MgO films on the two substrates. The first UHV EPR spectra measured at W-band are the most significant results of the thesis. The measurements on the organic radical DTBN proved that the spectrometer adaptation to the pressure conditions succeeded and that paramagnetic species present in submonolayer quantities can be detected. Additionally, the measurements on MgO(100)/Mo(100) showed that paramagnetic centers on oxidic surfaces and interfaces can be investigated. Currently the reproducibility of the background as well as the sensitivity still lag behind those of the UHV X-band spectrometer in our lab. Therefore an improvement on background stability as well as sensitivity will still be an important issue in the further development of the W-band EPR spectrometer.

Bibliography

[1] A. Abragam, *The Principles of Nuclear Magnetism*, volume 32 of *International Series of Monographs on Physics*, Claredon Press, Oxford (1996).

[2] A. Akkerman *et al.*, *Inelastic Electron Interactions in the Energy Range 50 eV to 10 KeV in Insulators: Alkali Halides and Metal Oxides*, physica status solidi (b) **198**, 769 (1996).

[3] T. Ala-Nissila *et al.*, *Collective and Single Particle Diffusion on Surfaces*, Advances in Physics **51**, 949 (2002).

[4] G. Annino *et al.*, *High-Frequency EPR Applications of Open Nonradiative Resonators*, Journal of Magnetic Resonance **200**, 29 (2009).

[5] N. M. Atherton, *Principles of Electron Spin Resonance*, Ellis Horwood and Prentice Hall, New York (1993).

[6] P. W. Atkins, *Molecular Quantum Mechanics*, Oxford University Press, Oxford (1997).

[7] M. L. Bailly *et al.*, *A Spectroscopy and Catalysis Study of the Nature of Active Sites of MgO Catalysts: Thermodynamic Brønsted Basicity Versus Reactivity of Basic Sites*, Journal of Catalysis **235**, 413 (2005).

[8] J. Bardeen, *Tunnelling from a Many-Particle Point of View*, Physical Review Letters **6**, 57 (1961).

[9] C. Barth and C. R. Henry, *Atomic Resolution Imaging of the (001) Surface of UHV Cleaved MgO by Dynamic Scanning Force Microscopy*, Physical Review Letters **91**, 196102 (2003).

[10] M. Beckendorf, *Simulation und Experimente zur Elektronenspinresonanz von kondensiertem Stickstoffdioxid auf Einkristalloberflächen im Ultrahochvakuum*, PhD thesis, Ruhr-Universität Bochum (1994).

[11] M. Beckendorf *et al.*, *UHV-ESR Investigation of NO_2/Au(111)*, Journal of Physics-Condensed Matter **5**, 5471 (1993).

[12] G. M. Begun and W. H. Fletcher, *Infrared Spectra of the Isotopic Nitrous Oxides*, Journal of Chemical Physics **28**, 414 (1958).

[13] S. Benedetti *et al.*, *Morphology and Optical Properties of MgO Thin Films on Mo(001)*, Chemical Physics Letters **430**, 330 (2006).

[14] S. Benedetti *et al.*, *Structure and Morphology of Thin MgO Films on Mo(001)*, Physical Review B **78**, 195411 (2008).

[15] H.-M. Benia *et al.*, *Nucleation and Growth of Gold on MgO Thin Films: A Combined STM and Luminescence Study*, Journal of Physical Chemistry C **111**, 10528 (2007).

[16] H.-M. Benia *et al.*, *Electron Trapping in Misfit Dislocations on MgO Thin Films*, Physical Review B **81**, 241415 (2010).

[17] H.-M. Benia *et al.*, *Photon Mapping of MgO Thin Films with an STM*, Surface Science **601**, L55 (2007).

[18] M. Bennati and T. F. Prisner, *New Developments in High Field Electron Paramagnetic Resonance with Applications in Structural Biology*, Reports on Progress in Physics **68**, 411 (2005).

[19] T. Berger *et al.*, *The Color of the MgO Surface - a UV/Vis Diffuse Reflectance Investigation of Electron Traps*, Journal of Physical Chemistry B **108**, 7280 (2004).

[20] L. J. Berliner and J. Reuben, *Biological Magnetic Resonance*, volume 8 of *Spin Labeling, Theory and Applications*, Plenum Press, New York (1989).

[21] G. Binning *et al.*, *Surface Studies by Scanning Tunneling Microscopy*, Physical Review Letters **49**, 57 (1982).

[22] H. E. Bishop and J. C. Riviere, *Estimates of Efficiencies of Production and Detection of Electron-Excited Auger Emission*, Journal of Applied Physics **40**, 1740 (1969).

[23] F. Bloch, *Nuclear Induction*, Physical Review **70**, 460 (1946).

[24] J. F. Boas *et al.*, *Interpretation of Electron-Spin Resonance-Spectra Due to Some B12-Dependent Enzyme-Reactions*, Journal of the Chemical Society-Faraday Transactions II **74**, 417 (1978).

[25] F. Bottomley and J. R. Crawford, *Reactions between Nitrosylpentaammineruthenium(II) and Hydroxylamine or Hydrazine. Formation of (Dinitrogen Oxide)Pentaammineruthenium(II)*, Journal of the American Chemical Society **94**, 9092 (1972).

[26] G. D. Boyd and J. P. Gordon, *Confocal Multimode Resonator for Millimeter through Optical Wavelength Masers*, Bell System Technical Journal **40**, 489 (1961).

[27] G. Breit and I. I. Rabi, *Measurement of Nuclear Spin*, Physical Review **38**, 2082 (1931).

[28] L. Brunel, *Recent Developments in High Frequency/High Magnetic Field cw EPR. Applications in Chemistry and Biology*, Applied Magnetic Resonance **11**, 417 (1996).

[29] O. Burghaus *et al.*, *A Novel High-Field High-Frequency EPR and ENDOR Spectrometer Operating at 3 mm Wavelength*, Measurement Science & Technology **3**, 765 (1992).

[30] O. Burghaus *et al.*, *Superconducting Magnet Field Regulation for Electron-Paramagnetic-Resonance*, Journal of Physics E-Scientific Instruments **18**, 294 (1985).

[31] O. Burghaus *et al.*, *Proton ENDOR at a Microwave Frequency of 97 GHz*, Journal of Magnetic Resonance (1969) **80**, 383 (1988).

[32] P. M. Butcher, *Gunn Effect*, Reports on Progress in Physics **30**, 97 (1967).

[33] G. W. Chantry, *The Use of Fabry-Perot Interferometers, Etalons and Resonators at Infrared and Longer Wavelengths - an Overview*, Journal of Physics E - Scientific Instruments **15**, 3 (1982).

[34] C. J. Chen, *Theory of Scanning Tunneling Spectroscopy*, Journal of Vacuum Science & Technology A - Vacuum Surfaces and Films **6**, 319 (1988).

[35] C. J. Chen, *Introduction to Scanning Tunneling Microscopy*, Oxford University Press, New York (1993).

[36] M. S. Chen and D. W. Goodman, *Ultrathin, Ordered Oxide Films on Metal Surfaces*, Journal of Physics - Condensed Matter **20**, 264013 (2008).

[37] M. Chiesa *et al.*, *Single Electron Traps at the Surface of Polycrystalline MgO: Assignment of the Main Trapping Sites*, Journal of Physical Chemistry B **109**, 7314 (2005).

[38] R. N. Clarke and C. B. Rosenberg, *Fabry-Perot and Open Resonators at Microwave and Millimeter Wave Frequencies, 2-300 Ghz*, Journal of Physics E - Scientific Instruments **15**, 9 (1982).

[39] R. Collin, *Grundlagen der Mikrowellentechnik*, Technik Verlag, Berlin (1973).

[40] A. L. Cullen and P. K. Yu, *Complex Source-Point Theory of the Electromagnetic Open Resonator*, Proceedings Of The Royal Society Of London. Series A, Mathematical Physical And Engineering Sciences **366**, 155 (1979).

[41] K.-P. Dinse *et al.*, *Multi-Frequency EPR and DC Conductivity of Itinerant Spins in Single-Wall Carbon Nanotubes*, Applied Magnetic Resonance **37**, 595 (2010).

[42] Z. Dohnalek *et al.*, *Physisorption of CO on the MgO(100) Surface*, Journal of Physical Chemistry B **105**, 3747 (2001).

[43] D. Drakova, *Theoretical Modelling of Scanning Tunnelling Microscopy, Scanning Tunnelling Spectroscopy and Atomic Force Microscopy*, Reports on Progress in Physics **64**, 205 (2001).

[44] A. Dubinskii *et al.*, *An Investigation of Rotational Anisotropy of Nitroxyl Radicals by ESR Spectra in the 2 mm Range*, Theoretical and Experimental Chemistry **17**, 180 (1981).

[45] G. R. Eaton and S. S. Eaton, *High-Field and High-Frequency EPR*, Applied Magnetic Resonance **16**, 161 (1999).

[46] G. Ertl, *Reactions at Surfaces: From Atoms to Complexity (Nobel Lecture)*, Angewandte Chemie - International Edition **47**, 3524 (2008).

[47] C. S. Fadley, *Angle-Resolved X-Ray Photoelectron Spectroscopy*, Progress in Surface Science **16**, 275 (1984).

[48] E. Fermi, *Magnetic Moments of Atomic Nuclei*, Nature **125**, 16 (1930).

[49] S. A. Francis and A. H. Ellison, *Infrared Spectra of Monolayers on Metal Mirrors*, Journal of the Optical Society of America **49**, 131 (1959).

[50] M. Frank, *Vom Atom zum Kristallit: Struktur und Reaktivität oxidgetragener Metallpartikel*, PhD thesis, Humboltdt Universität Berlin (2000).

[51] J. H. Freed, *New Technologies in Electron Spin Resonance*, Annual Review of Physical Chemistry **51**, 655 (2000).

[52] H.-J. Freund, *Metal-Supported Ultrathin Oxide Film Systems as Designable Catalysts and Catalyst Supports*, Surface Science **601**, 1438 (2007).

[53] H.-J. Freund and G. Pacchioni, *Oxide Ultra-Thin Films on Metals: New Materials for the Design of Supported Metal Catalysts*, Chemical Society Reviews **37**, 2224 (2008).

[54] M. C. Gallagher *et al.*, *Structure of Ultrathin MgO Films on Mo(001)*, Thin Solid Films **445**, 90 (2003).

[55] M. Gerloch, *Magnetism and Ligand-Field Analysis*, Cambridge University Press, Cambridge (1983).

[56] A. Gonchar, *Private Communication* (2010).

[57] W. Gordy, *Theory and Applications of Electron Spin Resonance*, John Wiley & Sons, New York (1980).

[58] R. G. Greenler, *Infrared Study of Adsorbed Molecules on Metal Surfaces by Reflection Techniques*, Journal of Chemical Physics **44**, 310 (1966).

[59] O. J. Grinberg *et al.*, *Submillimeter Spectroscopy of Free-Radical ESR*, Doklady Akademii Nauk Sssr **230**, 884 (1976).

[60] S. Grosser *et al.*, *The Growth of Thin NiO Films on Ag(001) Studied by Scanning Tunneling Microscopy and Spectroscopy*, Surface and Interface Analysis **40**, 1741 (2008).

[61] S. Guimond, *Vanadium and Molybdenum Oxide Thin Films on Au(111) : Growth and Surface Characterization*, PhD thesis, Humboldt Universität Berlin (2009).

[62] J. B. Gunn, *Microwave Oscillations of Current in III-V Semiconductors*, Solid State Communications **1**, 88 (1963).

[63] P. L. J. Gunter *et al.*, *Surface Science Approach to Modeling Supported Catalysts*, Catalysis Reviews-Science and Engineering **39**, 77 (1997).

[64] W. R. Hagen, *High-Frequency EPR of Transition Ion Complexes and Metalloproteins*, Coordination Chemistry Reviews **192**, 209 (1999).

[65] U. Harbarth *et al.*, *Confocal Fabry-Perot Microwave Resonator at 48 GHz for High-Resolution Spectroscopy*, Journal of Physics E - Scientific Instruments **20**, 409 (1987).

[66] W. Hebenstreit *et al.*, *Atomic Resolution by Stm on Ultra-Thin Films of Alkali Halides: Experiment and Local Density Calculations*, Surface Science **424**, L321 (1999).

[67] E. Hecht, *Optics*, Addison-Wesley, San Francisco, 4. ed. (2002).

[68] J. Heidberg and B. Redlich, *The Adsorption of CO_2 and N_2O on the MgO(001) Single Crystal Surface: A Comparative PIRSS and LEED Study*, Surface Science **368**, 140 (1996).

[69] V. E. Henrich and P. A. Cox, *The Surface Science of Metal Oxides*, Cambridge University Press, Cambridge (1994).

[70] C. R. Henry, *Surface Studies of Supported Model Catalysts*, Surface Science Reports **31**, 235 (1998).

[71] F. M. Hoffmann, *Infrared Reflection-Absorption Spectroscopy of Adsorbed Molecules*, Surface Science Reports **3**, 107 (1983).

[72] J. M. Hollas, *Moderne Methoden in der Spektroskopie*, Vieweg Verlag, Wiesbaden (1995).

[73] P. Hollins, *The Influence of Surface Defects on the Infrared Spectra of Adsorbed Species*, Surface Science Reports **16**, 51 (1992).

[74] P. Hollins and J. Pritchard, *Infrared Studies of Chemisorbed Layers on Single Crystals*, Progress in Surface Science **19**, 275 (1985).

[75] T. Ito and J. H. Lunsford, *Synthesis of Ethylene and Ethane by Partial Oxidation of Methane over Lithium-Doped Magnesium-Oxide*, Nature **314**, 721 (1985).

[76] H. Kabashima *et al.*, *Conjugate Addition of Methanol to 3-Buten-2-One over Solid Base Catalysts*, Applied Catalysis A: General **214**, 121 (2001).

[77] U. J. Katter, *ESR-Untersuchung zum Adsorptionsverhalten und zur Dynamik von Di-Tertiärem-Butyl-Nitroxid (DTBN) auf einkristallinen Oberflächen im Ultrahochvakuum*, PhD thesis, Ruhr Universität Bochum (1995).

[78] U. J. Katter *et al.*, *Adsorption of the Stable Radical Di-Tert-Butyl Nitroxide (DTBN) on an Epitaxially Grown Al_2O_3 Film*, Journal of Physical Chemistry B **101**, 552 (1997).

[79] U. J. Katter *et al.*, *ESR and TPD Investigations of the Adsorption of Di-Tert-Butyl Nitroxide on Au(111) and NiO(111). Evidence for Long-Range Interactions*, Journal of Magnetic Resonance **126**, 242 (1997).

[80] L. Kevan and M. K. Bowman, *Modern Pulsed and Contniuous-Wave Electron Spin Resonance*, John Wiley & Sons, New York (1990).

[81] H. Kogelnik and T. Li, *Laser Beams and Resonators*, Applied Optics **5**, 1550 (1966).

[82] S. Kolaczkowski *et al.*, *Some Remarks on Reported Inconsistencies in the High-Field EPR Spectrum of DPPH*, Applied Magnetic Resonance **16**, 293 (1999).

[83] T. König *et al.*, *Measuring the Charge State of Point Defects on MgO/Ag(001)*, Journal of the American Chemical Society **131**, 17544 (2009).

[84] T. König *et al.*, *Work Function Measurements of Thin Oxide Films on Metals-MgO on Ag(001)*, Journal of Physical Chemistry C **113**, 11301 (2009).

[85] Y. Kozirovski and M. Folman, *Infra-Red Spectra of $N_2 0$ Adsorbed on Evaporated Films of NaCl, NaBr, and NaI*, Transactions of the Faraday Society **65**, 244 (1969).

[86] J. Kramer *et al.*, *Mechanism and Kinetics of Color Center Formation on Epitaxial Thin Films of MgO*, Surface Science **517**, 87 (2002).

[87] J. Krzystek *et al.*, *DPPH as a Standard for High-Field EPR*, Journal of Magnetic Resonance **125**, 207 (1997).

[88] H.-J. Kümmerer, *Hochfeld-ESR und Doppelresonanz an austauschgekoppelten Systemen*, PhD thesis, Universität Stuttgart (2004).

[89] H. J. Kümmerer *et al.*, *Spin Exchange between a Quantum Well and the Donor Layer in Si/Si1-Xcx*, Physical Review B **59**, 12568 (1999).

[90] C. M. Kwei *et al.*, *Electron Inelastic Mean Free Paths for Plasmon Excitations and Interband-Transitions*, Surface Science **293**, 202 (1993).

[91] L. D. Landau and E. M. Lifschitz, *Quantenmechanik*, volume 3 of *Lehrbuch der theorethischen Physik*, Akademie-Verlag, Berlin, 6. ed. (1979).

[92] I. N. Levine, *Quantum Chemistry*, Prentice Hall, New Jersey, 5. ed. (2000).

[93] J. C. Lian *et al.*, *$N_2 O$ Adsorption on the Surface of MgO(001) Thin Films: An Infrared and TPD Study*, The Journal of Physical Chemistry C **114**, 3148 (2010).

[94] X. Lin *et al.*, *Quantum Well States in Two-Dimensional Gold Clusters on MgO Thin Films*, Physical Review Letters **102**, (2009).

[95] X. Lin *et al.*, *Characterizing Low-Coordinated Atoms at the Periphery of MgO-Supported Au Islands Using Scanning Tunneling Microscopy and Electronic Structure Calculations*, Physical Review B **81**, (2010).

[96] C. Linsmeier, *Auger-Electron Spectroscopy*, Vacuum **45**, 673 (1994).

[97] G. P. Lozos and B. M. Hoffman, *Electron Paramagnetic Resonance of a Nitroxide Adsorbed on Silica, Silica-Alumina, Alumina, and Decationated Zeolites*, The Journal of Physical Chemistry **78**, 2110 (1974).

[98] W. B. Lynch *et al.*, *1 mm Wave Electron-Spin-Resonance Spectrometer*, Review of Scientific Instruments **59**, 1345 (1988).

[99] F. E. Mabbs and D. Collison, *Electron Paramagnetic Resonance of d-Transition Metal Compounds*, Elsevier, Amsterdam (1992).

[100] K. P. McKenna and A. L. Shluger, *Electron-Trapping Polycrystalline Materials with Negative Electron Affinity*, Nature Materials **7**, 859 (2008).

[101] M. M. Mestdagh *et al.*, *Hydrogenation of Di-Tert-Butyl Nitroxide Adsorbed on Supported Platinum Catalysts*, Journal of Physical Chemistry **79**, 1944 (1975).

[102] Y. N. Molin *et al.*, *Spin Exchange*, volume 8 of *Springer Series in Chemical Physics*, Springer, Berlin (1980).

[103] R. G. Musket *et al.*, *Preparation of Atomically Clean Surfaces of Selected Elements - a Review*, Applied Surface Science **10**, 143 (1982).

[104] M. Nilges and J. H. Freed, *UHV Electron-Spin-Resonance and CREMSEE - 2 Novel Surface Techniques*, Chemical Physics Letters **82**, 203 (1981).

[105] N. Nilius, *Properties of Oxide Thin Films and Their Adsorption Behavior Studied by Scanning Tunneling Microscopy and Conductance Spectroscopy*, Surface Science Reports **64**, 595 (2009).

[106] N. Nilius, *Private Communication* (2010).

[107] M. A. Ondar *et al.*, *ESR Spectroscopy in the Two-Millimeter Band and Magnetic-Resonance Parameters*, Soviet Journal of Chemical Physics—Khimicheskaya Fizika **2**, ISSN 0733 (1985).

[108] G. Pinarello *et al.*, *O^- Radical Ions on MgO as a Tool to Unravel Structure and Location of Ionic Vacancies at the Surface of Oxides: A Coupled Experimental and Theoretical Investigation*, Surface Science **494**, 95 (2001).

[109] A. B. Pippard, *Response and Stability*, Cambridge University Press, Cambridge (1985).

[110] C. P. Poole, *Electron Spin Resonance*, John Wiley & Sons, New York, 2. ed. (1983).

[111] T. F. Prisner *et al.*, *Pulsed 95 Ghz, High-Field EPR Heterodyne Spectrometer with High Spectral and Time Resolution*, Applied Magnetic Resonance **7**, 167 (1994).

[112] G. A. Rinard *et al.*, *Frequency Dependence of EPR Signal-to-Noise*, Journal of Magnetic Resonance **140**, 218 (1999).

[113] A. Scagnelli *et al.*, *Catalytic Dissociation of N_2O on Pure and Ni-Doped MgO Surfaces*, Surface Science **600**, 386 (2006).

[114] S. Schintke *et al.*, *Insulator at the Ultrathin Limit: MgO on Ag(001)*, Physical Review Letters **87**, 276801 (2001).

[115] S. Schintke and W. D. Schneider, *Insulators at the Ultrathin Limit: Electronic Structure Studied by Scanning Tunnelling Microscopy and Scanning Tunnelling Spectroscopy*, Journal of Physics - Condensed Matter **16**, R49 (2004).

[116] H. Schlichting and D. Menzel, *Techniques for Attainment, Control, and Calibration of Cryogenic Temperatures at Small Single-Crystal Samples under Ultrahigh-Vacuum*, Review of Scientific Instruments **64**, 2013 (1993).

[117] H. Schlienz *et al.*, *Electron-Spin-Resonance Investigations of the Molecular-Motion of NO_2 on Al_2O_3(111) under Ultrahigh-Vacuum Conditions*, Physical Review Letters **74**, 761 (1995).

[118] D. Schmalbein *et al.*, *The Bruker High-Frequency-EPR System*, Applied Magnetic Resonance **16**, 185 (1999).

[119] A. Schweiger and G. Jeschke, *Principles of Pulse Electron Paramagnetic Resonance*, Oxford University Press, New York (2001).

[120] M. P. Seah, *Quantitative Auger Electron Spectroscopy and Electron Ranges*, Surface Science **32**, 703 (1972).

[121] I. Sebastian *et al.*, *Scanning Tunnelling Microscopy on the Growth and Structure of NiO(100) and CoO(100) Thin Films*, Faraday Discussions **114**, 129 (1999).

[122] F. I. Shimabukuro *et al.*, *A Quasi-Optical Method for Measuring the Complex Permittivity of Materials*, IEEE Transactions on Microwave Theory and Techniques **32**, 659 (1984).

[123] J. W. Sidabras *et al.*, *Multipurpose EPR Loop-Gap Resonator and Cylindrical TE_{011} Cavity for Aqueous Samples at 94 GHz*, Review of Scientific Instruments **78**, 034701 (2007).

[124] V. Simic-Milosevic *et al.*, *Charge-Induced Formation of Linear Au Clusters on Thin MgO Films: Scanning Tunneling Microscopy and Density-Functional Theory Study*, Physical Review B **78**, (2008).

[125] H. J. M. Slangen, *Determination of Spin Concentration by Electron Spin Resonance*, Journal of Physics E - Scientific Instruments **3**, 775 (1970).

[126] C. P. Slichter, *Principles of Magnetic Resonance*, volume 1 of *Solid-State Sciences*, Springer, New York (1990).

[127] G. A. Somorjai and J. Y. Park, *Frontiers of Surface Science*, Physics Today **60**, 48 (2007).

[128] T. L. Squires, *Introduction to Microwave Spectroscopy*, George Newnes Limited, London (1963).

[129] M. Sterrer, *Private Communication* (2010).

[130] M. Sterrer *et al.*, *Identification of Color Centers on MgO(001) Thin Films with Scanning Tunneling Microscopy*, Journal of Physical Chemistry B **110**, 46 (2006).

[131] M. Sterrer *et al.*, *Interaction of Gold Clusters with Color Centers on MgO(001) Films*, Angewandte Chemie - International Edition **45**, 2630 (2006).

[132] M. Sterrer *et al.*, *When the Reporter Induces the Effect: Unusual IR Spectra of CO on Au_1/MgO(001)/Mo(001)*, Angewandte Chemie - International Edition **45**, 2633 (2006).

[133] M. Sterrer *et al.*, *Control of the Charge State of Metal Atoms on Thin MgO Films*, Physical Review Letters **98**, (2007).

[134] M. Sterrer *et al.*, *Crossover from Three-Dimensional to Two-Dimensional Geometries of Au Nanostructures on Thin MgO(001) Films: A Confirmation of Theoretical Predictions*, Physical Review Letters **98**, (2007).

[135] M. Sterrer *et al.*, *Palladium Monomers, Dimers, and Trimers on the MgO(001) Surface Viewed Individually*, Angewandte Chemie - International Edition **46**, 8703 (2007).

[136] M. Sterrer *et al.*, *Vacancies and Electron Deficient Surface Anions on the Surface of MgO Nanoparticles*, Journal of Physical Chemistry B **104**, 3601 (2000).

[137] M. Sterrer *et al.*, *Geometric Characterization of a Singly Charged Oxygen Vacancy on a Single-Crystalline MgO(001) Film by Electron Paramagnetic Resonance Spectroscopy*, Physical Review Letters **94**, 186101 (2005).

[138] M. Sterrer *et al.*, *Low Temperature Infrared Spectra of CO Adsorbed on the Surface of MgO(001) Thin Films*, Surface Science **596**, 222 (2005).

[139] M. Sterrer *et al.*, *CO Adsorption on the Surface of MgO(001) Thin Films*, Applied Catalysis A: General **307**, 58 (2006).

[140] S. Stoll and A. Schweiger, *An Adaptive Method for Computing Resonance Fields for Continuous-Wave EPR Spectra (Vol 380, Pg 464, 2003)*, Chemical Physics Letters **382**, 216 (2003).

[141] S. Stoll and A. Schweiger, *Easyspin, a Comprehensive Software Package for Spectral Simulation and Analysis in EPR*, Journal of Magnetic Resonance **178**, 42 (2006).

[142] K. Takayanagi *et al.*, *Structure-Analysis of Si(111)-7x7 Reconstructed Surface by Transmission Electron-Diffraction*, Surface Science **164**, 367 (1985).

[143] S. Tanuma *et al.*, *Calculations of Electron Inelastic Mean Free Paths .5. Data for 14 Organic-Compounds over the 50-2000 eV Range*, Surface and Interface Analysis **21**, 165 (1994).

[144] A. J. Tench *et al.*, *Oxygen Species Adsorbed on Oxides .1. Formation and Reactivity of $(O^-)_S$ on MgO*, Journal of the Chemical Society - Faraday Transactions I **68**, 1169 (1972).

[145] P. A. Tipler, *Physik*, Spektrum Akademischer Verlag, Heidelberg (1994).

[146] R. M. Tromp *et al.*, *Atomic and Electronic Contributions to Si(111)-(7×7) Scanning-Tunneling-Microscopy Images*, Physical Review B **34**, 1388 (1986).

[147] H. Ueda *et al.*, *Electron-Spin-Resonance Studies of DPPH Solutions*, Journal of Chemical Physics **36**, 1676 (1962).

[148] S. Valeri *et al.*, *Structural Study of Thin MgO Layers on Ag(001) Prepared by Either MBE or Sputter Deposition*, Thin Solid Films **400**, 16 (2001).

[149] S. Valeri *et al.*, *Scanning Tunnelling Microscopy of MgO Ultrathin Films on Ag(001)*, Physical Review B **65**, (2002).

[150] R. E. Weber and A. L. Johnson, *Determination of Surface Structures Using LEED and Energy Analysis of Scattered Electrons*, Journal of Applied Physics **40**, 314 (1969).

[151] R. T. Weber *et al.*, *Electron Spin-Echo Spectroscopy at 95 GHz*, Journal of Magnetic Resonance **81**, 129 (1989).

[152] J. A. Weil and J. R. Bolton, *Electron Paramagnetic Resonance*, John Wiley & Sons, Hoboken, New Yersey, 2. ed. (2007).

[153] J. E. Wertz, *Nuclear and Electronic Spin Magnetic Resonance*, Chemical Reviews **55**, 829 (1955).

[154] R. Wichtendahl *et al.*, *TDS Study of the Bonding of CO and NO to Vacuum-Cleaved NiO(100)*, Surface Science **423**, 90 (1999).

[155] R. Wiesendanger, *Scanning Probe Microscopy and Spectroscopy*, Cambridge University Press, Cambridge (1994).

[156] J. Wollschläger *et al.*, *Growth of NiO and MgO Films on Ag(100)*, Thin Solid Films **400**, 1 (2001).

[157] N. B. Wong and J. H. Lunsford, *EPR Study of $^{17}O^-$ on Magnesium Oxide*, Journal of Chemical Physics **55**, 3007 (1971).

[158] M. C. Wu *et al.*, *Preparation, Characterization, and Chemical Properties of Ultrathin MgO Films on Mo(100)*, Journal of Vacuum Science & Technology A - Vacuum Surfaces and Films **10**, 1467 (1992).

[159] Y. J. Xu *et al.*, *Theoretical Study of N_2O Adsorption and Decomposition at Regular and Defect Sites of MgO(001) Surface*, Journal of Theoretical & Computational Chemistry **2**, 57 (2003).

[160] B. Yang *et al.*, *CO Adsorption on Thin MgO Films and Single Au Adatoms: A Scanning Tunneling Microscopy Study*, Journal of Physical Chemistry C **114**, 8997 (2010).

[161] B. Yoon *et al.*, *Charging Effects on Bonding and Catalyzed Oxidation of CO on Au_8 Clusters on MgO*, Science **307**, 403 (2005).

[162] N. D. Yordanov, *Is Our Knowledge About the Chemical and Physical Properties of DPPH Enough to Consider It as a Primary Standard for Quantitative EPR Spectrometry*, Applied Magnetic Resonance **10**, 339 (1996).

[163] B. D. Yu and M. Scheffler, *Ab Initio Study of Step Formation and Self-Diffusion Ion Ag(100)*, Physical Review B **55**, 13916 (1997).

[164] M. Yulikov *et al.*, *Binding of Single Gold Atoms on Thin MgO(001) Films*, Physical Review Letters **96**, 146804 (2006).

[165] A. Zecchina *et al.*, *Infrared Study of Nitrous-Oxide Adsorption on Alpha-Chromia*, Journal of Catalysis **25**, 55 (1972).

[166] P. Zeeman, *On the Influence of Magnetism on the Nature of the Light Emitted by a Substance*, Philosophical Magazine **43**, 226 (1897).

[167] C. M. Zhang *et al.*, *Submonolayer Island Formation and the Onset of Multilayer Growth During Ag/Ag(100) Homoepitaxy*, Surface Science **406**, 178 (1998).

Abbreviations

AES	Auger electron spectroscopy
amu	atomic mass unit
a.u.	arbitrary units
CT	conversion time
cw	continuous wave
DPPH	2,2´-diphenyl-1-picrylhydrazil
DTBN	di-tert-butyl nitroxide
EPR	electron paramagnetic resonance
ESR	Elektronenspinresonanz
FT IR	Fourier transform infrared
FWHM	full width at half maximum
HPC	high pressure cell
IGP	ion getter pump
IMFP	inelastic mean free path
IRAS	infrared reflection-absorption spectroscopy
IR	infrared
L	Langmuir
LEED	low energy electron diffraction
MA	modulation amplitude
ML	monolayer
MW att.	microwave attenuation
NMR	nuclear magnetic resonance
PC	preparation chamber
QMB	quartz microbalance
QMS	quadrupole mass spectrometer

RG	receiver gain
STM	scanning tunneling microscope
TC	transfer chamber
tc	time constant
TPD	thermal programmed desorption
TDS	thermische Desorptionsspektroskopie
TMP	turbo molecular pump
TSP	titanium sublimation pump
UHV	ultrahigh vacuum
XPS	x-ray photoelectron spectroscopy

Abstract

The present PhD thesis describes for the first time the construction and preliminary tests of a system that allows electron paramagnetic resonance (EPR) measurements at 94 GHz (W-band) under ultra high vacuum (UHV) conditions and combines this technique with common surface science methods such as scanning tunneling microscopy (STM), infrared (IR) spectroscopy, low energy electron diffraction (LEED), thermal desorption spectroscopy (TPD) and Auger electron spectroscopy (AES).

The main challenge of this work was an appropriate construction of an EPR resonator that fulfills the UHV conditions and simultaneously maintains a high sensitivity towards paramagnetic species. On the basis of theoretical considerations a Fabry-Perot resonator was selected. In particular, a resonator was chosen that consists of a concave and a planar mirror with the latter being simultaneously the sample under investigation. The adaption of this resonator to UHV conditions succeeded by placing a 150 μm thick quartz window between both mirrors. This, however, demanded that the second mirror was also placed under low vacuum to limit the forces acting onto the window. A number of challenges with this design were analyzed in detail and are described within the thesis. For example, a proper microwave coupling into the resonator is more complicated to achieve under the condition of vacuum on both mirror sites. Three different methods for adjusting the coupling were tested. Finally, a combined method of antenna coupling in vacuum and a three-screw tuner at ambient conditions was selected. Furthermore, the mechanical stability of the resonator proved challenging: Due to the spatial limitations in the magnet the concave and the planar mirrors are not in good mechanical and thermal contact. For this reason the system is sensitive to vibrations and thermal drifts. To reduce the coupling of vibrations into the system, the setup was built on an optical bench that is mounted on an active vibration isolation system. Temperature gradients in the laboratory led to detuning of the resonator that could not be compensated by the automatic frequency control (AFC) of the EPR spectrometer. A feedback loop was developed that uses the offset determined by the AFC to correct the position of the concave mirror with the help of a Peltier element. Furthermore, the influence of the quartz window on the resonator properties was analyzed in detail. It was shown that positioning the window close to the planar mirror is mandatory for optimum sensitivity. Additionally, it was proven that concave mirrors with higher radii of curvature led to better signal-to-noise ratios which is different from the

window free case.

The performance of the completed UHV assembly was tested on selected systems. The capability of the STM to produce atomically resolved images was proven on the reconstructed Si(111) surface. Furthermore, the morphological properties of thin magnesium oxide (MgO) films grown on Ag(100) could be reproduced. The MgO films were used afterwards to probe the adsorption behavior of N_2O by infrared spectroscopy, and this investigation was compared to prior studies on MgO(100)/Mo(100). This comparison showed that the IR spectra of N_2O reflect the different defect densities of the MgO films on the two substrates. The first UHV EPR spectra measured at W-band are the most significant results of the thesis. The measurements on the organic radical DTBN proved that the spectrometer adaptation to the pressure conditions succeeded and that paramagnetic species present in submonolayer quantities can be detected. Additionally, the measurements on MgO(100)/Mo(100) showed that paramagnetic centers on oxidic surfaces and interfaces can be investigated.

Zusammenfassung

Die vorliegende Doktorarbeit beschreibt erstmalig den Aufbau und die ersten Tests einer Apparatur, die unter Ultrahochvakuumbedingungen (UHV) Elektronenspinresonanz(ESR)-Spektroskopie im W-Band (94 GHz) erlaubt und mit einer Reihe von anderen Techniken wie Rastertunnelmikroskopie (STM), Infrarotspektroskopie (IR), Beugung niederenergetischer Elektronen (LEED), thermischer Desorptionsspektroskopie (TDS) und Augerelektronenspektroskopie (AES) kombiniert.

Eines der wesentlichen Probleme, die in dieser Arbeit bearbeitet wurden, bestand darin einen ESR-Resonator zu konzipieren, der zum einen den Anforderungen des Ultrahochvakuums gerecht wird und zum anderen eine möglichst optimale Sensitivität des Experiments realisiert. Anhand theoretischer Erwägungen ist ein Fabry-Perot-Resonator ausgewählt worden. Im speziellen wurde ein Resonator gewählt, der durch einen konkaven sowie einen planaren Spiegel gebildet wird, wobei letzterer zugleich als Probe dient. Eine Adaption dieses Resonators an das UHV gelingt durch die Positionierung eines etwa 150 μm dicken Quarzfensters zwischen den beiden Spiegeln. Dies erfordert allerdings, dass sich auch der zweite Spiegel zumindest im Feinvakuum befinden muss, um die Kräfte auf das Fenster zu begrenzen. Die hieraus entstehenden Probleme sind in der Arbeit detailliert untersucht worden. So erschwert beispielsweise die Randbedingung, dass sich beide Spiegel im Vakuum befinden, die Anpassung der Mirkrowelleneinkopplung in den Resonator erheblich. Drei verschieden Mechanismen der Einkopplung wurden getestet und eine kombinierte Methode aus Antennenkopplung im Vakuum und Drei-Schrauben-Tuner an Luft ausgewählt. Des Weiteren bereitete die mechanische Stabilität des Resonators beträchtliche Schwierigkeiten: Aufgrund der räumlichen Gegebenheiten im Magneten sind der Konkav- und der Planarspiegel mechanisch und thermisch nicht gut verbunden, was das System empfindlich für Vibrationen sowie thermische Drifts macht. Um Vibrationseinkopplungen zu verringern, wurde das Gesamtsystem auf einer optischen Bank aufgebaut, die von einem aktiven Schwinungsdämpfungssystem getragen wird. Temperaturgradienten im Labor führen zu einer Verstimmung des Resonators, die durch die automatische Frequenzkontrolle (AFC) des ESR-Spektrometers nicht ausgeglichen werden kann. Es wurde eine Regelschleife entwickelt, die das Fehlersignal der AFC nutzt, um die Position des Konkavspiegels mittels eines Peltier Elements auszugleichen. Darüber hinaus wurde der Einfluss des Fensters auf die Eigenschaften des Fabry-Perot-Resonators eingehend untersucht. Es zeigte sich,

dass die Positionierung des Fensters bedeutsam ist. Eine optimale Sensitivität findet man, wenn das Fenster möglichst dicht am planaren Spiegel positioniert ist. Außerdem zeigte sich, dass Spiegel mit einem größeren Krümmungsradius ein besseres Signal-zu-Rausch Verhältnis aufweisen – ein Verhalten, welches von dem für Resonatoren ohne Fenster abweicht.

Die Funktionsfähigkeit des in dieser Arbeit aufgebauten UHV Systems wurde anhand einiger ausgewählter Systeme getestet. Die Fähigkeit des STMs atomare Auflösung zu erreichen wurde an der rekonstruierten Si(111) Oberfläche demonstriert. Daneben konnte aber auch die morphologischen Eigenschaften dünner Magnesiumoxid (MgO) Filme, die auf Ag(100) gewachsen wurden, reproduziert werden. Diese MgO-Oberfläche wurde anschließend verwandt, um die Adsorption von N_2O mittels Infrarotspektroskopie zu untersuchen. Die Untersuchungen dienten dem Vergleich zu Messungen dieses Moleküls auf MgO(100)/Mo(100) und zeigten, dass die IR Spektren von N_2O die unterschiedliche Defektstruktur dieser beiden Oberflächen gut widerspiegeln. Höhepunkt sind die ersten jemals gemessenen W-Band ESR-Spektren im Ultrahochvakuum. Die Messungen an dem organischen Radikal DTBN beweisen, dass die Adaption des Spektrometers an die Druckbedingungen gelungen ist und dass das Spektrometer in der Lage ist, paramagnetische Zentren im Submonolagen-Bereich zu detektieren. Darüber hinaus zeigen die Messungen am System MgO(100)/Mo(100), dass es möglich ist, paramagnetische Spezies auf oxidischen Oberflächen und Grenzflächen zu untersuchen.

Publications

1. E. Kieseritzky, W.H. Ziegler, J. Rocker, A. Seiler, O. Bondarchuk, T. Risse, and H.-J. Freund, *Adaptation of a W-band EPR spectrometer to UHV conditions*, Review of Scientific Instruments, in preparation.

2. J.C. Lian, E. Kieseritzky, A. Gonchar, M. Sterrer, J. Rocker, H.-J. Gao, and T. Risse, *N_2O adsorption on the surface of MgO(001) thin films: an infrared and TPD study*, Journal of Physical Chemistry C **114**, 3148 (2010).

3. M. Sterrer, E. Fischbach, M. Heyde, N. Nilius, H.P. Rust, T. Risse, and H.-J. Freund, *Electron paramagnetic resonance and scanning tunnelling microscopy investigations on the formation of F^+ and F^0 on the surface of thin MgO(001) films*, Journal of Physical Chemistry B **110**, 8665 (2006).

4. M. Sterrer, M. Yulikov, E. Fischbach, M Heyde, H.P. Rust, G. Pacchioni, T. Risse, and H.-J. Freund, *Interaction of gold clusters with color centers on MgO(001) films*, Angewandte Chemie - International Edition **45**, 2630 (2006).

5. C. Di Valentin, K. M. Neymann, T. Risse, M. Sterrer, E. Fischbach, H.-J. Freund, V.A. Naszulov, G. Pacchioni, and N. Rosch, *Density-functional model cluster studies of EPR g tensors of F_S^+ centers on the surface of thin MgO(001) films*, Journal of Chemical Physics **124**, 044708-1 (2006).

6. M. Sterrer, E. Fischbach, T. Risse, and H.-J. Freund, *Geometric characterization of a singly charged oxygen vacancy on a single crystalline MgO (001) film by electron paramagnetic resonance spectroscopy*, Physical Review Letters **94**, 186101 (2005).

7. H. Abdoul-Carime, S. Gohlke, E. Fischbach, J. Scheike, and E. Illenberger, *Thymine excision from DNA by subexcitation electrons*, Chemical Physics Letters **387**, 267 (2004).